Proximity Projection Grating Structured Illumination Microscopy

Chin-Jung Chuang, MSc

Thesis submitted to the University of Nottingham for the

degree of Doctor of Philosophy

November 2011

Abstract

Structured illumination has been employed in fluorescence microscopy to extend its lateral resolution. It has been demonstrated that a factor of 2 improvement can be achieved. In this thesis, we introduce a novel optical arrangement, which we call Proximity Projection Grating Structure Illumination Microscopy (PGSIM). Although the method is based on the original structured illumination, the present technique can further improve the lateral resolution of the microscope. The technique makes use of a fine grating held in close proximity to the sample, with a layer of high refractive index optical thin film sandwiched between the two. The fringe pattern thus projected onto the sample contains grating vectors substantially higher than those that are possible with the original structured illumination setup. The presence of these very high grating orders is the basis for the significant improvement in the system resolution.

In this thesis, the principle behind the PGSIM will be explained. The optical system used to demonstrate the technique will be described, with particular attention paid towards the construction and alignment of the unit containing the fine grating. Experimental results will be presented to demonstrate the characteristics of the grating unit and the operation of the system. Further results obtained with the system

applied to fine particles will be given, showing the resolution improvement of greater than a factor of 2 compared to a conventional optical microscope. The thesis also contains detailed analysis of the performance of the system. From this analysis, it is concluded that greater resolution improvement can be achieved by using appropriate material for the optical thin film.

Publications

S. Liu, <u>C. J. Chuang</u>, C. W. See, G. Zoriniants, W. L. Barnes, and M. G. Somekh, "Double-grating-structured light microscopy using plasmonic nanoparticle arrays," Opt. Lett. **34**, 1255-1257 (2009).

C. W. See, <u>C. J. Chuang</u>, S. G. Liu, and M. G. Somekh, "Proximity projection grating structured light illumination microscopy," Applied Optics **49**, 6570-6576 (2010).

J. Zhang, Y. Huang, <u>C. J. Chuang</u>, M. Bivolarska, C. W. See, M. G. Somekh, and M. C. Pitter, "Polarization modulation thermal lens microscopy for imaging the orientation of non-spherical nanoparticles," Opt. Express **19**, 2643-2648 (2011).

Acknowledgements

Abbreviations

CCD	charged couple device
CFM	confocal fluorescence microscopy
DGSIM	double grating structured illumination microscope
HELM	harmonic excitation light microscope
LSPR	localised surface plasmon resonance
FWHM	full width at half maximum
NSIM	nonlinear structured illumination microscopy
OTF	optical transfer function
PSF	point spread functions
PMT	photo-multiplier tube
PALM	photo-activated localization microscopy
PGSIM	proximity projection grating structured illumination microscope
STED	stimulated emission depletion microscopy
STORM	stochastic optical reconstruction microscopy
SIM	structured illumination microscopy
SNOM	scanning near-field optical microscopy
SPEM	saturated patterned excitation microscopy
SWFM	standing-wave fluorescence microscopy
WFM	wide-field fluorescence microscope

Contents

Chapter 1 Introduction and Review

1.1   Introduction

This project is involved with the development of an optical microscopy technique which can overcome the conventional resolution limit.

Optical microscopy is a useful and irreplaceable tool for biological studies. Among many important aspects concerning an optical microscope is the lateral resolution. The resolution or resolving power can be defined as the smallest distance at which two points on a specimen can still be seen separately. However, the resolution is determined by diffraction, which is about 200nm in the conventional wide-field light microscope. This barrier is a fundamental physical limit and severely restricts the application of the microscope. Techniques with high resolving power are in demand as many samples encountered in biological and life sciences are characterised by features on the tens of nanometers scale. In the past few years, some high resolution microscopy techniques, including stimulated emission depletion microscopy (STED) [1], stochastic optical reconstruction microscopy (STORM) [2], and structured illumination microscopy (SIM) [3], have emerged and overcome the classical resolution limit.

Our research is based on SIM. Structured illumination has been employed in fluorescence microscopy to extend its system bandwidth. It has been demonstrated that a factor of two improvement in lateral resolution can be achieved. This thesis will focus on a novel optical arrangement that can further improve the resolution. We call this system the proximity projection grating structured illumination microscope (PGSIM) [4].

PGSIM uses a fine grating to produce a high spatial frequency illumination. Unlike conventional SIM, the upper limit of the spatial frequency component of the illumination is not restricted by the bandwidth or aperture of the optical system, so the factor of two resolution improvement limit associated with SIM does not apply for PGSIM. The key component in the PGSIM system is the sample holder, which contains the fine grating and a high refractive index thin film. It is the presence of this high index thin film that allows grating orders substantially higher than those achieved in SIM to illuminate the sample, thus forming the basis of much improved resolution. In common with SIM, spatially shifting of the illumination pattern is required. This is accomplished by varying the angle of the light beam incident at the grating unit. After acquiring the raw data at each phase step, the final high resolution image can be synthesized by a reconstruction algorithm. The resolution improvement will be demonstrated by computer simulations as well as experimentally.

1.2 Layout of thesis

This thesis focuses on the development of the PGSIM system. A study of PGSIM and the practical achievements will be presented. This thesis is organised as described below:

Chapter 1 contains introduction of the research project and literature review. It starts with the fundamental concepts of light microscope resolution based on diffraction theory. Then we will introduce a number of modern microscopy techniques that can achieve super resolution, with the main focus on fluorescence microscopy. A comparison of different techniques (STED, STORM, and SIM) and the recent developments will be described in this chapter.

In chapter 2, we will focus on the SIM and discuss the principle behind it. Discussion in the spatial frequency domain provides a clear picture of the workings of SIM and the reconstruction processing algorithms. A review of different hardware configurations will be given. This will include nonlinear SIM and grating assisted SIM. One technique, double grating SIM [5], which was developed in the early stage of this study, will be presented showing a resolution improvement in one dimension. Furthermore, we will discuss the possibilities of improving the SIM even more.

Chapter 3 presents the PGSIM from a theoretical viewpoint. We will explain the

combination of the fine grating and the high refractive index thin film as the sample holder, and how this arrangement will lead to a high spatial frequency illumination of the sample. It will be shown that, based on this grating unit, a system resolution equivalent to an imaging NA ≈ 4 can be achieved. The reconstruction algorithm appropriate for the proposed technique and the influence of the shape of the fine grating on the system performance will be discussed. Computer simulations will be used to support the analysis.

In chapter 4, the practical system implementation will be described. A bench top microscope set up is constructed in order to demonstrate the PGSIM. The set up is divided into three main sections: an illumination arm, an imaging arm and the grating unit. The requirements including the specifications of the optical and mechanical components for these three sections will be described. The construction of the grating unit is crucial to the system and will be discussed in detail. The integrity of the practical set up will be demonstrated with experimental results.

The next chapter contains the experimental results. Fluorescent beads are used as standard samples to be imaged by PGSIM system. Several raw pictures were recorded and then processed by the reconstruction algorithm. The final results demonstrated that lateral resolution improvement capability experimentally. Results obtained with two grating shapes: square and triangle will be presented. Point spread

functions (PSF) obtained experiments will be compared to theoretical ones, showing the resolution improvement and the image quality achieved. Investigation of the relation between the grating pattern and the PSF will be given.

In the last chapter, the summary to this thesis and general conclusions are presented. Future development and applications of PGSIM microscope will be proposed.

1.3 Background of microscopy

The optical microscope, often referred to as the 'light microscope', is an optical instrument which gathers the visible light from the sample and uses a system of lenses to form a magnified image. Optical microscopy is naturally related to the study of cell biology. Historically, the Dutch scientist Anton van Leeuwenhoek (1632-1723) was credited as the inventor of optical microscopy. However, it is believed that the English scientist Robert Hooke (1635-1703) was the first micrographic to publish his research based on the use of an optical microscope in 1665 [6]. Whereas Leeuwenhoek used a single lens in his simple microscope, Hooke developed a more complete microscope system containing two lenses.

By 1900 the theory and principles of the optical microscope were well

established [7]. Optical microscopes were used extensively and had become

indispensable as a research tool. Further development in optical and mechanical

design and high precision manufacturing, together with the development of digital

imaging techniques, have led to the modern optical microscopes being regarded as an

essential tool all around the world.
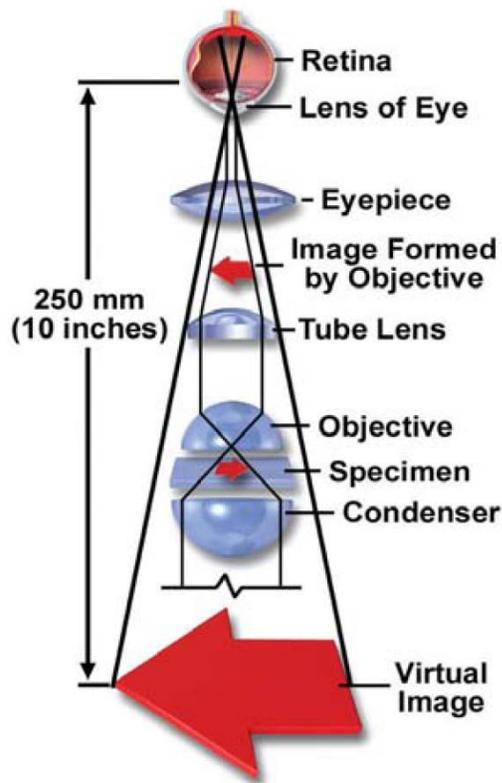
Figure 1.1 Light microscope basic configuration [8]

In the basic form, a conventional light compound microscope (figure 1.1)

consists of an objective lens and an eyepiece. An inverted magnified image of the

specimen is produced by the objective lens with the tube lens. The function of the

eyepiece is to project this image into our eye and create a further magnified virtual image. In addition, a camera can be used to acquire a digital image. Conventionally the virtual image is formed at a distance of 250mm from the eyes, as this is the least distance of distinct vision.

Sufficient light is required to illuminate the specimen. In general light from the light source, for example a lamp, would pass through a condenser, a field stop and an aperture stop before arriving at the specimen. The scattered light is gathered by the objective lens and, together with the tube lens, an image of the specimen is formed in front of the eyepiece. This results in a real image being formed at the retina of the eyes. The microscope thus provides a magnified image of the sample, and allows researchers to conduct detailed investigations in microscopic scale. For a typical microscope, the magnification ranges from x20 to x1000. It is important to point out that large magnification does not necessarily mean more detail can be seen. The amount of detail depends on the resolving power of a microscope, which is the smallest separation at which two separate objects can be distinguished (or resolved). Increasing the system magnification does not change its resolving power. Resolution is a key consideration of microscope and it will be discussed in next section (section 1.4).

For different applications, several types of microscopes have been developed.

For example, the dark field technique improves the visibility of certain features and makes small objects, such as bacteria, visible in this case; the organism is made to appear bright against a dark background. Another technique, phase contrast microscopy, turns the phase signal to visible intensity information to introduce contrast into the image of unstained or poorly stained specimens. In the family of optical microscopy, fluorescence microscopy provides observation of cells and tissues with custom markers. It helps to address specific questions regarding life sciences, and by using various fluorophores, different features can be identified.

Fluorescence refers to the effect that some molecules can absorb light of a certain wavelength and re-emit at a longer wavelength. The shift of the emission light to longer wavelengths is referred to as Stokes shift [9].
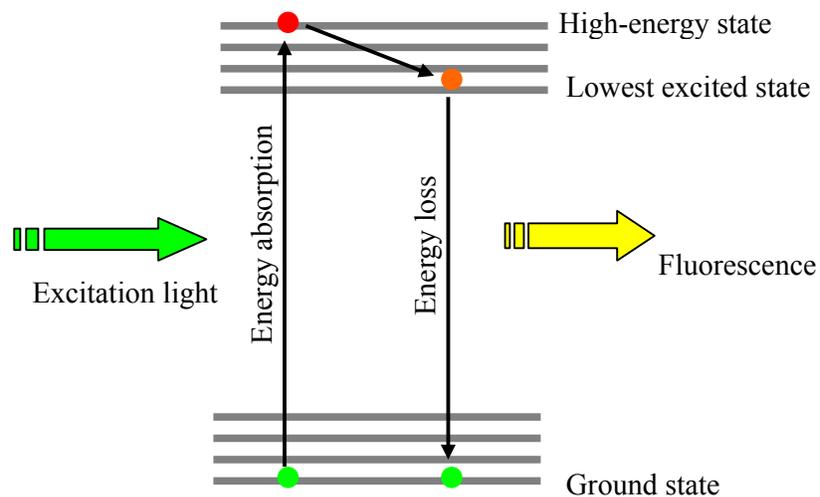
Figure 1.2 A simple view of states and transitions of a fluorophore.

The energy diagram in figure 1.2 shows the Stokes shift process. The photon

absorption excites the fluorescent molecule, originally in the ground state, to enter a high-energy state. When re-entering the ground state, the molecule emits a photon with energy equivalent to the difference between the lowest excited state and the ground state. Since the emitted photon loses some energy compared with the absorbed energy it is less energetic and has a longer wavelength than the absorbed photon. The emitted photon can be detected by a charged couple device (CCD) or photo-multiplier tube (PMT), thus converting the photon energy into electrical signals. By attaching fluorescent markers to features of interest, the sample can be studied through the distribution and the density of the fluorescent markers in the image.

Samples that are intrinsically fluorescent or which are coupled to extrinsic fluorescent molecules can be imaged by a fluorescence microscope. The fundamental function of a fluorescence microscope is to project excitation light onto the fluorophore in the specimen and to detect the much weaker emitted fluorescence light. The wavelength selection is fulfilled by the combination of excitation filter, dichroic filter and emission filter. A typical epi-fluorescence microscope configuration containing a filter set is shown in Figure 1.3.
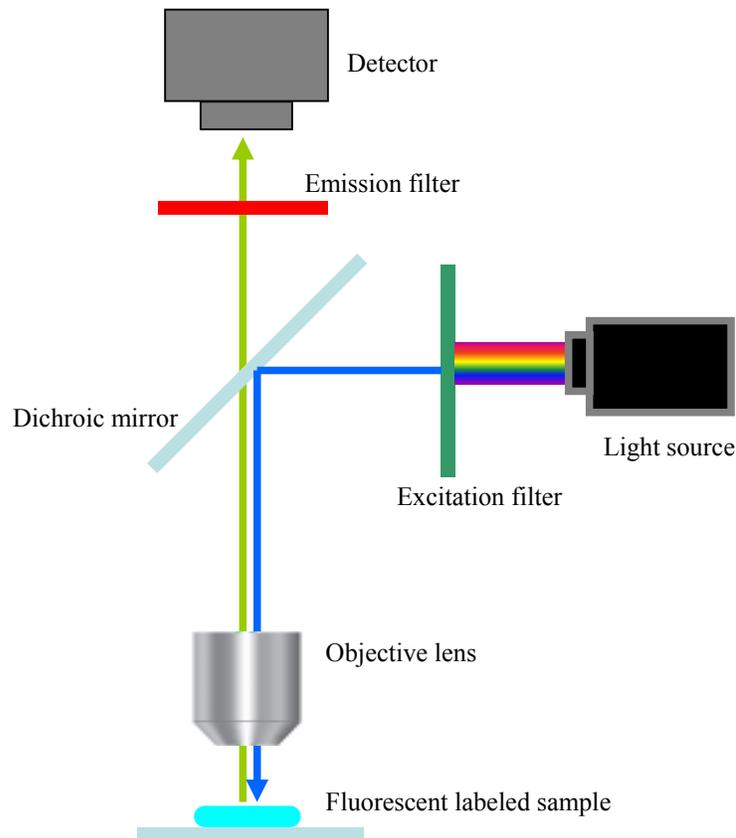
Figure 1.3 A typical epi-fluorescence microscope configuration [10].

The excitation filter is used to select the excitation wavelength of light from a light source. When the light source is a laser, it is usually unnecessary to employ an excitation filter. The dichroic filter, usually a long-pass filter, reflects the short wavelength excitation light to the objective. Furthermore, it allows the long wavelength emitted fluorescent light to pass to the detector, but at the same time blocking the passage of the shorter excitation wavelength. The emission filter that is usually a band-pass filter specifically selects the wavelength of the light emitted from the sample and removes the traces of residual excitation light. It is common practice

to use both a dichroic beamsplitter as well as an emission filter, as the intensity of the excitation beam is much stronger than that of the emitted light.

In recent years, fluorescence microscopy has evolved into a number of super-resolution techniques that can go beyond the diffraction limit and offer lateral resolution in the nanometre scale. These fluorescence imaging techniques find applications in advance biological research and have truly become fluorescent nanoscopy. A brief discussion (section 1.5) outlines some of the recent developments and several promising super-resolution techniques.

1.4   Resolution

The resolution of a microscope refers to the ability to observe a structure in detail, and is usually defined as the ability to distinguish two objects that are close to each other [11]. Because of diffraction, a small point object imaged by a light microscope appears broadened comparing to the original object [12]. Once the images of two close object points overlap and the resulting image contrast reduces to an indistinguishable level, the microscope is said to be not able to resolve them. The smallest separation where the objects can be distinguished is considered the resolution of the microscope [13].

1.4.1 Point-spread-function

The impulse response is used to describe the system response to an ideal infinitely sharp input delta function. With an optical microscope, the input delta function is a single point source, and the corresponding image is referred to as the point-spread-function (PSF) [12]. Typically, the PSF has a radial symmetry and can be described by the Airy disc [14]:

$$I = I_0 \left[\frac{J_1(u)}{u} \right]^2 \qquad \text{where} \quad u = \frac{2\pi}{\lambda} \rho \, NA \qquad\qquad (1.1)$$

where I is the intensity distribution, I_0 is the intensity at the centre of the pattern, J_1 is the first order Bessel function of the first kind, λ is the wavelength of the imaging light, ρ is the radial coordinates at the image plane, NA is the numerical aperture of the imaging system and is expressed as:

$$NA = n \times \sin(\theta) \qquad\qquad (1.2)$$

where n is the refractive index of the medium between the specimen and the objective lens, and θ is the light collecting half angle of the objective lens. According

to Eq. 1.1, the diameter of the Airy disc, taken as the diameter of the mainlobe (microscope PSF) is given by:

$$d = \frac{1.22 \times \lambda}{NA} \qquad (1.3)$$

As shown in Eq.(1.3), this diffraction phenomenon as described by Abbe [12] depends on the wavelength of the light and the NA of the objective lens. When a microscope can achieve this theoretical, ideal PSF, it is described as diffraction limited. In terms of PSF, the narrower PSF means the better resolution. A common measure of the PSF is the value d in eq (1.3). Another parameter of interest is the full width at half maximum (FWHM) which is about 43% of d (figure 1.4 (b)).
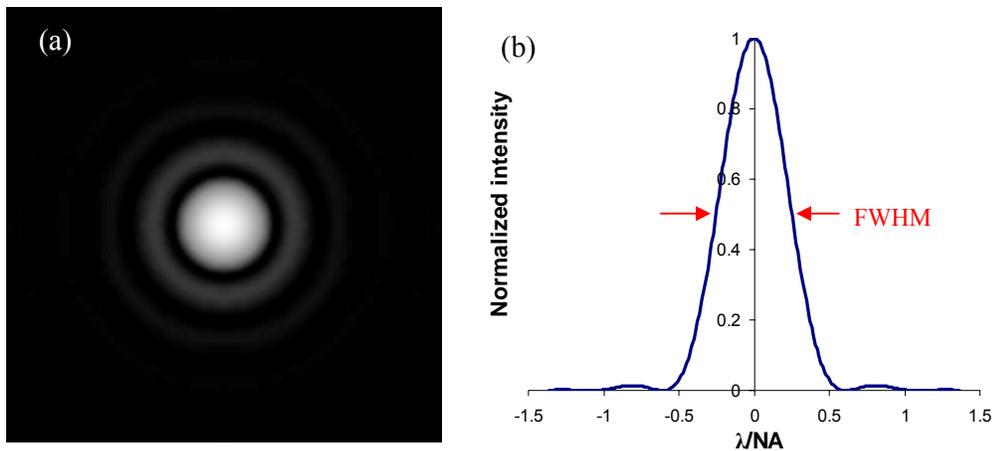
Figure 1.4 a) Airy disc, the system point spread function (PSF); b) Centre cross-section of the PSF, showing its full width at half maximum (FWHM).

It is important to emphasize that resolution is different from magnification. An image of the sample can be magnified by a large amount, but the magnification process does not increase the information content of the image. From optical image to digital image, the magnification should be controlled so that details are sampled satisfying the sampling theory [12]. However, any sampling process does not provide new information and will not improve the resolution [15].

1.4.2 Two-point resolution by Rayleigh and Sparrow criteria

Since the optical system can only collect light diffracted from the sample over a limited angular range, this imposes an upper limit to the lateral resolution of the system. Resolution is often discussed in the context of a two-point object. The intensity profile of the PSF has zero value at regular distances (figure 1.4). The circle inside the first zero is the Airy disc and its radius is called the Rayleigh distance. Rayleigh distance is the basis of the Rayleigh resolution criterion [16], where it was proposed that when the central maximum of one Airy disc lies on the first zero of the other, the two point objects are considered just resolved (figure 1.5).
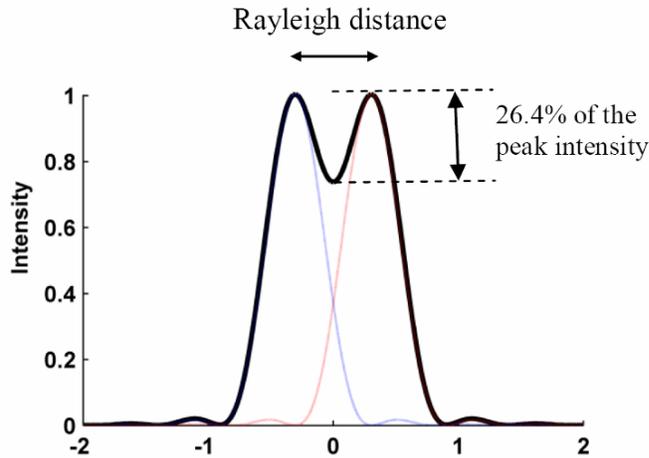
Figure 1.5 Rayleigh resolution criterion of two identical points, where the maximum of one of the PSF coincides with the first minimum of the second PSF, which gives a contrast of about 26.4%; the blue and red dotted lines show the two contributing PSFs.

The criterion is based on two point-like objects of equal strength, and it gives a contrast of about 26.4% (contrast defined as the difference between the highest intensity and the lowest intensity found between the two PSF divided by the highest intensity). According to the Rayleigh criterion, the lateral resolution limit of a conventional microscope is given by:

$$r = \frac{0.61 \times \lambda}{NA} \qquad (1.4)$$

The resolution is determined by the objective lens NA and the light wavelength. The higher the NA of the objective lens, the finer the resolution, and a short

wavelength is beneficial for higher resolution as well. As an example, with a

wavelength of 500nm and an imaging NA of 1, the resolution is r = 305nm.

Also based on a two-point object of equal strength, the Sparrow criterion [17]

defines the resolution as the distance between two point-like objects when the

intensity at the mid-point of the image has the same value as the peak value at either

side. Under this condition, the contrast becomes zero and the distance between the

two objects is:

$$r = \frac{0.47 \times \lambda}{NA} \qquad\qquad (1.5)$$
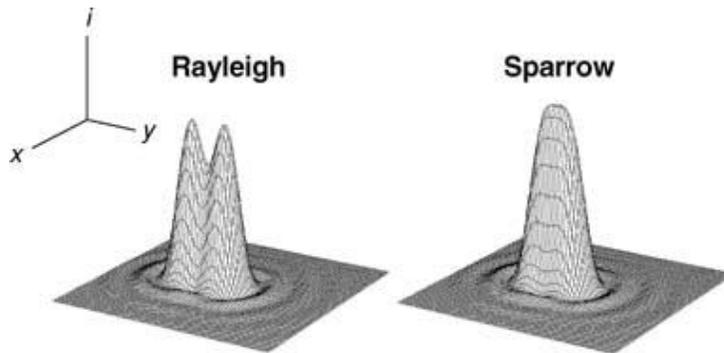
Figure 1.6 Comparison of Rayleigh criteria and Sparrow criteria [18]

Although these two resolution criteria are commonly used, the Sparrow criterion

leads to an apparent better resolution which is 18% smaller than the one defined by

Rayleigh criterion. They are rather subjective and by no means the absolute limit.

Therefore, these criteria provide a standard approach when comparing the resolution performance of imaging systems [19]. An alternative view in terms of spatial frequency and the bandwidth of the optical system can provide an objective measure of resolution. It relates resolution to the spatial frequency components accepted by the imaging system. It is the Abbe limit and will be discussed next.

1.4.3 Abbe limit bandwidth and spatial frequencies

The Abbe limit criterion provides an indication of an absolute resolution limit, and the incoherent case can be applied to fluorescence imaging. Based on the concept of spatial frequencies, the Abbe limit clearly defines the finest periodic structure that can be imaged by an optical microscope. It can be shown that light scattered from an object consists of individual components of different frequencies (equivalent to propagation directions) of various phases and magnitudes (the spatial frequency components) [12]. Fine object features will scatter light into high frequency components that propagate at large angles. The image formed by an optical microscope is the summation of the components that pass through the aperture of the objective lens and arrive at the image plane. However, the aperture of the objective lens is finite so that it is not capable of collecting very high spatial

frequency components scattered from a very fine structure. In this way, the aperture on the back focal plane of the objective lens acts as a low pass filter and determines the resolution of the system. Consider a grating object of period r, and assuming that the aperture of the objective is sufficiently large to collect the first order diffracted light (Figure 1.7), it can be readily shown that r and the NA of the system are related as:

$$r = \frac{\lambda}{2NA} \tag{1.6}$$
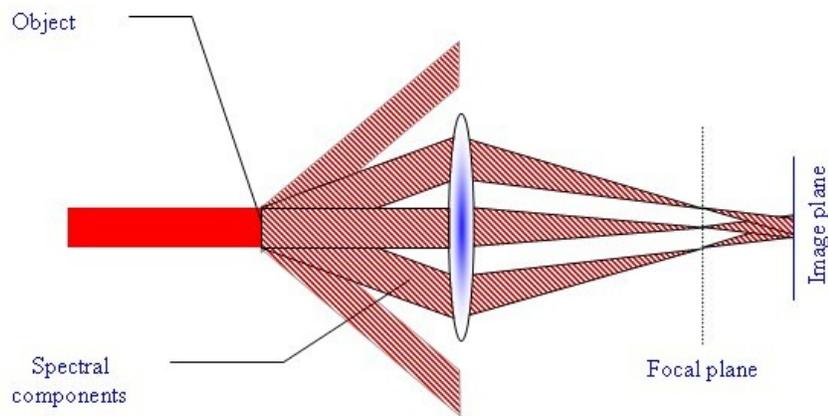
Figure 1.7 Imaging system as seen by Abbe[12]

In this situation, the structure period r is considered just resolved, and Eq. (1.6) is known as the Abbe resolution limit.

Following the Abbe image theory, we can derive the resolution of a microscope in the spatial frequency domain. If the object is coherently illuminated, then the image amplitude is given by[12]:

$$u(x,y) = \int\int\limits_{-\infty}^{\infty} u_o(\xi,\eta) h(x-\xi, y-\eta) d\xi d\eta \qquad (1.7)$$

where u_0 is the complex amplitude transmitted by the object, h denotes the PSF of the coherent system. ξ and η are the coordinate of the object plane. In spatial frequency domain, the expression becomes

$$\hat{u}(f_x,f_y) = \hat{u}_o(f_x,f_y)\hat{h}(f_x,f_y) \qquad (1.8)$$

where ˆ denotes the quantities after the Fourier transformation and f_x, f_y are the spatial frequencies.

The cut-off frequency f_c of $\hat{h}(f_x,f_y)$ can be connected to the physical limit of the optical system directly. Because of the limited aperture size (limited NA), only some part of diffracted light can be collected by the objective lens. So the amplitude transfer function works like a low pass filter and the shape is like a top-hat. For the coherent case, this amplitude transfer function $\hat{h}(f_x,f_y)$ refers to the spectra of

complex amplitudes from the object plane since a coherent system is linear in

complex amplitude.

$$f_c = \frac{NA}{\lambda} \qquad (1.9)$$

(a)   (b)
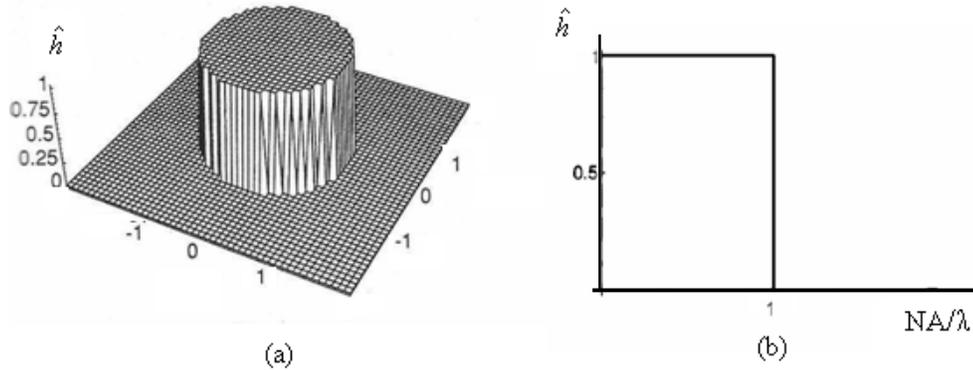
Figure 1.8 (a) amplitude transfer function in two dimensions and the shape is like a

top-hat; (b) half cross-section profile

For the incoherent case, such as fluorescence microscopy, the emitted light is

incoherent with a random phase relationship, and the image intensity should be

considered rather than amplitude. The image intensity is simply the sum of all

elementary intensity contributions:

$$I(x,y) = \int\int\limits_{-\infty}^{\infty} I_o(\xi,\eta) |h(x-\xi, y-\eta)|^2 \, d\xi d\eta \qquad (1.10)$$

Eq. 1.10 is a convolution integral in intensity. Let $H(\xi,\eta)=|h(\xi,\eta)|^2$, the expression becomes:

$$\hat{I}(f_x,f_y)=\hat{I}_0(f_x,f_y)\hat{H}(f_x,f_y) \tag{1.11}$$

$\hat{H}(f_x,f_y)$ is known as the optical transfer function (OTF) of the system. Using the autocorrelation theorem of Fourier transform, it can be shown that the OTF is given by the autocorrelation of the amplitude transfer function. For a circular aperture, the shape of the optical transfer function is a Chinese-hat as shown in figure 1.9.
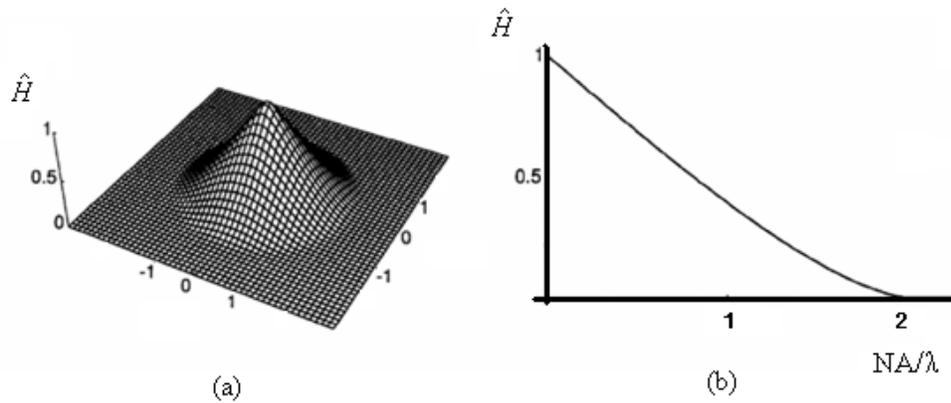
Figure 1.9 (a) optical transfer function in two dimensions and the shape is like a Chinese-hat (b) half cross-section profile

As discussed previously, the bandwidth limit in frequency domain provides a more quantitative limit on the resolution. This thesis contains mainly discussion on

fluorescence imaging systems, and attention will be focused in the incoherent case in the following discussion. The intensity transfer function will be used and the associated cut-off frequency will be employed as the criteria of resolution.

1.5   Imaging techniques and recent developments

The resolution of a conventional optical microscope is limited to about half the imaging wavelength, around 200nm, due to the diffraction of the light. Recently, scientists and researchers have tried to improve the resolution beyond this value, and different kinds of microscopes have been developed. These include the use of shorter wavelength, imaging with evanescent wave, or to use a confocal set up. These methods provide higher resolution and have found applications in many areas. They will be discussed briefly in section 1.5.1.

In addition, there are other more recently developed techniques which provide nanometer resolution and they will be presented in section 1.5.2.

1.5.1 Different kinds of microscopic techniques with high resolution

Electron microscopy

Benefiting from the much shorter wavelength of high energy electron, electron microscopy is used for studies at the molecular level. It has a much greater resolving power than conventional light microscopes, but the technique has several disadvantages such as requiring sample fixation [20] and suffering from radiation damage [21], making it unsuitable for imaging dynamic living cells. However, it can provide more details of a dry thin-cut processed sample, and the resolution is down to nanometres. Even considering the large size of equipment and high maintaining cost, it is still the more popular tool to explore the very fine structure.

Near-field scanning probe methods

Instead of an objective lens, near-field methods use a fine probe and the resolution is determined by the geometry of the probe and the interaction it has with the sample. Scanning near-field optical microscopy (SNOM) uses a probe (nano sized tip) close to the sample structure to collect the evanescent fields [22]. Although the technique can in principle achieve resolution in the order of 10nm [23], the practical resolution achieved with biological samples is typically in the range of 50-100nm [24-26] because of difficult involved in the fabrication of the probe and

interference with background light originated from other parts of the sample. Aside from technical and SNR issues these methods are constrained to imaging surfaces. Similar constraints are shared by other techniques which attempt to collect the evanescent fields such as the recent concept of a perfect lens, which uses a negative refractive index material [27].

Confocal microscope

Confocal microscopy is an optical imaging technique used to increase optical resolution and contrast. By using point illumination and a spatial pinhole in front of the detector to eliminate out-of-focus light arriving at the detector, it enables the reconstruction of three-dimensional structures from the obtained images [28]. As only one point in the sample is illuminated at a time, 2D or 3D imaging requires scanning in the specimen. The lateral resolution is improved over that of a conventional wide-field microscope by a factor of about 1.4 [29]. However, it only occurs when the pinhole size is smaller than the point spread function at the image plane, thus severely restricting the light throughput of the system. The much improved optical sectioning makes these types of microscopes particularly good at 3D imaging and surface profiling of samples [30]. This technique has gained

popularity in the scientific and industrial communities and typical applications are in life sciences, semiconductor inspection and material sciences.

1.5.2 Super resolution microscopic techniques

In the past few years techniques that can be called 'super-resolution' have emerged, and they can be defined as the techniques that are based on light microscopy but can bypass the limit of optical resolution. Notable examples include the structured illumination microscope (SIM) [3], stimulated emission depletion (STED) microscopy [1] and stochastic optical reconstruction microscopy (STORM) [2]/ photo-activated localization microscopy (PALM) [31]. Contrary to the near-field techniques, these recent developments are all based on the classical far-field operations. This property makes them highly attractive to biologists because of their compatibility with existing sample preparation procedure and the ability to look beyond the surface of a specimen.

STED and STORM/PALM, and a comparison between different super-resolution methods will be given in this section. SIM is the technique addressed in this thesis and will be discussed in details in chapter 2.

Stimulated emission depletion microscopy (STED)

The idea of STED is to use the fundamental physical process of stimulated emission to locally turn off the fluorescence emission of fluorophores. It was first introduced by Hell and Wichmann in 1994 theoretically [32]. In the actual experiment demonstrated in 1999 [33], a sample is spot-scanned with two lasers that were overlaid and synchronized: the first laser excites the fluorophores, and a second laser ("STED-beam") that has a longer wavelength and an intensity distribution of a doughnut shape generated with a phase mask depletes the fluorophores form their excited state. Provided that the irradiation intensity of the STED-beam is high enough, the particular intensity profile of the STED-beam leads to efficient quenching of fluorophores that reside in the excited state everywhere except close to the position of zero intensity inside the doughnut profile. The higher the irradiation intensity of the STED-beam, the smaller is the central area with zero intensity [34-35], such that the resolution enhancement in STED microscopy scales with the intensity of the depletion beam [36].

Figure 1.10 shows the concept of STED. Molecules in the region of zero STED intensity are also in an excited state and are left to decay by spontaneous emission. Although the size of the excitation PSF and the STED distribution still obey the diffraction limit, the effective PSF, which corresponds to the fluorescence light

emerging from the weak STED intensity region can be confined to much smaller

than the conventional diffraction limit.
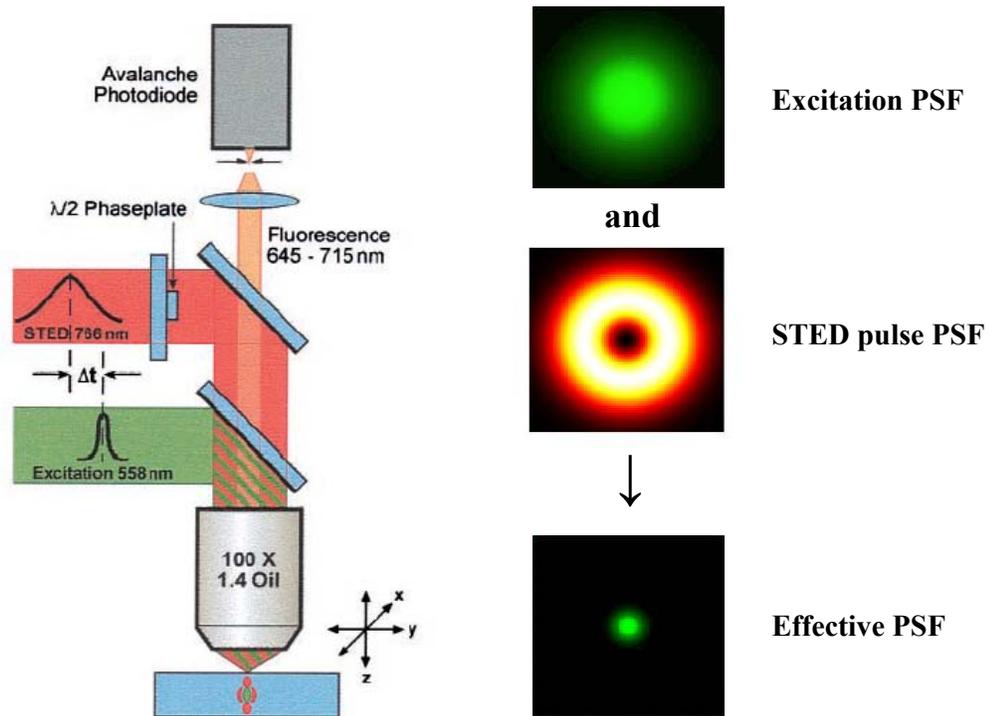
Figure 1.10 Schematic and concept of STED microscope [37]. Excitation (green) and STED (red) are accomplished with synchronized laser pulses focused by a lens into the sample. Fluorescence is captured by a detector and the focal point needs to be scanned all over the sample for a wide-field image. The left pictures show the shape of different laser: the excitation spot is overlapped with the doughnut-shaped STED spot featuring a central naught. Saturated depletion by the STED beam reduces the region of excited molecules to the small zero point, leaving a fluorescent spot of sub diffraction dimension

Stochastic single molecule localization

Single-molecule localization based super-resolution microscopy is enabled by detecting fluorescence emitted from isolated fluorophores and the subsequent determination of their molecular positions. In localization based techniques, only a small proportion of individual molecules are randomly activated each time. Adjacent molecules remain off during this period. The activated molecules are then excited until enough photons are collected to allow an accurate localization of their coordinates. The registered molecules are then switched off to complete one operation cycle. This process is repeated thousands of times. The positions of the individual molecules are determined by determining the centre of the blurred spots on each image, and the latter is used to construct a super resolution image (figure 1.11).

This localization approach can determine the locations of the particles with high precision, with the ultimate limit governed by the signal to noise ratio of the system. Although high precision single particle/molecule localization has been practiced for a long time [38], it is not a microscopy technique by itself because the dense labeling of a structure hinders imaging individual molecules whose diffraction-limited images overlap with each other. This localization-based super-resolution microscopy technique was independently developed and named as stochastic optical

reconstruction microscopy (STORM) [2], and photoactivated localization microscopy (PALM) [39-40] in 2006. This type of technique has the added advantage of using essentially the conventional microscope setup. Typical resolution achieved is currently around 20-30nm [41].
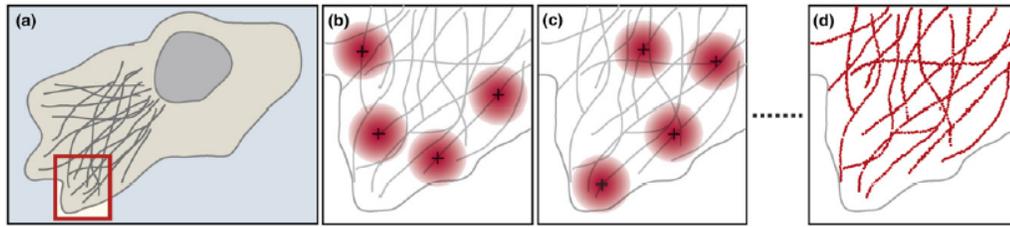

Figure 1.11 concept of Super-resolution imaging by high precision localization of photo-switchable fluorophores [42]. (a) Schematic of a cell in which the structure of interest (grey filaments in this case) are labeled with photo-switchable fluorophores (not shown). All fluorophores are initially in the nonfluorescent state. The red box indicates the area shown in panels b–d. (b) An activation cycle: a sparse set of fluorophores is activated to the fluorescent state, such that their images (large red circles) do not overlap. The image of each fluorophore appears as a diffraction-broadened spot, and the position of each activated fluorophore is determined by fitting to find the center of the spot (black crosses). (c) A subsequent activation cycle: a different set of fluorophores is activated and their positions are determined as before. (d) After a sufficient number of fluorophores have been localized over the course of multiple activation cycles, a high-resolution image is constructed by plotting the measured positions of the fluorophores (red dots).
The resolution of this image is not limited by diffraction, but by the precision of each fluorophore localization and by the number of fluorophore positions obtained.

To briefly summarize section 1.5.2, super resolution techniques have developed rapidly in recent years, and the emergence of different photo-activatable and photo-switchable fluorophores have increased the application areas for these techniques. They keep the advantages associated with far-field microscopy and

provide biologist with a powerful tool to observe the interior of cell.

Another promising super-resolution microscopic technique is structured illumination microscopy (SIM) [3]. When a sample is illuminated using a structured pattern, the illumination orders down convert the high spatial frequency components to within the system aperture. This effectively extends the bandwidth of the system and eventually leads to a higher resolution. This method can enhance the resolution of the system by up to a factor of two comparing with the diffraction limit conventional microscope. SIM is a wide-field technique and can potentially provide a fast real time high resolution image. As the system PGSIM discussed in this thesis is based on the original SIM system, the latter will be discussed in greater detail in Chapter 2. Table 1.1 shows the published resolution performances of different microscope systems for comparison. The advantages and disadvantages of each microscopy will be discussed in the final chapter.

Type	Best lateral resolution (nm)	References
Confocal fluorescence microscopy (CFM)	~150	[28]
Stimulated emission depletion microscopy (STED)	~20	[43-44]
Stochastic optical reconstruction microscopy (STORM)	~20	[2, 45]
Structured illumination microscopy (SIM)	~100 (linear) ~50 (nonlinear)	[3, 46-49]

Table 1.1 Comparison of different microscopes

1.6 Chapter summary

The aim and motivation behind the project have been presented in this Chapter. The main objective is to investigate, both theoretically and experimentally, the feasibility of using a novel optical component, namely the proximity grating unit, in conjunction with the SIM technique to provide an imaging resolution greater than a factor of two compared to the conventional microscope.

After outlining the layout of the thesis, a basic theory relating to optical system resolution has been presented, both in terms of the commonly used Rayleigh and Sparrow resolution criteria, and that based on diffraction theory linking the accepted spatial frequency components to the system bandwidth. It is shown that the resolution of a conventional system is limited to half of the optical wavelength and is around 200nm.

Some of the more recent development in high resolution microscopy techniques has been described. These include SNOM, confocal, STORM and STED. The resolution achieved by these systems ranges from 20 to 150nm. Their relative merits have also been discussed.

Chapter 2 Structured Illumination Microscopy

2.1 Introduction

As the technique described in this thesis is closely related to the structured illumination microscope (SIM), the concept and principle of SIM will be presented in this chapter. Computer simulation results and the more recent developments will also be given.

In the previous chapter, the resolution of optical imaging systems has been discussed, which provides a framework to understand the imaging performance of different microscope systems in terms of system transfer functions. The lateral resolution of a system depends on the numerical aperture of the imaging optics, but is also affected by the illumination system [50]. In fluorescence microscopy the simple diffraction argument needs to be modified because the fluorescence process discards the directional information of the illuminating light. To improve the resolution of a fluorescence imaging system, an intensity variation in the illumination is required instead of increasing the angular illumination range as with the coherent situation. This is precisely how SIM improves the lateral resolution. With SIM [3], the sample is illuminated by a series of sinusoidal excitation light patterns which encode the

normally inaccessible high spatial frequency information of the sample into several

recorded images. These images are then processed to yield a final reconstruction with

up to twice the normal resolution of the conventional widefield fluorescence

microscope (WFM).

High frequency information from the sample is encoded in the recorded

images in the form of the well known Moiré effect [51], where the resulting fringe

can be much coarser than either of the two original patterns. This encoded

information can be extracted using knowledge of the excitation light pattern and thus

giving normally inaccessible high frequency information about the object structure.

Figure 2.1 shows the Moiré fringe of two superposed patterns.
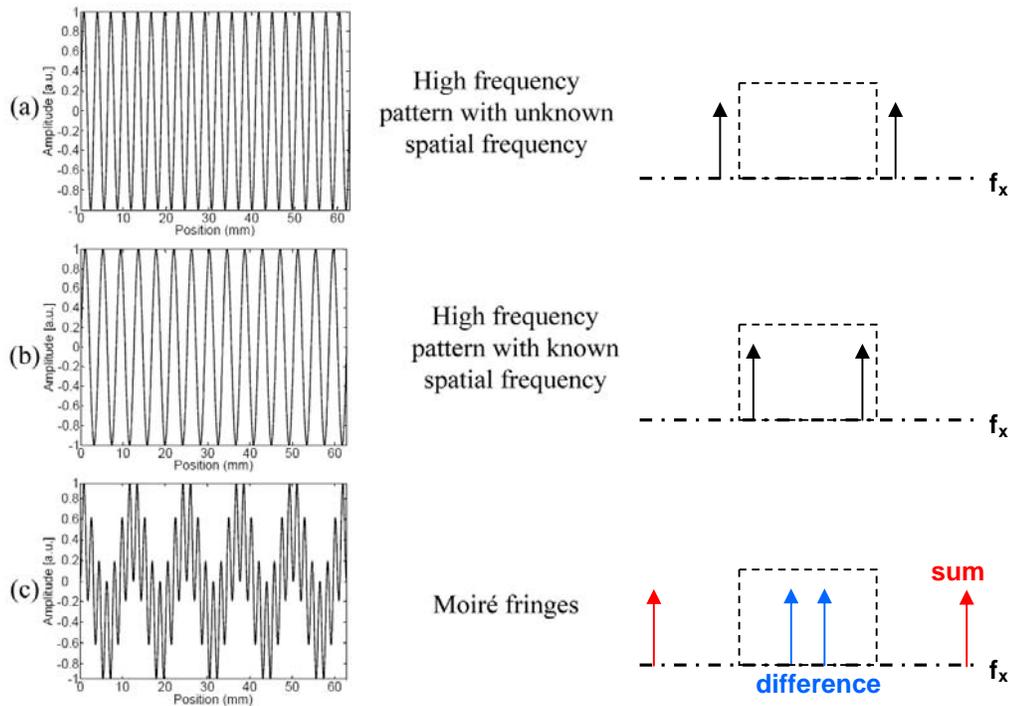
Figure 2.1 Moiré fringes: physical phenomenon behind SIM. The right hand column illustrates the phenomenon in the frequency domain, and the dash line is the system bandwidth.

In figure 2.1, (a) represents a signal whose frequency is outside of the

bandwidth of the system concerned, and (b) is a known signal whose frequency is

inside of the system bandwidth. The product of the two, which is those obtained in a

Moiré system, results in the up and down converted components, and the down

converted component can be arranged to be inside the bandwidth. The detected

signal thus contains high frequency information that is previously inaccessible to the

system.

The concept of improving the lateral resolution by means of structured

illumination came into reality in the last 10 years. In 1999, the idea of using a

diffraction grating to improve the microscope resolution was proposed by

Heintzmann and Cremer [52]. The first experimental result was presented by

Gustafsson two years later, showing a factor of 2 resolution improvement [3, 46]. In

2005, a nonlinear SIM with a 50nm lateral resolution was published. This represents

a fourfold improvement in resolution compared to conventional microscope [47].

Recently, a SIM system with doubled resolution in all three dimensions has been

demonstrated [48]. All these achievements have made the SIM becoming a key

technique in the exploration of higher resolution in optical microscopy. In this chapter, the principle of SIM will be presented.

Section 2.2 will illustrate step by step the process of SIM, with accompanying simulation results. In order to retrieve the high frequency information from the sample, the spatial phase of the structured illumination patterns needs to be altered. The procedure of changing the spatial phase of the illumination is called phase stepping [53-54]. Section 2.3 will show the application of the reconstruction algorithm to the raw phase stepped images. The synthesis of the SIM transfer function which would lead to a resolution improvement by a factor 2 will be discussed.

In section 2.4, more recent developments of SIM will be presented. Different approaches are applied to further improve the resolution. For example, in non-linear SIM, the fluorescence saturation characteristic is used to achieve improvement beyond a factor of two. Another way is to use nano-grating to produce high spatial frequency illumination [55]. At the same time, a novel method which we established in the early stage of this project will be discussed. It was named double grating SIM and was published in [5]. Double grating SIM combines a physical grating made using nano gold particle array and an optical grating which is the same as being used in conventional SIM. This combination produces intensity distribution with a high

spatial frequency, and improves the 1D lateral resolution improvement more than 5

times. Experimentally results will be shown.

In the end of this chapter, a summary will be given and the limitations of SIM

will be discussed. Since the illumination plays an important role in SIM and

determines the cut-off frequency of the sample, we consider a new approach to create

a unique illumination to improve the resolution by more than a factor of two in 2

dimensions. The work will be discussed in details in the next chapter.

2.2 Theory of SIM

In a fluorescence optical microscope, the acquired image $O(x,y)$ is the

convolution of the distribution of the sample $S(x,y)$ with the intensity point spread

function $h(x,y)$ of the microscope:

$$O(x,y) = S(x,y) * h(x,y) \tag{2.1}$$

where * denotes the convolution operation. In the frequency domain, the Fourier

transform of convolution is:

$$\hat{O}(k_x,k_y) = \hat{S}(k_x,k_y) \times \hat{h}(k_x,k_y) \tag{2.2}$$

where ^ indicates the Fourier transform of the quantity and k is the spatial frequency

component. The term $\hat{h}(k_x,k_y)$ is the Fourier transform of the PSF, and is therefore

the optical transform function (OTF) of the system (see section 1.4.4). As mentioned in the last chapter, the OTF of a fluorescence microscope is of a Chinese-hat shape, and the classical resolution limit is based on the fact that OTF has a finite cut-off frequency. In other words, high spatial frequency information outside the OTF cannot pass through the microscope, and thus the finer details cannot be resolved.

In a fluorescent microscope, the distribution of the sample is the fluorescent object $S(x,y)$ which is excited by the illumination intensity $I(x,y)$. Eq. 2.1 is therefore modified as

$$O(x,y) = [S(x,y) \times I(x,y)] * h(x,y) \tag{2.3}$$

The Fourier transform of the first multiplication is a convolution:

$$\hat{O}(k_x,k_y) = [\hat{S}(k_x,k_y) * \hat{I}(k_x,k_y)] \times \hat{h}(k_x,k_y) \tag{2.4}$$

The convolution mixes spatial frequency components from the sample with those from the illumination, and in particular shifts some of the high-frequency sample information into the OTF of the microscope. This is equivalent to using appropriate illumination structure to encode the high frequency sample signal in conventional images. Once obtained, these images can be decoded and the high frequency information restored.
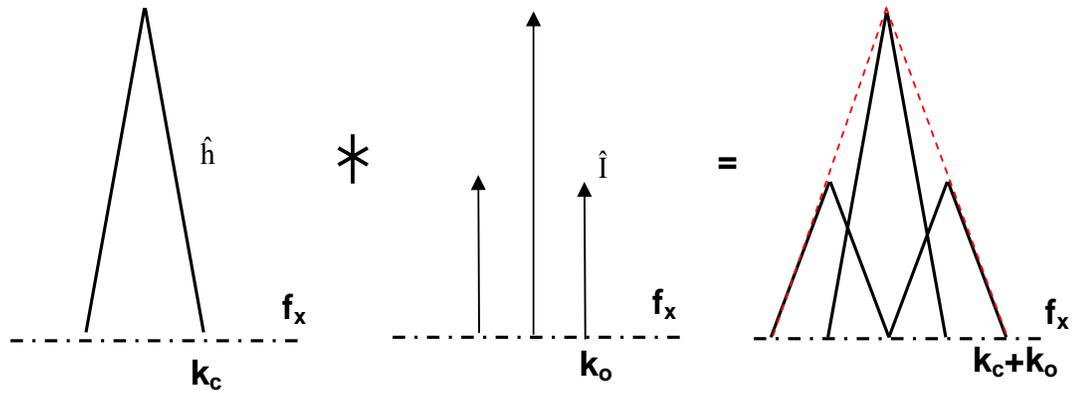
Figure 2.2 The process of SIM is to use illumination components as carrier to down convert different parts of spatial frequency signal of the sample. Then the spatial frequency signal will be decoded and restored to its proper position. The whole process is equivalent to shifting the original system transfer function and synthesis a new extended OTF. The left hand part of the picture is the optical system transform function with cut-off frequency k_c. By convolution with a sinusoidal illumination ($f_x = k_o$), a new synthetic OTF with wider bandwidth can be obtained. The final synthetic OFT cut-off frequency will be $k_c + k_0$. Red dash lines show the effective bandwidth of the synthetic OTF.

Figure 2.2 shows how structured illumination is used to extend the system bandwidth. The frequency components of the illumination behave like carriers in a communication system. Their function is to down convert the high spatial frequency signal which is originally higher than the cut-off frequency into the system bandwidth. As illustrate in figure 2.2, if the original system bandwidth cut-off frequency is k_c, the final system bandwidth as extended by the structured light with spatial frequency k_o will be $k_c + k_0$.

The highest spatial frequency of the illumination that can be cast onto the sample is limited by the optical system. For a reflection microscope, this frequency is

equal to the cut-off frequency of the microscope transfer function, hence $\max\{k_o\} = k_c$. Under this condition the final bandwidth of the system is $2k_c$, or twice the bandwidth of the original system. This represents the best improvement a linear SIM system can achieve. To go beyond this point, one needs to employ either non-linear operation, or the technique proposed in this thesis. For a transmission microscope, the final width with be the sum of the illumination and imaging bandwidth.

Based on the original microscope, a new synthetic OTF with wider bandwidth is created as shown in figure 2.2. The idea can be applied to 2D directly. Rotating the direction of the illumination pattern can generate carriers with spatial frequency components along different directions (Figure 2.3). In this way, a two-dimensional SIM image with improved lateral resolution can be reconstructed. The reconstruction process commonly used for this purpose will be shown in the next section.
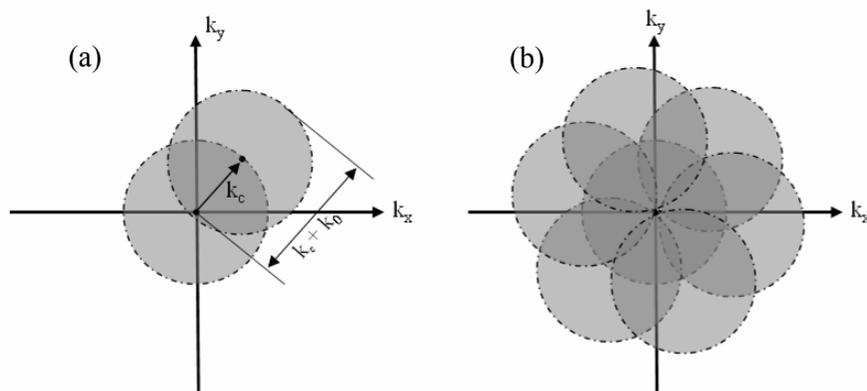

Figure 2.3 schematic explanation of two-dimensional resolution improvement in SIM in frequency domain. (a) The sinusoidal distribution illumination pattern has frequency components and the corresponding spatial frequency is k_0 which approaches the bandwidth cut-off frequency k_c. The observed images include the high

frequency information, and it can be decoded and restored to its proper position. (b) By repeating this process at different direction, a wider circle with twice the radius of the conventional bandwidth can be retrieved and restored.

2.3 Simulation and reconstruction process

The concept of SIM is best illuminated in the spatial frequency domain. The following results are obtained using simulations with a single point as a fluorescent sample to illustrate every stage of the SIM processing. All distances are measured in units of normalized wavelength (λ/NA) in spatial domain and normalized spatial frequency (NA/ λ) in the spatial frequency domain.

As previously discussed in section 1.1.4, the bandwidth of the optical system is limited by the numerical aperture of the objective lens. In two dimensions, the transfer function of a wide field system has the shape of a 'Chinese-hat' with a cut-off spatial frequency at ± 2NA/ λ, as shown in figure 2.4.
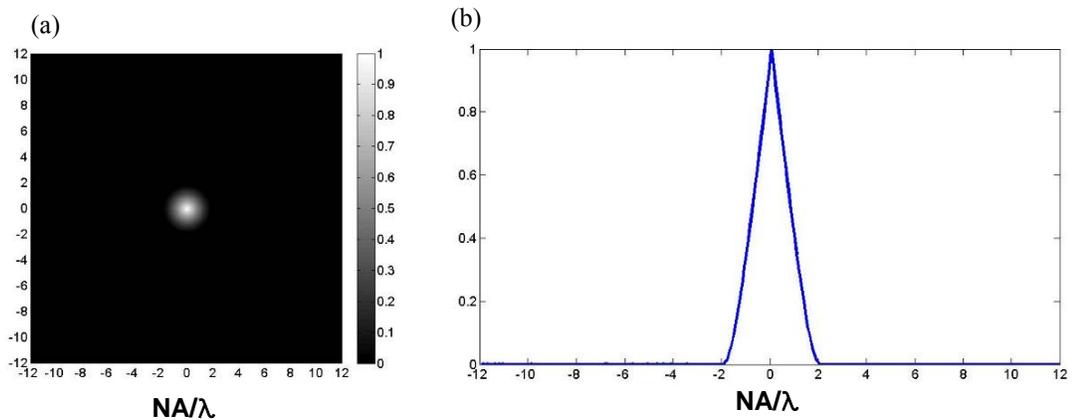

Figure 2.4 (a) 2 dimensional intensity transfer function of a conventional microscope; (b) Cross-section of the transfer function through the peak and showing the cut-off

spatial frequency at ±2NA/λ.
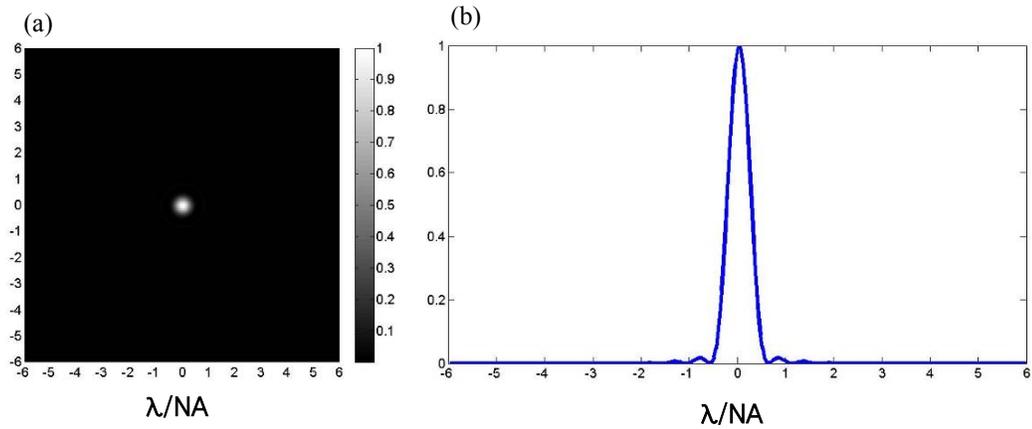
Figure 2.5 (a) PSF of a conventional microscope. (b)Centre cross-section of PSF and its diameter is 1.22

Figure 2.5 shows the corresponding PSF of the system. By convolving the PSF with the fluorophores used in a microscope, a fluorescent image of the sample will be obtained.
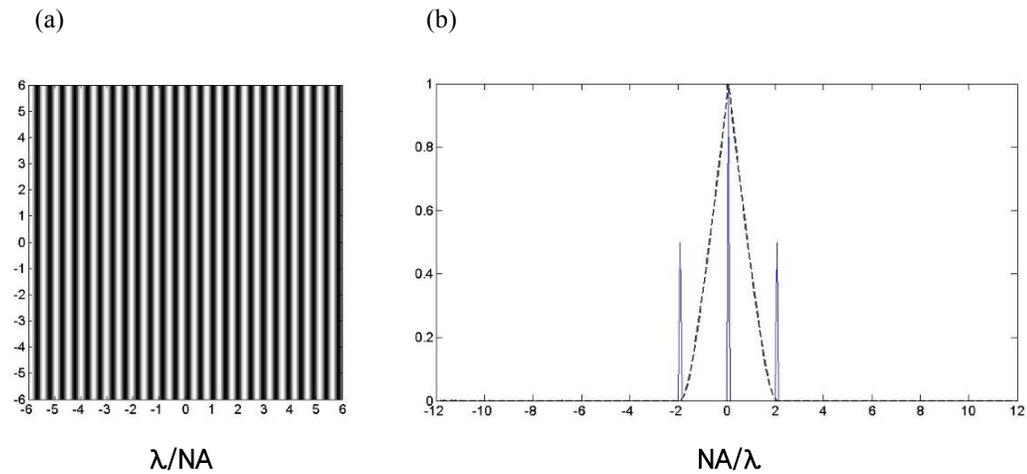

Figure 2.6 (a) Sinusoidal illumination pattern with the modulation depth = 1. (b) Centre cross-section of the Fourier components of the illumination (Blue line). It consists of both positive and negative spatial frequency and the DC. The dash line indicates the system transfer function.

With SIM, the sample is illuminated by a structured excitation light. Figure 2.6 (a) shows one such case with the illumination assumed sinusoidal. Figure 2.6 (b) shows the frequency spectrum of the illumination, containing three distinct components. Also shown is the transfer function of the optical system. Note that the frequency of the sinusoid cannot be higher than the frequency cut-off of the system bandwidth or the sample will be illuminated by a uniform distribution only. In the figure, the frequency of the sinusoidal pattern is assumed to hold the maximum possible value.

The image obtained using the structure illumination contains the sample information mixed with the illumination pattern. In the frequency domain, this is equivalent to convolving the illumination spectrum with the sample spectrum. There are, therefore, three duplicate sample frequency spectra, each centred at one of the illumination harmonics, as described by Eq. 2.4.

When captured, these three groups of frequency components overlap with each other and occupy the same region in the frequency domain. In order to form a high resolution image, the three groups of frequency components need to be extracted, separated and arranged into appropriate locations. A commonly used method for this operation is the one employed in the Phase stepping interferometry [56]. When applied here, a series of images, each with the illumination pattern shifted by a known amount, are captured. These images are then treated as a set of simultaneous

equations. When solved, the individual harmonics and the associated frequency

components are obtained, and the reconstruction process can continue.

(a) Illumination pattern   (b) Corresponding images

Step 1

Step 2

Step 3
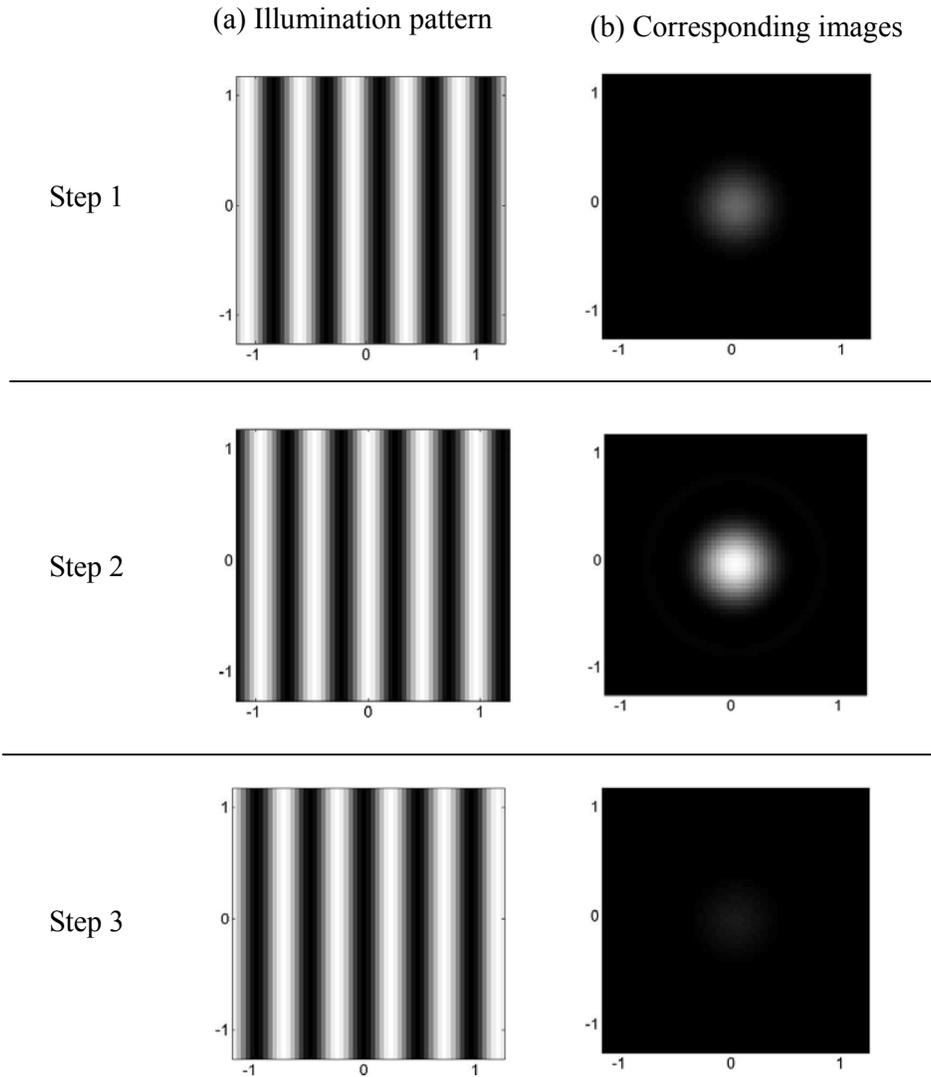
Figure 2.7 Three recorded images of a point like sample with different phase step illuminations. The phase shift between the illumination patterns in (a) is 120 degrees, and this causes the different images in (b). The unit is normalized wavelength λ/NA.

Figure 2.7 shows the multiple images taken using the phase stepping approach. The

lateral phase shift is $2\pi/3$ each step, so different parts of the sample are excited. Since

a single point is used as the sample in the simulation, the images appear to change in

intensity according to the phase step.

The next step is to perform the high resolution image reconstruction. Firstly, we

need to recover the spatial frequency components of the object associated with the

illumination frequency. Since the illumination pattern is a sinusoidal distribution with

frequency k_0, Eq. 2.4 can be extended as:

$$\hat{O}(f_x) = \hat{H}(k_x)[\hat{S}(k_x) + g_1\hat{S}(k_x - k_0)e^{i\theta} + g_1\hat{S}(k_x + k_0)e^{-i\theta}]$$
(2.5)

where g_1 is the modulation depth of the sinusoidal distribution, θ is the phase shift of

each step. The sample spectrum $\hat{S}(k_x)$ and the up and down shifted versions are all

shown in the equation. These three regions need to be separated by the phase

stepping process, resulting in three independent simultaneous equations:

$$\begin{bmatrix} \hat{O}_1(k_x,k_y) \\ \hat{O}_2(k_x,k_y) \\ \hat{O}_3(k_x,k_y) \end{bmatrix} = \begin{bmatrix} 1 & e^{i\theta_1} & e^{-i\theta_1} \\ 1 & e^{i\theta_2} & e^{-i\theta_2} \\ 1 & e^{i\theta_3} & e^{-i\theta_3} \end{bmatrix} \begin{bmatrix} \hat{S}_{DC} \\ \hat{S}_{+1} \\ \hat{S}_{-1} \end{bmatrix}$$
(2.6)

$$\hat{\mathbf{O}} \quad = \quad \mathbf{C} \quad \times \quad \hat{\mathbf{S}}$$

The phase-steps are usually selected to be equally spaced between 0-2π. These

three independent simultaneous equations can be solved by finding the inverse to the

matrix C in Eq 2.6.

Solving Eq (2.6) yields the spatial frequency components Ŝ, all of them have the

same bandwidth as the original system transfer function. Figure 2.8 shows the

shifting of the various frequency components to their correct positions.
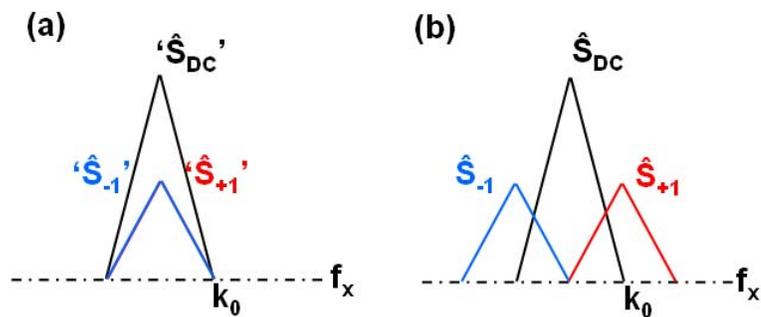
Figure 2.8 (a) The frequency components after solving Eq. 2.6; (b) The frequency
components after the shifting process.

The amount of shift is determined by the illumination pattern and in particular,

its spatial frequency. The bandwidth extension of the system is given by $k_c + k_0$, as

illustrated in figure 2.2. As explained above, the maximum improvement that can be

achieved is a factor of two of the original bandwidth. By taking the inverse Fourier

transform of figure 2.8 (b), an image with extended bandwidth will be resulted. This

is shown in figure 2.9.
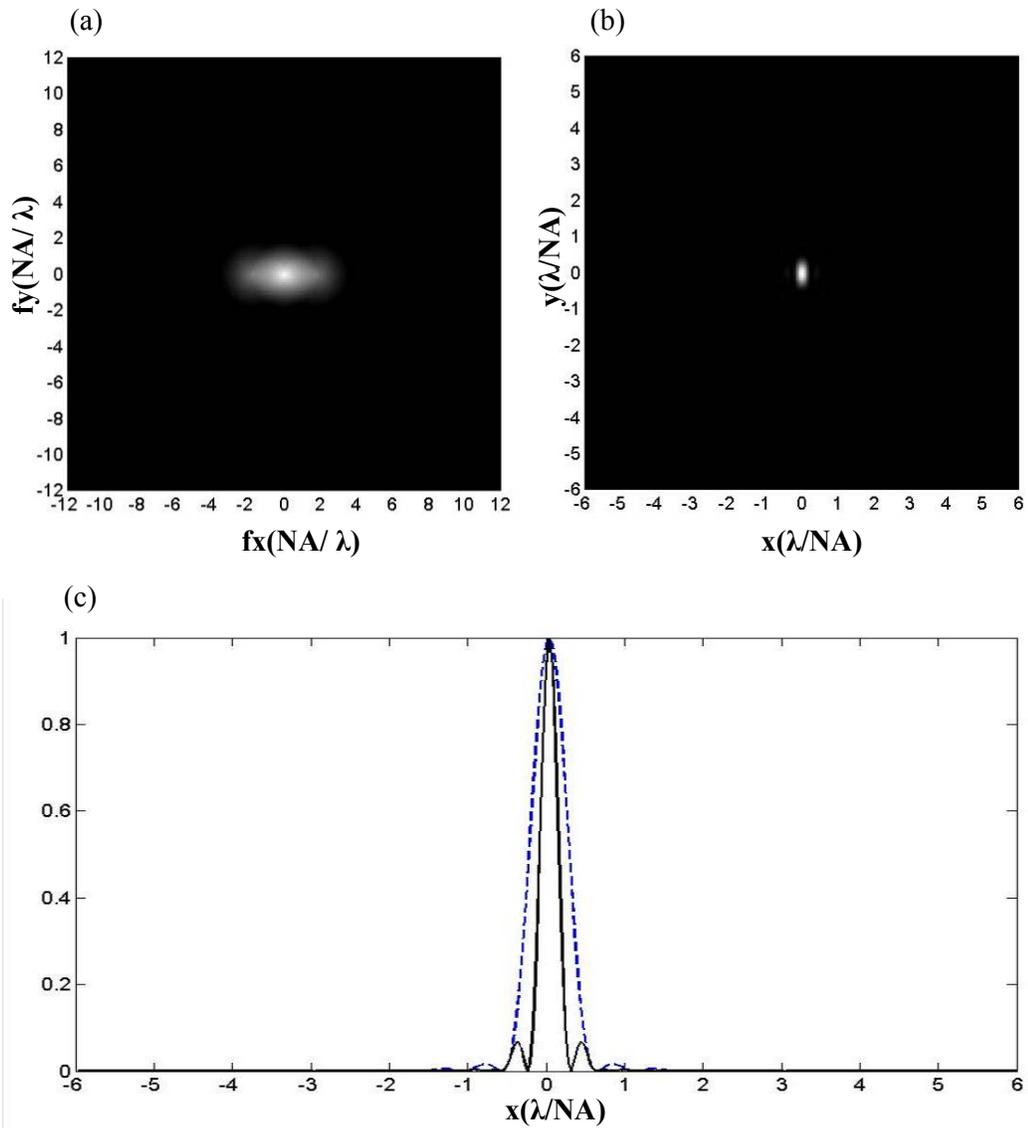
Figure 2.9 (a) sum of all three extracted components from figure 2.8; (b) reconstructed result in spatial domain. Notice that resolution is better in the horizontal direction; (c) is the centre cross-section profile of the image in (b) along horizontal direction, and the dash line is original conventional microscope PSF.

The above example has shown improvement in one direction only, thus figure

2.9 (b) appears long and narrow. For a more isotropic resolution enhancement, the

sinusoidal illumination pattern needs to be projected in more than one direction, with

the appropriate phase shifting process along each. The reconstruction algorithm is

same as the 1D case.

(a)   (b)
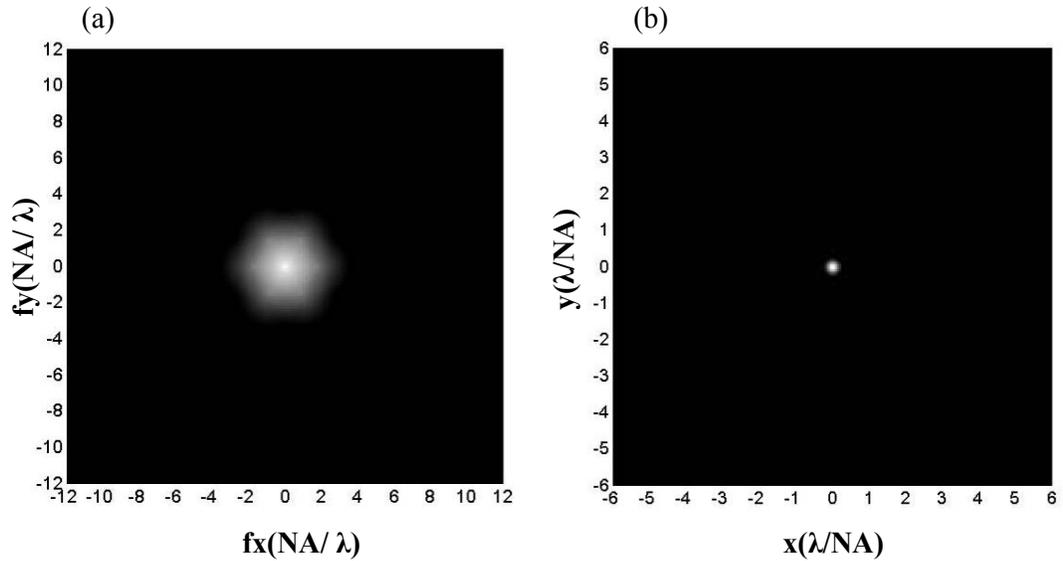
Figure 2.10 SIM with three illumination direction. (a) Reconstruction result in the spatial frequency domain and the bandwidth is extended by six frequency components. (see figure 2.3(b)). (b) The size of PSF reduces with more isotropic response compare to figure 2.9(b).

Figure 2.10 shows the SIM simulation result which includes three different

direction illumination patterns, spaced at 120 degrees apart. It is obvious that the

final reconstruction image is more isotropic and the resolution is improved along

both the vertical and horizontal direction.

2.4 Recent developments of SIM

The principle of SIM has been presented in the last section, with computer

simulations demonstrating the reconstruction process of the technique. In this section, some recent development of SIM techniques will be presented.

The first experimental demonstration of SIM was performed by Gustafsson in 2000 [3, 46]. In his system (figure 2.11), a 532nm light source was used, and the collimated linearly polarised light is directed to a phase grating, d. There were a large number of diffraction orders, but only the ±1 orders were used. The two beams were focused so as to form images near the edge of the aperture of an oil immersion objective lens, labelled h in the diagram. The resulting structured illumination pattern is a set of parallel lines of period 0.23μm that is approaching the resolution limit of the objective lens. The grating was located on a piezo translation stage, which in turn was mounted on a rotation stage. In this way, the phase stepping for reconstruction can be achieved by moving the stage laterally, and multiple directions improvement can be achieved by rotating the grating.
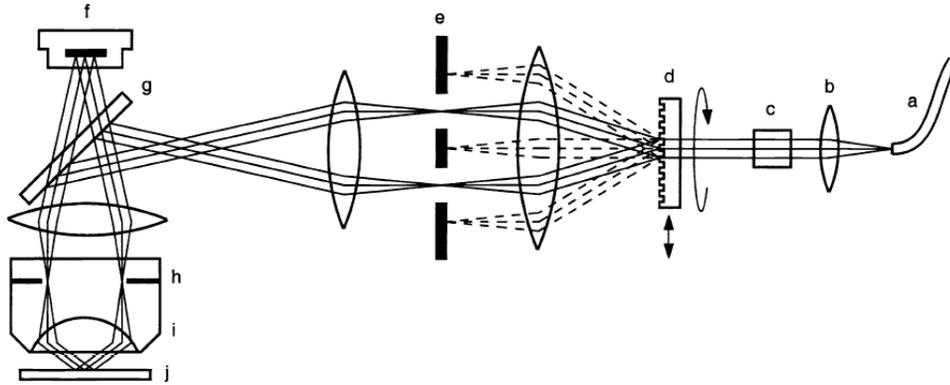
Figure 2.11 Schematic of the structured illumination system [46]. The phase grating d is located on a piezoelectric translation stage, which in turn is mounted on a rotation stage. Mask d allow the ±1 order enter the objective aperture h and form the structured illumination.

In this system, the lateral resolution exceeding the classical diffraction limit by a factor of two was achieved. It demonstrated a far field microscope with 100nm resolution. After that, Gustaffsson and the co-workers continuously developed the SIM technique, and the nonlinear SIM was introduced in 2005.

Nonlinear structured illumination microscopy (NSIM) [47] or saturated patterned excitation microscopy (SPEM) [57] works on the principle that once the illumination intensity is high enough to raise most fluorophores to the excited state, any additional increase in intensity will not yield a linear increase in the emission rate. This nonlinearity associated with the fluorescence excitation creates an illumination pattern with additional spatial frequency components at the sample. The

frequency values of these components are higher than that can be transmitted through the system aperture, and therefore can be used as carriers to give further lateral resolution enhancement.

With non-linear excitation, more illumination harmonics are involved. The processing algorithm is similar to the linear case, with more phase steps needed for the reconstruction. For each pair of additional harmonics two more phase stepped images are needed. In which case, Eq.(2.6) will become Eq.(2.7), indicating two addition harmonics and a total of five regions of sample spatial frequency components to be solved:

$$
\begin{bmatrix} \hat{O}_1(f_x,f_y) \\ \hat{O}_2(f_x,f_y) \\ \hat{O}_3(f_x,f_y) \\ \hat{O}_4(f_x,f_y) \\ \hat{O}_5(f_x,f_y) \end{bmatrix} = \begin{bmatrix} 1 & e^{i\theta_1} & e^{-i\theta_1} & e^{i2\theta_1} & e^{-i2\theta_1} \\ 1 & e^{i\theta_2} & e^{-i\theta_2} & e^{i2\theta_2} & e^{-i2\theta_2} \\ 1 & e^{i\theta_3} & e^{-i\theta_3} & e^{i2\theta_3} & e^{-i2\theta_3} \\ 1 & e^{i\theta_4} & e^{-i\theta_4} & e^{i2\theta_4} & e^{-i2\theta_4} \\ 1 & e^{i\theta_5} & e^{-i\theta_5} & e^{i2\theta_5} & e^{-i2\theta_5} \end{bmatrix} \begin{bmatrix} \hat{S}_{DC} \\ \hat{S}_{+1} \\ \hat{S}_{-1} \\ \hat{S}_{+2} \\ \hat{S}_{-2} \end{bmatrix}
\tag{2.7}
$$

It has been demonstrated experimentally that nonlinear SIM can achieve more than fivefold resolution improvement [47]. Although in theory it can provide even higher resolution improvement, its performance is always impaired by the weak intensity associated with the high harmonics illumination.

In 2008, a 3D SIM was established [48], and a grating is used to form an illumination pattern that varies both laterally and axially (figure 2.12). It demonstrated doubling in resolution approaching 100nm laterally and 300nm axially, and was used for the observation of nuclear periphery [49].
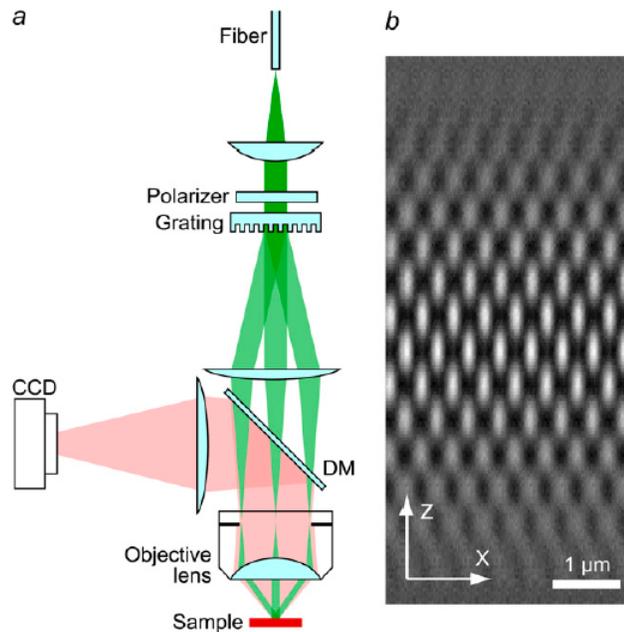

Figure 2.12 (a) Simplified diagram of the structured illumination apparatus. Scrambled laser light from a multimode fibre is collimated onto a linear phase grating. Diffraction orders –1, 0 and +1 are refocused into the back focal plane of an objective lens. The beams, recollimated by the objective lens, intersect at the focal plane in the sample, where they interfere and generate an intensity pattern with both lateral and axial structure (b). [48]

In addition, SIM was also combined with the I^5M technique [58-59], a well established high axial resolution microscopy technique, to form a microscope named I^5S [60], yielding images with 100nm resolution in all three dimensions (figure 2.13).

Furthermore, the SIM speed was also improved by using spatial light modulator to produce the illumination pattern. The system was demonstrated in the imaging of tubulin and kinesin in living cells [61].
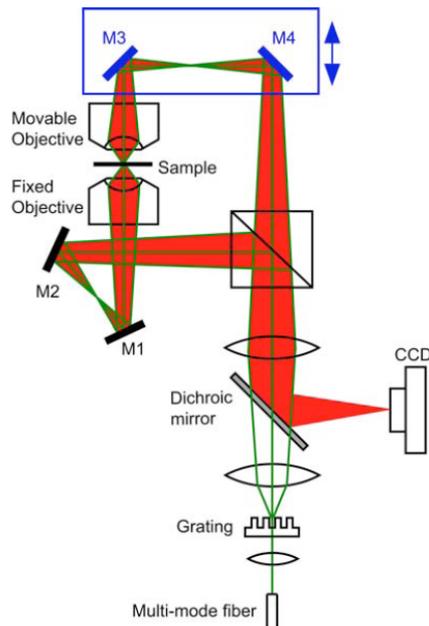

Figure 2.13 A schematic drawing of an I5S microscope [60]. The illumination light passes first through a transmission grating, which diffracts it into three beams (green lines), and then through a beam splitter, which splits each beam and directs three beams to each of the two opposing objective lenses. The same beam splitter combines the two beams of emission light (red) from the sample onto the camera. The movable objective lens can be positioned in X, Y and Z with respect to the stationary objective lens. Mirrors M3 and M4 can be translated together to adjust the path length difference. The grating can be rotated and laterally translated to control the orientation and phase of the illumination pattern.

The concept of using structured illumination has also been exploited by other research groups. Often these systems are described using different names, including harmonic excitation light microscope (HELM) [62-64], standing-wave fluorescence

microscopy (SWFM) [65-70], lateral modulated excitation microscopy and patterned

excitation microscopy [52, 57, 71-72].

Based on the concept of SIM, near-field fluorescence microscopy is created by

contacting the sample with the physical device to generate finer structured

illumination at the sample. Since the periodicity of the near-field device is not

limited by the diffraction through the illuminating optics, near-field SIM benefits

from a greater degree of resolution improvement. Sentenac proposed to create

illumination pattern by a sub-diffraction substrate (figure 2.14) [55]. The sample is

illuminated with different angles of incidence, and an appropriate reconstruction

scheme is used to restore the distribution of fluorescence density from a set of raw

images. The simulation result [73] shows the capability to improve the resolution

much more than conventional SIM.
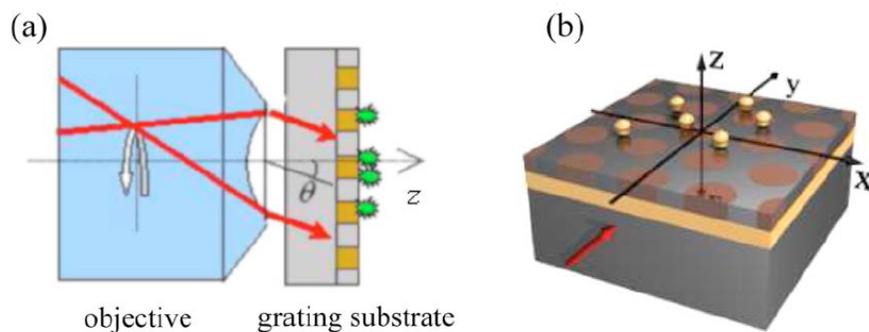
Figure 2.14 (a) Outline of the proposed experimental setup [55]. The fluorescent sample is deposited on a grating that is illuminated by one plane wave in total internal reflection configuration through an immersed objective. The fluorescence is collected through the same objective, and its image is formed on the image plane of the microscope. A total of 24 images are recorded by successively illuminating the sample under different incidence. (b) Zoom of the grating substrate.

2.5 Double grating SIM

The previous section shows the recent super resolution techniques based on SIM, where an intensity pattern with high spatial frequency components is used for illumination in order to extend the system bandwidth. In this section, a technique called double grating SIM will be discussed. It is developed in the early stage of this project, and adds a physical grating in contact with the sample to provide high spatial frequency illumination pattern. The experimental results demonstrate the potential of such an approach achieving resolution improvement beyond that of the conventional SIM.

As mentioned before, the nonlinear SIM distorts the excitation profile and creates higher-order spatial frequency components, thus providing better resolution. To avoid saturating the fluorophore, which can induce photo-bleaching, the idea of using a movable physical grating has been studied theoretically [55] (see figure 2.14). Since the physical grating is close to the sample and its periodicity is not limited by diffraction through the illuminating optics, it can thus enhance the resolution to a greater degree than the optical grating.

The physical grating used here relies on the localised surface plasmon resonance (LSPR) of gold nanoparticles [74-77]. When the k-vector of the incident

light beam matches the excitation conditions of LSPR, the incident electric field is

enhanced and confined to a small volume around the nanoparticles [78]. By changing

the orientations of the gold particles in a regular manner, the strengths of the

enhanced fields will change periodically. Combining physical and optical gratings

gives an even larger spatial frequency enhancement as these mix to produce sum and

difference frequencies. We call this system a double grating structured illumination

microscope (DGSIM). Figure 2.15 shows the schematic of the system arrangement.
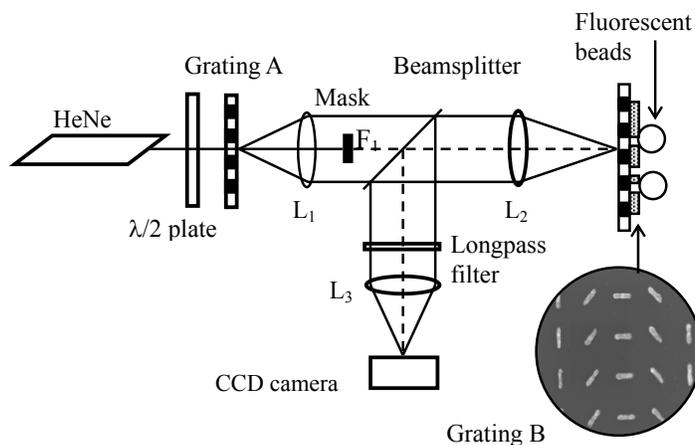
Figure 2.15 Schematic of the optical set up. Grating B is the physical grating and its electron micrograph, period = 1 μm [5].

The light source is a linearly polarised HeNe laser, with its polarisation

direction controlled using a half-wave plate. The rest of the system is the same as a

conventional SIM, except that the sample substrate is a specially designed physical

grating B. It consists of a coverglass with gold nanostructures arranged as shown in

figure 2.15. The gold nanoparticles were produced by electron beam lithography with

dimensions of 125 by 35 nm, and a thickness of 40 nm. In the array, the long axis of

each nanoparticle is rotated by 45 degrees in successive columns; a complete cycle

(180 degrees) is achieved every 4 particles. At the incident wavelength (633 nm) the

longitudinal resonance of the particles dominates the transverse resonance so that the

field enhancement close to the particle is far greater when the incident polarization is

oriented along the long axis.

To demonstrate the spatial phase shifting the grating was covered with a thin

uniform polymer layer (30 nm thick PMMA, 950kD) containing 2 wt% of the

fluorescent dye, Oxazine 1 perchlorate.   This dye has been shown to exhibit

enhanced emission when excitation is mediated by LSPR. The fluorescence image of

the physical grating comprised parallel stripes.   Figure 2.16 shows the spatial phase

of the stripes as polarization of the incident light was rotated, giving the effect of a

grating movement.

(a)   (b)
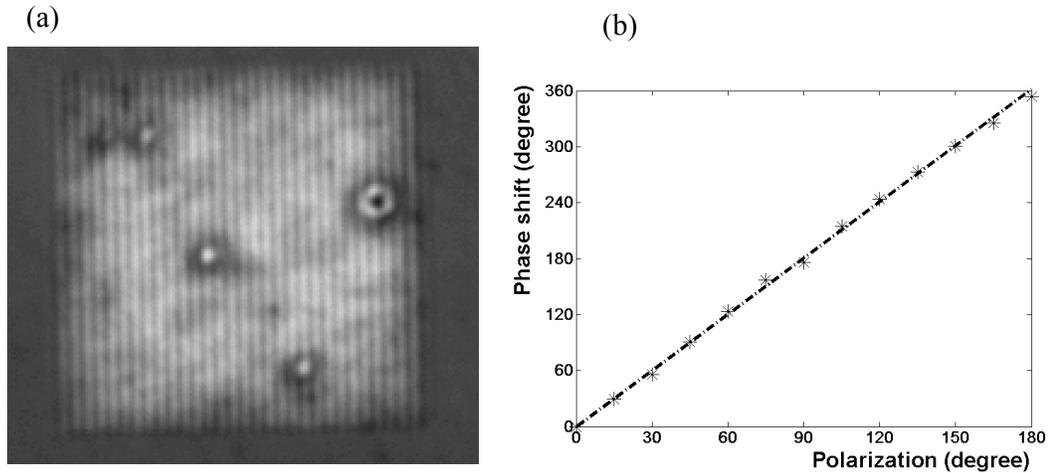
Figure 2.16 (a) the image of physical grating with linear polarization. (b) Optical phase shift of light beam after passing through the physical grating, as a function of the polarization angle of the incident beam.

By rotating the polarization, the illumination created by the physical grating will vary and the resulting intensity pattern will undergo a process similar to the phase stepping described above, thus providing the images for the reconstruction purpose. Combining the physical grating B with the optical grating A (conventional SIM), this double grating SIM can provide an illumination with spatial frequency afforded by the physical and the optical gratings, and in theory, is not restricted by the illumination optics. Experimental results presented below demonstrate the principle of the DGSIM and also show how the physical grating provides resolution enhancement. The objective used was an Olympus Plan N 20x objective with a numerical aperture of 0.4. The period of the optical grating when projected onto the sample was 2μm, a value expected to give modest but noticeable improvement in the system bandwidth. The period of the physical grating was 1μm. The substrate with

the physical grating was sprinkled with fluorescent beads of 1μm diameter

(FluoSphere carboxylate-modified microsphere, Crimson fluorescent (625/645)

Invitrogen).
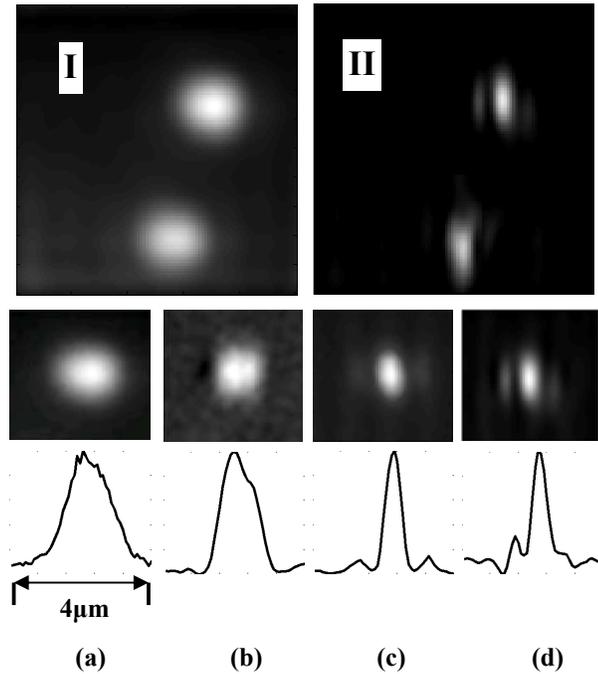
Figure 2.17 Images of two fluorescent beads obtained with (I) a conventional bright field microscope and (II) with the double grating system, both images are 9μm in width. The second row shows the intermediate processing (top right particle only), and third row shows the cross sectional profiles of the distributions in the second row. (a) Conventional microscope; (b) Optical grating only; (c) Physical grating only; and (d) Double grating.

Figure 2.17 shows the images of two fluorescent beads with different

combinations of the physical and optical gratings. (I) is obtained without any

enhancement, and (II) is with the double grating. The second row in the figure

concentrates on the particle near the top of the picture, to illustrate the intermediate

processing stages, showing images obtained with no enhancement, optical grating

enhancement only, physical grating enhancement only, and double grating enhancement. The reduction in the PSF applies in one direction only, and a factor of 2.3 improvement is achieved.

We have shown experimentally that an optically addressed physical grating based on particle LSPR can be used to provide PSF narrowing. The spatial phase of the structured light coming from the lithographic array can be changed simply by adjusting the polarization of the incident light, without needing to rotation the nanoparticle array. The period of this grating is not limited by diffraction. We have also shown how two gratings act together to further increase the bandwidth.

The use of polarization provides an excellent way of moving the grating but the effect is in one direction only, this problem may be addressed using concepts discussed in [79] where changing the incident angle or wavelength of excitation will give the additional degrees of freedom necessary to move the grating field in two dimensions.

Another issue is related to the minimum achievable grating period. While the method presented here is only one possibility, it should be noted that small particles show lower contrast between the long and short axis resonances. Nevertheless, this approach should still allow grating periods less than 100nm to be used, provided interactions between the metallic nanoparticles are considered. Such periodicities

when combined with an optical grating give potential bandwidth extension up to a factor of 5.

2.6 Discussion and summary

In this chapter, we have focused on the structured illumination microscope. The basic concept can be illustrated by Moiré fringes, and the harmonics of the structured pattern function as carriers to down-convert high spatial frequency signal into the system bandwidth. Simulations have been performed to show the operation of the technique step by step. From the literature review, the conventional SIM uses two beams through the objective aperture to produce interference pattern, and it can extend the system bandwidth twice. This corresponds to a lateral resolution improvement by a factor of two and the technique is applied to practical biology research.

Many techniques based on the SIM have been developed since, and complex illumination is created in order to improve the resolution even further. The nonlinear SIM takes advantage of saturated fluorescence light and show the capability of wide-field fluorescence imaging with theoretically unlimited resolution. However, the higher harmonics are typically weaker in strength and the SNR for the

extended higher frequency orders can deteriorate, thus limiting the practical performance of this technique. An alternative technique such as double grating SIM aims to encode higher spatial frequency information without fluorophore saturation. It uses gold nanoparticles to provide changeable field distribution and the high k vector which the grating can provide is no longer limited by the objective lens. However, there are two characteristics of double grating SIM: 1) only 1D resolution enhancement can be achieved; and 2) because of the decay of localised surface plasmon resonance, the physical grating only works at small region near the gold nanoparticles.

These drawbacks limit the practical application of double grating SIM. Concerning a novel SIM, a wide-field 2D microscope with high lateral resolution is necessary. The key challenge is how to create a 2D high spatial frequency illumination pattern not limited by the system optics, and that the pattern must be movable for reconstruction purpose.

In the next chapter, the idea of using a physical grating which can provide illumination with spatial frequency much higher than that can be afforded by the system optics will be introduced. This novel device, which we call the proximity projection grating, and the associated microscope, the proximity projection grating SIM, will be discussed in detail.

Chapter 3 Theory of the proximity projection grating SIM

As described in Chapter 1, we have developed a novel optical arrangement called the proximity projection grating structured illumination microscope (PGSIM). The arrangement is based on the original SIM, but has a superior resolution performance. In this chapter, the principle of the technique will be discussed. Computer simulations showing the operation of the system will also be presented. We will demonstrate that theoretically, an imaging NA approaching 4 may be achieved with the system, which would represent an improvement of 1.75 times compared to the conventional SIM. Furthermore, resolution improvement in 2 directions is readily achieved. We will present algorithm suitable for the 2D reconstruction.

3.1 Principles of proximity grating unit

As described in Chapter 2, the resolution of a conventional SIM is limited by both the imaging as well as the illumination NA. Our system will greatly reduce the limitation due to the illumination optics. The key component of the system is the

sample holder, which is designed to allow fringe pattern with *k*-vectors greater than 1

(in normalised units[1]) to illuminate the sample.
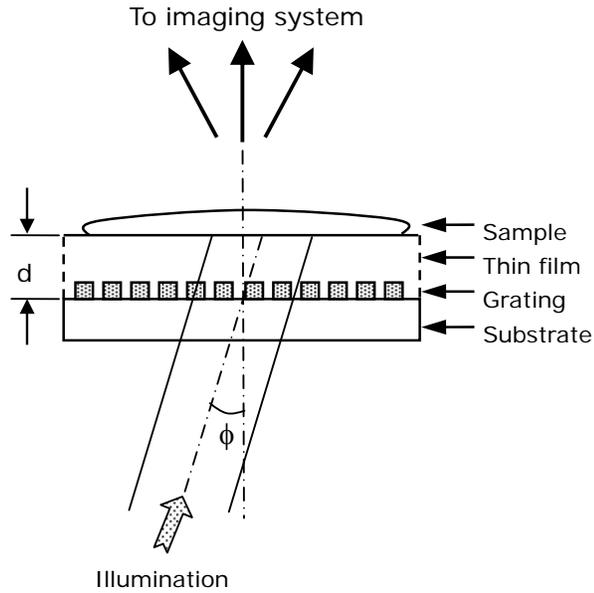
Figure 3.1 Sample unit showing the principle of the technique.

The sample holder is shown in figure 3.1. It consists of a fine grating, period

T_g, supported by a glass substrate. Between the grating and the sample is a layer of

optical thin film, the appropriate value of its thickness d will be discussed later in the

Chapter. The idea of the technique is to project an intensity pattern, through the

grating, onto the sample surface. This is achieved by illuminating the grating with a

parallel beam of light, thus resulting in different diffractions orders being generated

inside the thin film. Depending on the refractive index of the thin film, the k-vectors

---

[1] Normalised units indicate the wave number in free space.

of these diffracted orders may be greater than unity. By using thin film with high

refractive index, the resolution performance achievable can be substantially better

than that produced by the conventional SIM. The phase stepping process required for

the reconstruction algorithm is realised by changing the angle of the illumination

light beam, which will have the effect of shifting the intensity pattern at the sample

surface.

The various diffracted orders in the thin film will interfere, resulting in a

periodic intensity pattern. At the sample plane, in 1D form, this pattern can be written

as

$$I_m(x) = 1 + g_1 \cos(k_0 x + \theta_m) + g_2 \cos(2k_0 x + 2\theta_m) + \cdots \qquad (3.1)$$

where the g's and k_0 are the modulation depths and the k-vectors of the components

making up the intensity pattern. The phase values θ_m of the harmonics are dependent

on the angle of the illumination beam, and changing the latter will therefore effect

the required phase stepping. The modulation depths g's are determined by the relative

phases of the diffraction orders at the sample, which are functions of the grating

period T_g, the refractive index of the thin film, its thickness d, and also the aspect

ratio of the grating. This last point will be discussed further in the grating design

section 4.2.1. It is worth noting that the modulation depth is also a function of ϕ, the illumination angle of the light beam. However, for small variation in ϕ, which will be the case in our experiments, any changes in *g's* will be small and the effect can be ignored. Simulations will be presented to verify this point in Appendix A.

Referring to Eq. (2.4), the frequency spectrum of the PGSIM image can be rewritten as:

$$\hat{O}_m(f_x) = \hat{H}(k_x)[\hat{S}(k_x) + g_1\hat{S}(k_x - k_0)e^{i\phi_m} + g_1\hat{S}(k_x + k_0)e^{i\phi_m}$$
$$+ g_2\hat{S}(k_x - 2k_0)e^{i2\phi_m} + g_2\hat{S}(k_x + 2k_0)e^{i2\phi_m}] \qquad (3.2)$$

The index m indicates the phase-step order of the illumination. The first term inside the brackets in Eq. (3.2) corresponds to the sample spectrum captured with a conventional imaging system. The other terms are due to the structured illumination, and contain spatial frequency components of the sample originally outside the aperture of the system. To extract and separate the various terms, phase stepping is employed. For ease of discussion, we will assume the system to be 1D, and only the zero, first and second grating orders are present. The analysis can readily be extended to 2D and include higher diffracted orders.

The characteristics of the illumination will be discussed in the next three sections, and the points of consideration are:

- The highest value of *k-vector* achievable

- Filling of the extended effective aperture

- Contrast of the multiple orders

3.1.1 PGSIM producing k-vectors greater than 1

The improvement in the system resolution is due to the fact that the thin film next to the grating can have very high refractive index, and thus is able to support grating vector much greater than 1.

The maximum *k-vecto*r plays an important role because it determines the upper limit of the spatial frequency of the sample that can be captured by the system. Figure 3.2 shows the frequency spectrum of the reconstructed image.
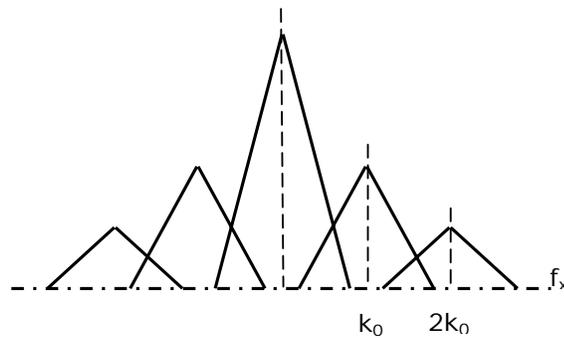

Figure 3.2 system bandwidth extension by projected grating illumination in 1 D

This figure is very similar to figure 2.2 in Chapter 2. k_0 and $2k_0$ are the *k-vectors* of the illumination orders and act as carriers to extend the system

bandwidth. The crucial difference between our system and the conventional SIM is

values of the *k-vectors* that can be present in the eventual frequency spectrum.

With the conventional SIM operating in air, the highest *k-vector* allowed is 1 in

normalised unit. In practice, it is reduced to coincide with the edge of the system

aperture. With our system, the limit of the *k-vector* is determined by the refractive

index of the thin film material, and as will be seen in section 3.5, there are materials

with refractive index 2.5 or greater, this represents the basis of the resolution

improvement of the system.

Figure 3.2 also illustrates the other two important considerations for the

illumination system, namely the relationship between the locations of the *k-vectors*

and the width of the triangles (which is dependent on the aperture of the imaging

system); and the magnitudes of the various *k-vectors*. These two points will be

discussed in the next two sections.

3.1.2 Filling the effective image frequency space - multiple diffracted orders in two directions

When designing the illumination system, the highest *k-vector* is an important

consideration. Beside this, we need also to consider the lower diffracted orders to fill

the frequency domain. For example, in figure 3.2, if we remove the component k_0

and that there are only the zero and the $2k_0$ components, the final image spectrum

will contain no information around k_0. It is therefore essential to pursue not only the

highest *k-vector* but also the number of the lower diffracted orders.

In order to fill the effective frequency space of the reconstructed image, two

important characteristics need to be considered:

1) Multiple fringe orders

The highest grating harmonics provides the highest *k-vector* and multiple

harmonic orders will provide overlapping of spectra centring at each harmonic. This

allows the entire effective image spectrum to be covered. (see figure 3.2). As an

example, if the original system has an NA = 1, and the refractive index of the thin

film is n = 2.5, a minimum of two harmonics is required in order to ensure that there

are no gaps in the spectrum.

2) Two dimensional fringe pattern

Imaging is usually a 2D phenomenon and therefore we need to fill a 2D

frequency space. Using the sample holder described above 2D operation is

accomplished readily, as the grating may take the forms of square, equilateral

triangle or even more complicated shape. It is important to note, however, using a

large number of illumination harmonics to fill the frequency space will have its

drawbacks.   This is because each additional harmonic will require two phase steps

in order to fulfil the reconstruction requirements. So the actual number of fringe

harmonics used is a compromise between the filling of the frequency space and the

complexity of the phase stepping process and the time required for the experiment.

Figure 3.3 below shows the location of a particular fringe harmonic at 2D frequency

space.

To sum up, we want to collect information which is originally outside system

bandwidth. Multiple orders allow us to collect all signals in the region defined by the

highest *k-vector*, and two dimensional grating structure makes the enhancement more

isotropic. Both of them are necessary to arrive at a final transfer function that is near

ideal.
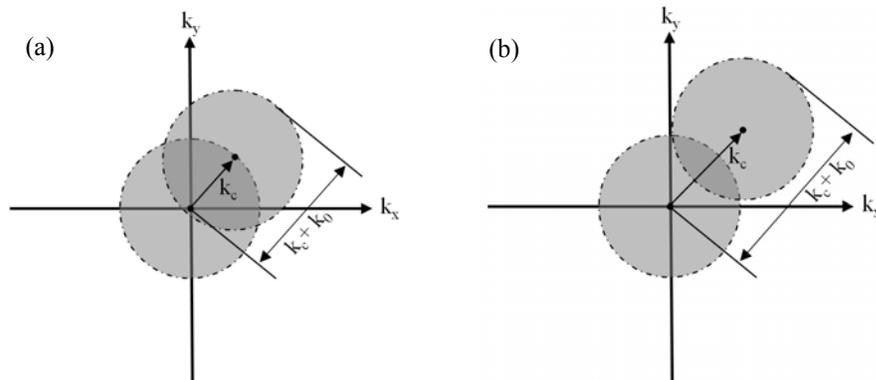
Figure 3.3 (a) Original optical system has bandwidth k_o, and the sinusoidal distribution structured illumination pattern has frequency component k_c. The information can be decoded and restored to its proper position. The bandwidth after reconstruction is $k_o + k_c$, and the max value is 2* k_o, (b) Projected illumination can create high special frequency carrier k_c which is not restricted to the system bandwidth k_o

3.1.3 Talbot effect leading to max contrast and determination of the thin film thickness d

In 1836 Henry Fox Talbot discovered an optical phenomenon and published his experimental result [80]. A diffraction grating was illuminated with white light, and a lens was used to image the grating. It was found that a 'perfectly sharp and well-defined' image appeared even when the observation screen was greatly out of focus of the lens. Furthermore this sharp image repeated itself at regular intervals as the observation distance from the lens was increased. This phenomenon is known as the Talbot effect and the interval where the image repeated itself is called the Talbot distance Z_T.

Half a century later, Lord Rayleigh explained this phenomenon analytically as a consequence of Fresnel diffraction [81], and showed that the Talbot distance Z_T is given by $2T^2/\lambda$, where T is the period of grating and λ the light wavelength. For example, with a wavelength of 632.8nm and a grating pitch of 0.1mm, the Talbot distance is 31.6mm. Rayleigh also pointed out that this effect can be used practically to reproduce a grating by putting photographic film at the Talbot distance of the original grating.

As an aside, the simplicity of self-imaging still attracts many researchers.

Nowadays, the Talbot effect is exploited in a wide variety of applications [82]. It has

been used in wave front measurement, interferometry, and image processing [83].

Others have applied the Talbot effect to perform ranging and depth measurement [84].

Here we combine this self-image effect with lithographic fabrication of nano-scale

structure to create high spatial frequency illumination.

We will now consider a field distribution u(x, y, z) at a certain distance z from

the grating. The illumination is taken as a plane wave and the spatial frequencies of

the grating are assumed small so that paraxial approximation can be used throughout.
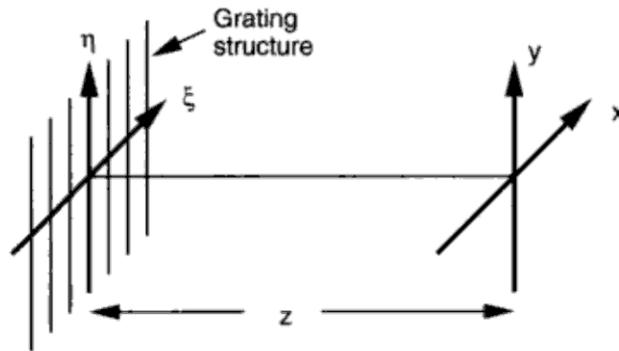
Figure 3.4 Geometry for diffraction calculation.

The amplitude u(x, y, z>0) can be expressed as a convolution of the

distribution immediately behind the grating and the impulse response h(x,y,z) of free

space propagation:

$$u(x,y,z_1) = \int_{-\infty}^{\infty} u(\xi,\eta,\varsigma = 0)h(x-\xi,y-\eta,z_1)d\xi d\eta \qquad (3.3)$$

where z_1 is the distance of observation. In the Frequency domain, the convolution

changes into a product of the transforms:

$$\tilde{u}(k_x, k_y, z_1) = \tilde{u}(k_x, k_y, 0)\tilde{h}(k_x, k_y, z_1) \qquad (3.3(a))$$

and the propagation factor can be expressed as:

$$\tilde{h}(k_x, k_y, z) = \exp(iz\sqrt{k^2 - k_x^2 - k_y^2}) \qquad (3.3(b))$$

where k_x and k_y are the wave vectors in the x and y directions. According to our initial assumption, the spatial frequencies along x and y are small compared to the wave factor k. Therefore, the square root in the exponential function of Eq. (3.3(b)) can be approximated by a Taylor series.

$$\tilde{h}(k_x, k_y, z) = \tilde{h}_{lin}(z)\tilde{h}_{par}(k_x, k_y, z) \qquad (3.4(a))$$

Where

$$\tilde{h}_{lin}(z) = \exp(ikz) \qquad (3.4(b))$$

$$\tilde{h}_{par}(k_x, k_y, z) = \exp(-\frac{jzk_x^2}{2k} - \frac{jzk_y^2}{2k}) \qquad (3.4(c))$$

The second term in Taylor series is small enough to be ignored because of the initial assumption (k_x and $k_y \ll k$). This result can be interpreted in the following way: the phase of the first term $\tilde{h}_{lin}(z)$ is a function of z only and is independent of k_x and k_y. The second phase factor contains the parabolic approximation of the light propagation, and for the on-axis case the Fresnel diffraction can be recognized.

For simplicity we will examine a 1D grating, which has periodic amplitude distribution in the x direction, the wave vectors consist only of discrete frequencies

$$k_x = m \times \frac{2\pi}{L} \qquad\qquad m = 0, \pm 1, \pm 2 \cdots \tag{3.5}$$

Self-imaging means that the components corresponding to the *k-vectors* in Eq. (3.5) have phase modulations equal to zero or multiples of 2π. In other words, $\tilde{h}_{par}(k_x, k_y, z) = 1$. Substituting Eq. (3.5) into Eq. (3.4(c)) yields the self imaging condition

$$\left(m \frac{2\pi}{L} \right)^2 \frac{z\lambda}{2\pi} = 2\pi l \tag{3.6}$$

where *m* and *l* are both integers. Finally we find the Talbot distance

$$z_T = l \frac{2T^2}{\lambda} \qquad\qquad l = 1, 2, 3,..... \tag{3.7}$$

Supposing the distance behind the grating satisfies the Talbot condition which is equal to a multiple of the Talbot distance, then the intensity pattern observed at this location can be interpreted as a perfect image of original grating because the transfer function is unity (apart from a linear phase factor). It is important to appreciate that this exact image is produced without the help of any lenses. Figure 3.5 shows simulation result of the diffraction pattern along z direction behind a 3μm period 1D grating and it shows the intensity distribution as a periodic function of the distance z. The Talbot image is clearly seen at Z_t. Also seen are the patterns at locations *(m + 1/2)Z_T* from the grating. They are also the exact replicas of the original grating by are

shifted by half a period laterally.
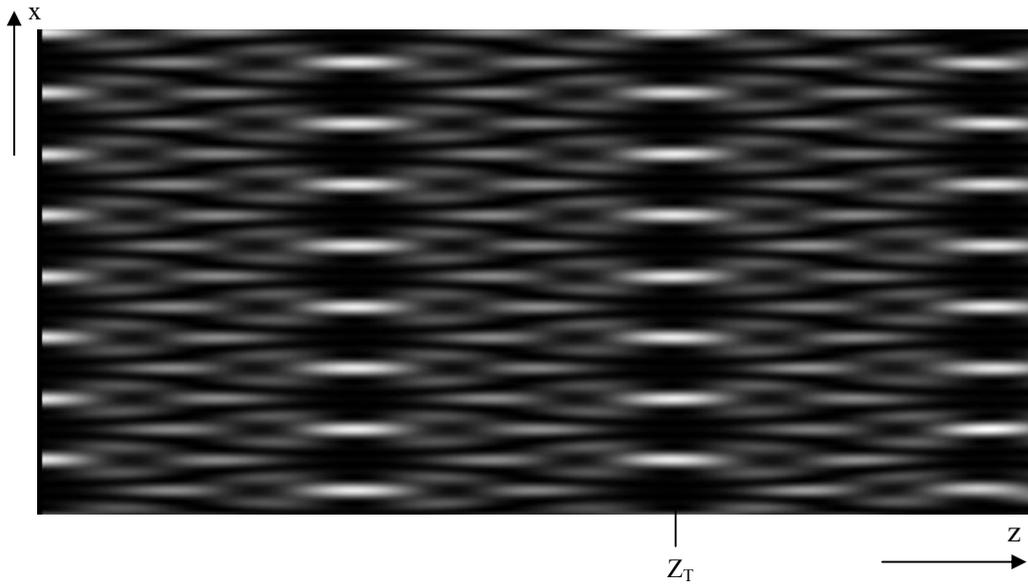
Figure 3.5 Intensity patterns behind the grating with $\lambda = 532$ nm and the on-off ratio of the grating equals to 80%-20%.

The Talbot effect applies equally to 2D gratings. Figure 3.6 shows simulations of the intensity patterns at different distances behind a square grid pattern of 3 μm period.
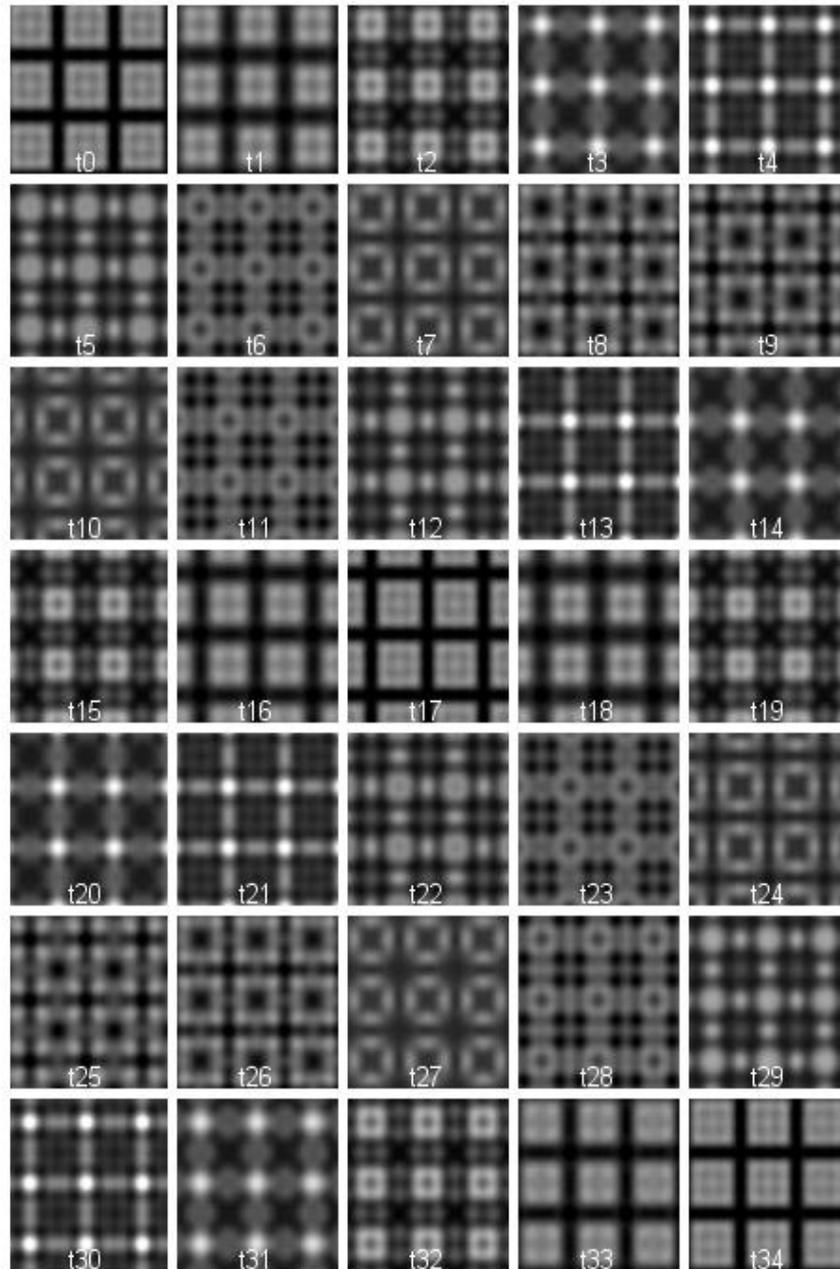
**Figure 3.6** The numerical simulation of intensity patterns at different locations. The period of the grating is 3μm, with an on-off ratio of 20%-80%. The wavelength is 532nm. Z_T is equal to 33.8 μm. The image t0 is taken immediately behind the grating. Other images are taken at regular intervals, $Z_T/34$ apart. The images t0 to t34 therefore cover exactly one Talbot distance. T17 is the image at half the Talbot distance, which is the same as t0 but with a lateral shift of half of the period.

(a)

$Z \approx 0 \mu m$

(b)

$Z = 8 \mu m$

(c)

$Z = 17 \mu m$

(d)

$Z = 32 \mu m$

(e)

$Z = 34 \mu m$
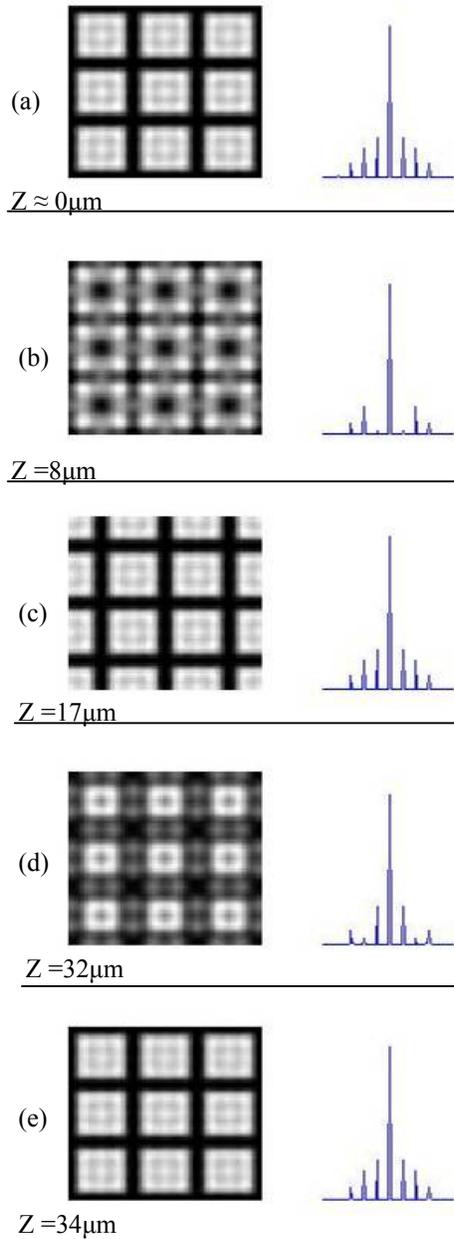
Figure 3.7 Contrast of different diffracted orders at various thin film thickness

Returning to our system, selecting the thickness of the thin film d is tantamount to deciding which particular pattern in figure 3.6 is used for sample illumination. To investigate the choice of d, we need to examine the spectra of the intensity patterns in figure 3.6, as the strengths of the *k-vectors* of the fringe

components correspond to the magnitudes of the Fourier components. Figure 3.7 shows five of the intensity patterns from figure 3.6: t0, t8, t17, t32 and t34. Next to each pattern is the corresponding magnitude spectrum along the x-direction. The first thing to notice is that, by choosing a particular intensity pattern, the magnitude of a certain frequency component can be suppressed. Gaps may therefore appear in the image spectrum if that particular pattern is used for illumination purpose. Another point to notice is that patterns (a), (c) and (e) produce the same magnitude spectrum which is as expected, since they are either the repeated patterns or simply shifted laterally.

The differences between grating diffraction orders and intensity orders should be clarified. Light propagation obeys conservation of energy, and as a field propagates, the energy is redistributed and different intensity patterns are produced. The amplitude of each grating diffraction order, however, remains the same during propagation, and different phase delays are added to the orders when propagating. Therefore, the intensity patterns are due to the interference of the various diffraction orders, and the pattern changes depending on the phase relationships of the diffraction orders.

On its own, we cannot draw any conclusion from figure 3.7 as to which pattern is 'best' for sample illumination, as the latter is usually application related. In

our experiments, we normally aim to use pattern at the Talbot distance.

The preceding discussion demonstrates that, when propagating, periodic wavefront repeat itself at regular intervals, and it is possible to observe the Talbot effect at multiple Talbot distance Z_T. The intensity patterns shown in figure 3.7 contain high spatial frequency components that are not limited by the NA of the imaging system. The Talbot effect is purely a light propagation phenomenon, and the highest spatial frequency component it can afford is limited only by the refractive index of the medium. Taking advantage of this, using the Talbot effect and a high refractive index material, a unique illumination arrangement can be obtained. Once the illumination pattern is determined, we need to consider the phase stepping aspect of the system. This would allow the illumination pattern at the sample plane to change, thus allowing reconstruction of the final image to be accomplished. In this section, the oblique illumination of the sample unit will be discussed and we will demonstrate the lateral shift of the intensity pattern by changing the illumination angle.
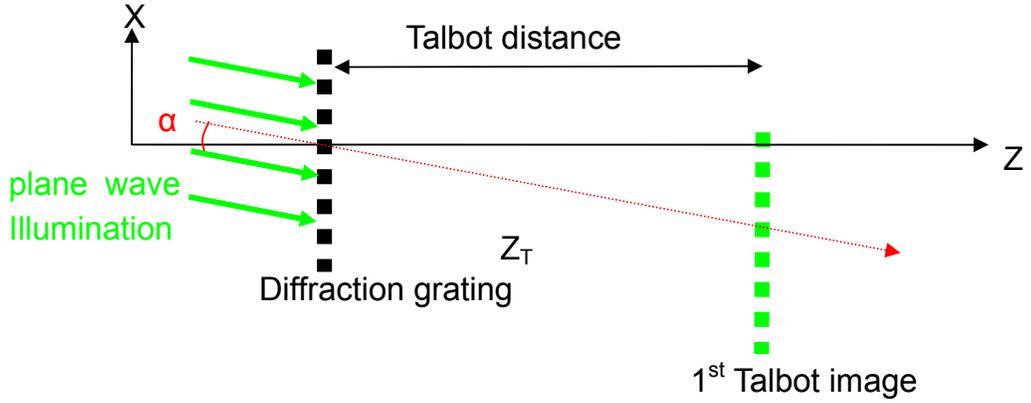
Figure 3.8 Off-axis configurations

We now consider the case when the incident angle of the illumination is α [85-86]. For the sake of simplifying the analysis, we restrict our discussion to the one-dimensional case, i.e. the grating and the incident angle are both independent on y (Figure 3.8).

Due to the off-axis propagation of the incident wave, the spatial frequency spectrum of the field behind the grating is centred around the incident plane wave, $k_i = k\sin(\alpha)$. Therefore, it is convenient to perform the coordinate transformation

$$k'_x = k_x - k_i \tag{3.6}$$

Eq. (3.2.(b)) then becomes

$$\tilde{h}(k'_x, z) = \exp(iz\sqrt{k^2 - (k'_x + k_i)^2})$$

$$= \exp(izk\cos(\alpha)\sqrt{1 - \frac{1}{\cos^2(\alpha)}\frac{k'^2_x}{k^2} - 2\frac{\sin(\alpha)}{\cos^2(\alpha)}\frac{k'_x}{k}}) \tag{3.7}$$

According to our assumptions, α must be small and k'_x is much smaller than k.

The exponential in Eq. (3.7) can therefore be expanded to yield

$$\tilde{h}(k'_x, z) = \tilde{h}_{lin}(k'_x, z)\tilde{h}_{par}(k'_x, z) \tag{3.8}$$

Where

$$\tilde{h}_{lin}(k'_x, z) = \exp\left[\underbrace{ikz\cos(\alpha)}_{\text{Const. phase}} - \underbrace{ik'_x z \tan(\alpha)}_{\text{Lateral shift}}\right] \tag{3.8 (a)}$$

$$\tilde{h}_{par}(k'_x, z) = \exp\left[-\frac{ik'^2_x z}{2k\cos^3(\alpha)}\right] \tag{3.8 (b)}$$

Comparing Eq.(3.3) and Eq.(3.8), the function $\tilde{h}_{lin}(k'_x, z)$ includes one more term which corresponds to a lateral shift in the space domain and is caused by the off-axis wave propagation. From Appendix A, the nonlinear term $\tilde{h}_{par}$ can be ignored if the incident angle α is smaller than 5 degrees.

The lateral shift is proportional to the observation distance z and the illumination angle. By adding a phase gradient to the incident beam we can simulate oblique illumination.
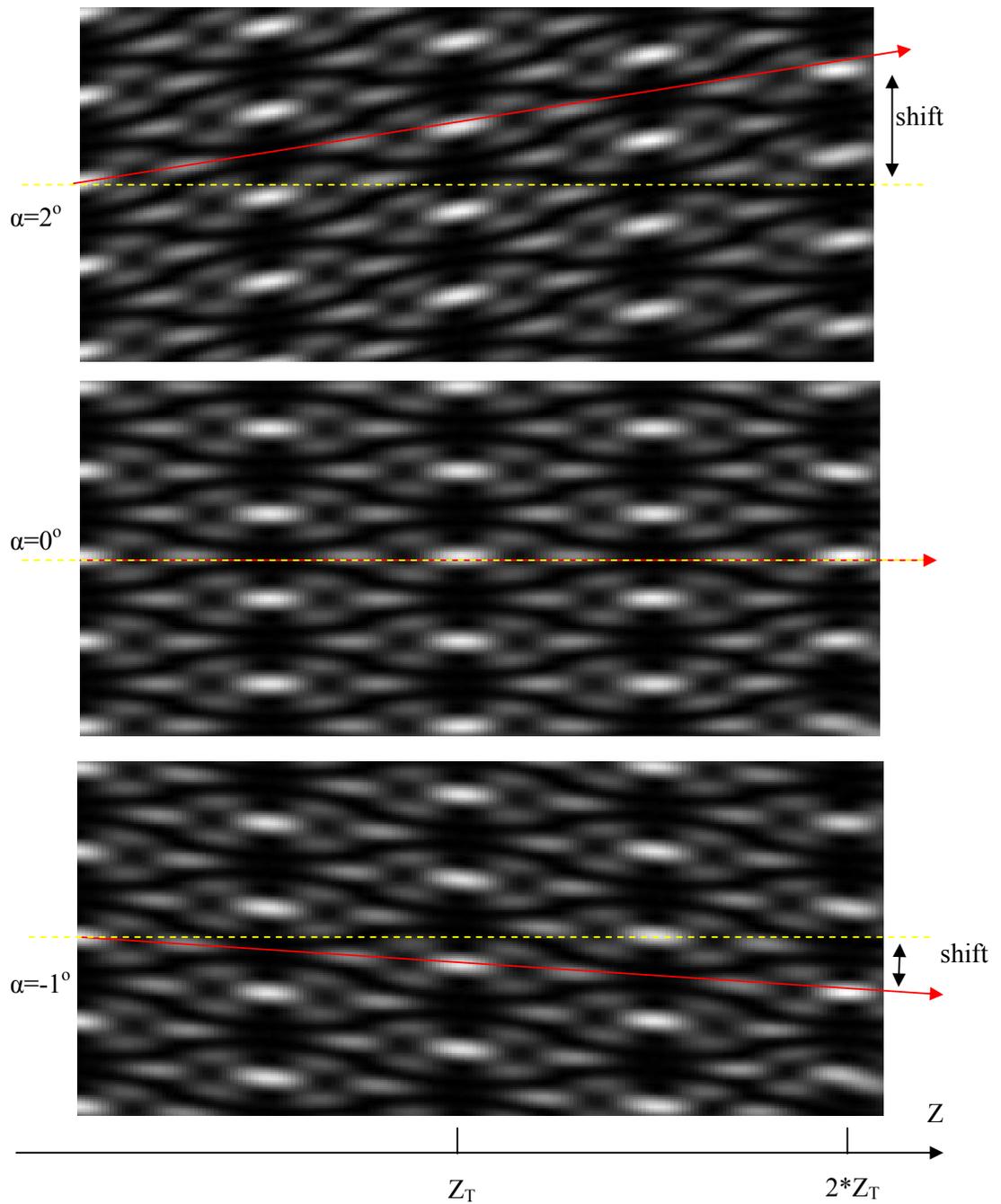
Figure 3.9 The Talbot Carpet in different incident angle. The yellow line is the reference to indicate normal incident. The red line shows the self-image shift.

Figure 3.9 shows the lateral positions of the light pattern for $\alpha = 2^{o}$, 0° and -1°.

The shadowlike projection effect is readily understood for the self-imaging

phenomenon. In daily life, the shadow of an object is changed according to the

direction of the light source. For a small scan angle, this approximation holds and we can take the image in the Talbot distance as a 'shadow' of the original grating. By controlling the incident angle, we can move the diffraction pattern. We can then conclude that the self-image under oblique illumination is a good way to accomplish the phase stepping.

In the case when small angle of α cannot be assumed, it will then be important to consider the effects of the scan on the intensity pattern, or more explicitly, its effects on the illumination orders, both magnitudes and phases. More generally, the magnitudes of the various orders will be a function of the scan angle, and their phase values will not be linearly related to the sine of the scan angle. This is especially the case when the period of the grating becomes small, which is precisely the requirement for extremely high resolution applications. Under this condition, a more general reconstruction algorithm is needed. This will be presented in section 3.2.

3.1.4 Edge effect

As mentioned previously, self-images of the intensity pattern occur at multiples of the Talbot distance, and in theory, the repeated images provide similar illumination to the sample. However, there are additional factors that govern the choice of the actual separation between the grating and the sample. The first is the amount of

image shift which is given by $z*\tan(\alpha)$ for small α. This implies that a large z value is desirable as it reduces the required scan angle α. The second factor is the so called edge effect, which places an upper limit to the z value. We will discuss the edge effect in this section.

The discussion presented up to now is only applicable to infinite gratings and infinite illuminating beam width. More realistic conditions, where both are of finite values, will cause the edge effect. First, we will present the cause of the edge effect. Figure 3.10 shows a schematic representation of the diffracted waves behind the grating with finite dimension. For clarity only the lowest diffraction orders are shown.
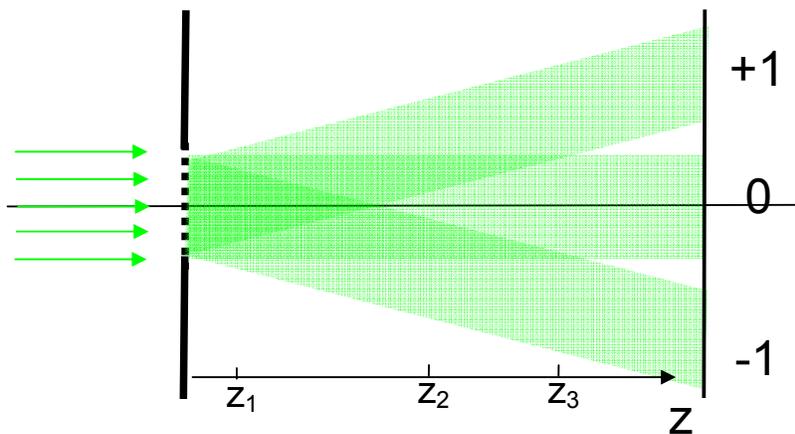
Figure 3.11 Edge effect: separation of the diffracted orders as a function of the sample/grating separation.

Each diffracted order will separate from the others at increasing distance. The

further the observation plan, the smaller is the overlay between the different orders. It means that a complete replication of the original object intensity distribution cannot be achieved. There are three locations indicated in figure 3.11. At Z_1, all three diffracted orders overlap in the central region. When the light reaches Z_2, only two of the three orders overlap each other, so that the resulting pattern is no longer the same as the grating. At Z_3, all orders are separated from each other and there is no diffraction pattern.
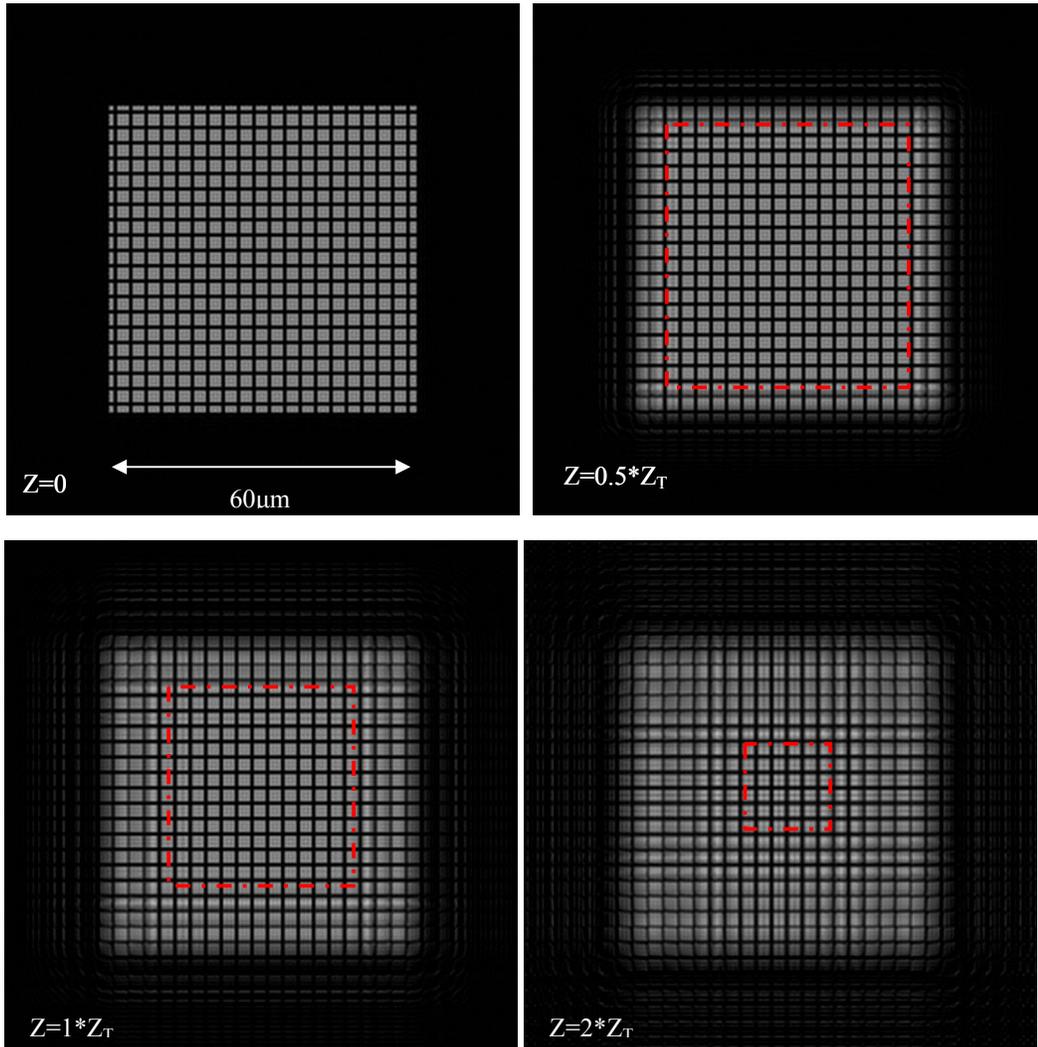
Figure 3.12 Talbot images at different distance. Red line shows the useful region.

Figure 3.12 shows the edge effect using simulated diffraction patterns, originated from a finite grid size, at different distances. The period of the grid is 3μm (80% transparent and 20% opaque) and the total size of grating is 60μm × 60μm. The edge effect can be seen clearly as the separation increase from z = 0, to 0.5, 1 and 2 Talbot distances. From the results the areas overlapped by all the orders are estimated to be 100%, 60%, 34%, and 7.6% for the four cases respectively. These areas are indicated by the red dashed lines in the figures.

Using geometrical optics, the amount of overlap as a percentage of the original grating size, for different grating unit parameters are calculated and shown in Table 3.1.

T z	1μm			2μm			3μm			5μm		
	n=1.5	2	2.5	1.5	2	2.5	1.5	2	2.5	1.5	2	2.5
10μm	85.8	89.4	91.5	92.9	94.7	95.7	95.3	96.5	97.2	98.6	98.9	99.1
20μm	71.6	78.7	82.9	85.8	89.4	91.5	90.5	92.9	94.3	97.2	97.9	98.3
50μm	29.1	46.8	57.4	64.5	73.4	78.7	76.4	82.3	95.8	92.9	94.7	95.7
100μm	NO	NO	14.9	29.0	46.8	57.4	52.7	64.5	71.6	85.8	89.4	91.5

Table 3.1 overlay region calculation. 2nd orders are taken into account with wavelength = 532nm, NO: no overlap, T: grating period, z: separation between grating and sample, n: refractive index of the medium.

From the discussion above, it is obvious that the separation between the

grating and the sample should be small to ensure a sufficiently large overlapped

region. However, it should not be too small otherwise a large scan angle is needed for

the illumination to produce the required lateral shift of the pattern. This trade-off will

be considered in the practical design in Chapter 4.
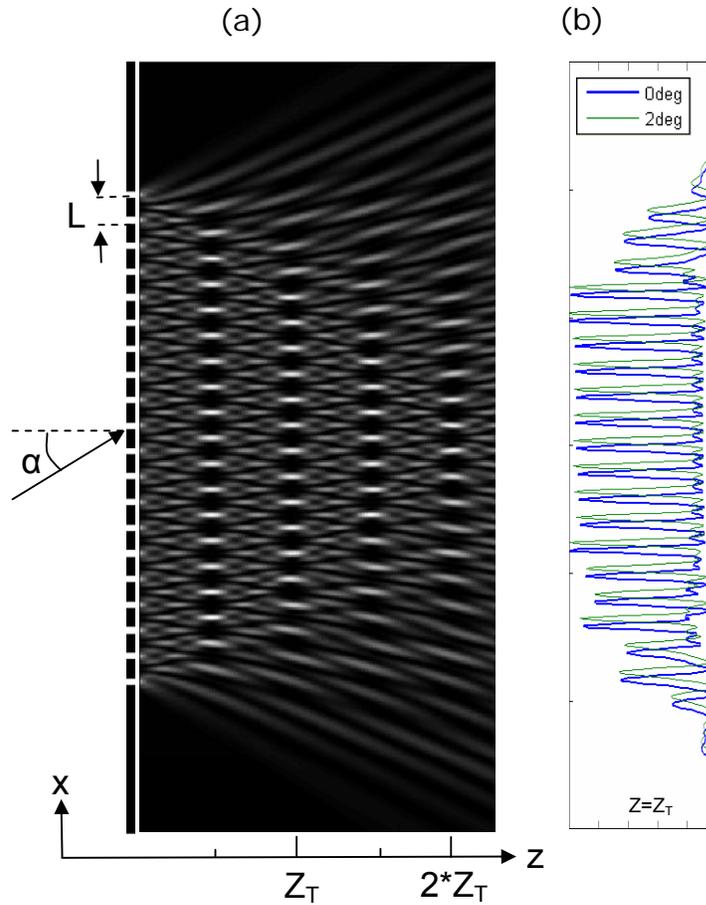
Figure 3.13 Illustration of self-imaging property of grating of finite size.

Figure 3.13 (a) shows the simulation of the intensity pattern as a function of z,

with parameters $T = 1\mu m$ (200nm transparent), $\lambda = 532nm$, $n = 2.5$ (refractive index

for TiO_2) and $\alpha = 0^o$ (normal incident). Note the self-images appearing at multiples of

the Talbot distance and the reduction in the overlapped region along the propagating

direction. Figure 3.13 (b) shows profiles across the intensity pattern at $z = Z_T$, for

scan angles $\alpha = 0^o$ and $\alpha = 2^o$, the lateral shift is apparent.

To summarise, we have discussed in detail the properties of the key

component of the technique, namely the proximity grating unit. The characteristics of

the unit have been investigated in order to ensure the proper operation of the system.

These include the shape and period of the grating and their effects on the

reconstructed image and the associated frequency spectrum. The intensity pattern

resulting from the grating has been explained using the Talbot effect, and the quality

of the intensity pattern has been indicated in terms of the relative strengths of the

illumination orders.

The shifting of the intensity pattern is accomplished by scanning the angle of

the input beam. We have shown the relationship between the scan angle and the

movement of the pattern. Finally we have considered the edge effect caused by

diffraction of the various orders. This edge effect is particularly important for a small

grating and fine grating period.

Compared to optical masks used in the semiconductor industry, the

manufacturing of the grating for this system should be relatively straightforward. The

idea of projecting a very fine intensity pattern onto the sample, with illumination

orders much higher than the bandwidth of the optical system, is therefore entirely

feasible. In the next section, we will examine the reconstruction algorithm required

for the technique.

3.2 Reconstruction Algorithm for projected illumination

Once we have accomplished the high spatial frequency illumination and the

required phase stepping, the next step is to perform the high resolution image

reconstruction. This reconstruction contains two main parts. The first involves

recovering the spatial frequency components of the object associated with the various

illumination orders. A general algorithm will be presented which is independent of

the linearity between the scan angle α and the shift of the intensity pattern. The

second part will shift the recovered spatial frequency components to the appropriate

locations so that high resolution images can be obtained.
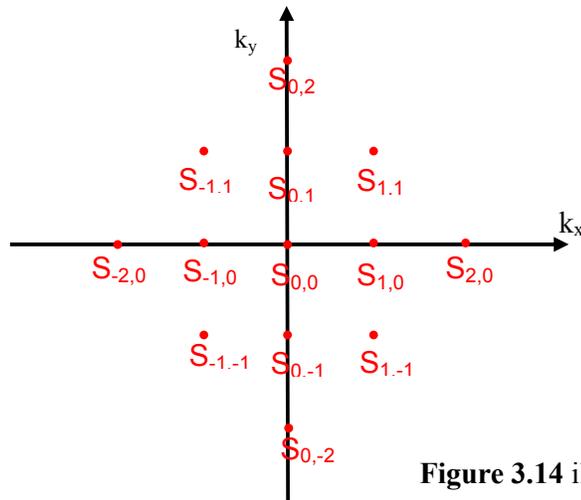
Figure 3.14 illumination orders

90

As an example, we will use illumination orders shown in figure 3.14 to illustrate

the reconstruction algorithm. The rationale behind such a pattern will be made clear

in section 3.4. Similar to the process used in Chapter 2 for the original SIM system, a

matrix equation can be written for the present case:

$$
\begin{bmatrix} \hat{O}_1(f_x,f_y) \\ \cdot \\ \cdot \\ \cdot \\ \hat{O}_m(f_x,f_y) \end{bmatrix} = \begin{bmatrix} C_{11} & C_{12} & \cdot & \cdot & \cdot \\ C_{21} & \cdot & \cdot & \cdot & \cdot \\ \cdot & \cdot & \cdot & \cdot & \cdot \\ \cdot & \cdot & \cdot & \cdot & \cdot \\ \cdot & \cdot & \cdot & \cdot & C_{qm} \end{bmatrix} \begin{bmatrix} \hat{S}_{0,0} \\ \hat{S}_{1,0} \\ \hat{S}_{-1,0} \\ \cdot \\ \cdot \end{bmatrix} \qquad (3.9)
$$

$$\hat{O}(m \times 1) \qquad\qquad C(m \times q) \qquad\qquad \hat{S}(q \times 1)$$

where m is the total number of acquired images and q is the number of illumination

orders used in the system. It should be emphasised that the minimum number of

required images m should be equal to q, the number of illumination orders, which in

this case is 13. The first column vector $\hat{O}_m$ contains the Fourier transforms of the

images obtained at each phase step. The matrix C contains information related to the

phase stepping process with $C_{i,j} = a_{ij}e^{i(\phi_{ij}+\varphi_{ij})}$, where ϕ's and φ's are the phase

step values along the x and y direction respectively. $\hat{S}_{i,j}$ contains the frequency

components of the object associated with the various illumination orders and are the

terms that we want to recover.

For general purpose, these phase values in the above equations are not assumed

to be regular with respect to the phase steps. In addition, the magnitudes a_{ij} of the

illumination orders are also assumed to be dependent on the scan position. Eq (3.9) is therefore a general algorithm and can be employed in situations where the phase stepping process is irregular but known. This is important as when the grating period is small, say below 1μm, both the phase step and the magnitude of the illumination order can become nonlinear with the scan angle α.

To recover the components $\hat{S}$ from Eq (3.9), the inverse to the matrix C, or more generally, its pseudo inverse is taken:

$$\hat{S} = C^{+1} \times \hat{O}$$

or

$$
\begin{bmatrix} \hat{S}_{0,0} \\ \hat{S}_{1,0} \\ \hat{S}_{2,0} \\ \cdot \\ \cdot \end{bmatrix} = \begin{bmatrix} C_{11} & C_{12} & \cdot & \cdot & \cdot \\ C_{21} & \cdot & \cdot & \cdot & \cdot \\ \cdot & \cdot & \cdot & \cdot & \cdot \\ \cdot & \cdot & \cdot & \cdot & \cdot \\ \cdot & \cdot & \cdot & \cdot & C_{qm} \end{bmatrix}^{+} \times \begin{bmatrix} \hat{O}_1 \\ \hat{O}_2 \\ \hat{O}_3 \\ \cdot \\ \cdot \end{bmatrix}
$$

$$\hat{S}(q \times 1) \qquad C^{+}(q \times m) \qquad \hat{O}(m \times 1) \qquad (3.10)$$

Solving Eq. (3.10) yields the spatial frequency components associated with the various illumination orders, although they still occupy the same frequency space. They need to be shifted to their proper positions before the final high resolution image can be obtained. The results of the shifting of the frequency components are illustrated in Eq (3.11):

$$\hat{S}_{0,0} \rightarrow S_1 = \hat{H}(k_x, k_y)\, \hat{S}(k_x, k_y)$$

$$\hat{S}_{1,0} \rightarrow S_2 = \hat{H}(k_x - k_0, k_y)\, \hat{S}(k_x, k_y) \qquad \hat{S}_{2,0} \rightarrow S_3 = \hat{H}(k_x - 2k_0, k_y)\, \hat{S}(k_x, k_y)$$

$$\hat{S}_{-1,0} \rightarrow S_4 = \hat{H}(k_x+k_0, k_y)\, \hat{S}(k_x, k_y) \qquad\qquad \hat{S}_{-2,0} \rightarrow S_5 = \hat{H}(k_x+2k_0, k_y)\, \hat{S}(k_x, k_y)$$

$$\hat{S}_{0,1} \rightarrow S_6 = \hat{H}(k_x, k_y-k_0)\, \hat{S}(k_x, k_y) \qquad\qquad \hat{S}_{0,2} \rightarrow S_7 = \hat{H}(k_x, k_y-2k_0)\, \hat{S}(k_x, k_y) \qquad (3.11)$$

$$\hat{S}_{0,-1} \rightarrow S_8 = \hat{H}(k_x, k_y+k_0)\, \hat{S}(k_x, k_y) \qquad\qquad \hat{S}_{0,-2} \rightarrow S_9 = \hat{H}(k_x, k_y+2k_0)\, \hat{S}(k_x, k_y)$$

$$\hat{S}_{1,1} \rightarrow S_{10} = \hat{H}(k_x-k_0, k_y-k_0)\, \hat{S}(k_x, k_y) \qquad \hat{S}_{1,-1} \rightarrow S_{11} = \hat{H}(k_x-k_0, k_y+k_0)\, \hat{S}(k_x, k_y)$$

$$\hat{S}_{-1,1} \rightarrow S_{12} = \hat{H}(k_x+k_0, k_y-k_0)\, \hat{S}(k_x, k_y) \qquad \hat{S}_{-1,-1} \rightarrow S_{13} = \hat{H}(k_x+k_0, k_y+k_0)\, \hat{S}(k_x, k_y)$$

Figure 3.14 shows the regions where the frequency components covered in the frequency domain for the example used above. $\hat{S}_{0,0}$ is the centre of the spatial frequency components obtained with the original system transfer function. All the other $\hat{S}$'s are as described in Eq. (3.11).
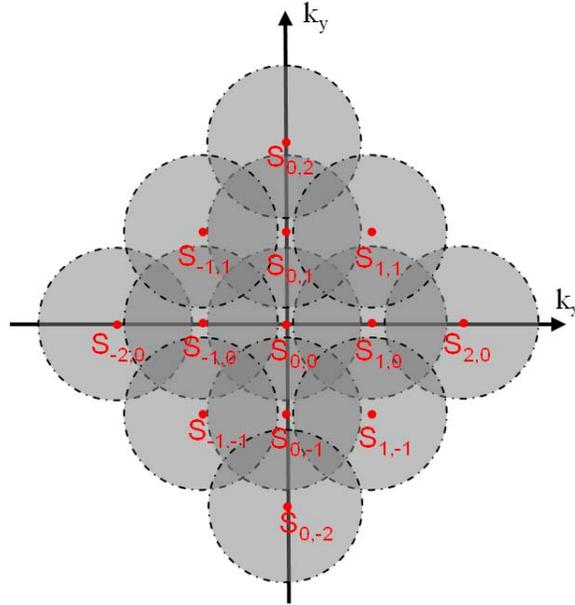
Figure 3.14 After reconstruction, the frequency components are shifted to the proper position.

3.3 Transfer function

The effective transfer function of the final reconstructed image is formed by combining the m different frequency components that are partially overlapped (figure 3.14). The overlap is determined by the radius of the frequency component region (R) and the locations of illumination orders (G). In turn, they are dependent on the original system bandwidth and the grating period. Further processing is used so that the eventual transfer function has the same shape as that of the original imaging system. Simple summation of the different frequency components in figure 3.14 would lead to discontinuities in the final effective transfer function, making it difficult to compare the performance of the system with other techniques. We therefore use a weighted-average function so that the final effective transfer function has the same shape as the original system, as illustrated in figure 3.15.
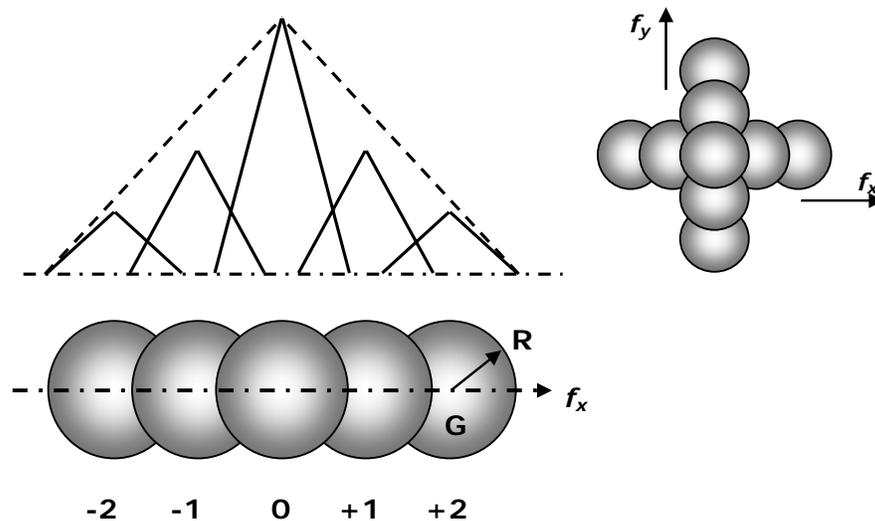
Figure 3.15 Effective transfer function as indicated by the dashed lines.
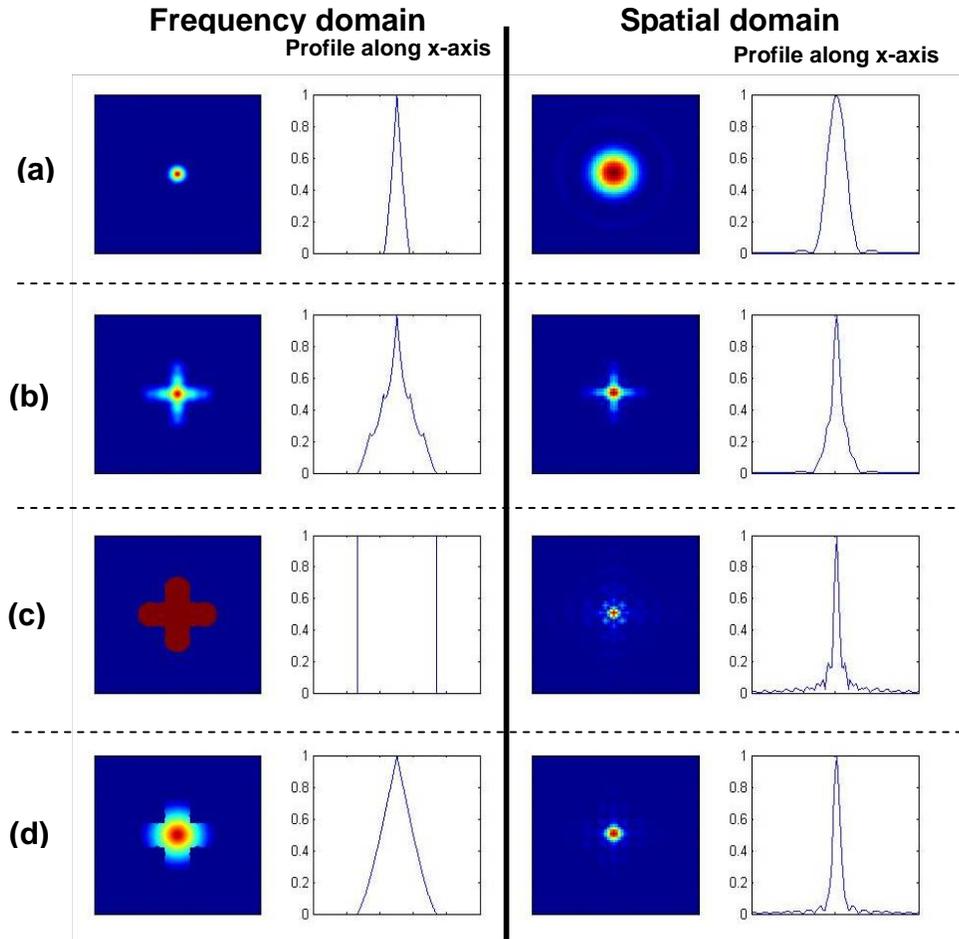
Figure 3.16 Different transfer function and their point spread function

Figure 3.16 illustrates the formation of the effective transfer function using simulated results. The arrangement of the synthetic apertures is as shown in the insert in figure 3.15. The first column shows the normalized 2D transfer functions at various stages of the reconstruction process. Column 2 shows the profiles of the transfer functions along x-axis. Columns 3 and 4 are the corresponding point spread functions and the profiles along x-axis. Row (a) corresponds to the transfer function

and the PSF of the original optical system. (b) shows the results when all the frequency components are summed directly before any scaling process was applied. Because of the arrangement of the synthetic apertures, the point spread function takes on a star-like appearance. Although the resolution enhancement is obvious, the PSF contains a large number of artefacts. In order to reduce these artefacts, the summed transfer function is first scaled to unity in all regions inside the pass band, as shown in row (c). The transfer function in (c) is then multiplied by the Chinese hat function of width $G + R$ (see figure 3.14) and the final effective transfer function is shown in row (d). The ratio of the cut-off frequencies between PGSIM and the original system is 2.5 times and the FWHM of the PSF of each have 2.5 times improvement.

The normalisation function is a weighted-average function. Depending on the actual application, the normalisation algorithm should be based on signal-to-noise ratio (SNR) of the system. Algorithms based on the Wiener deconvolution filter [12] would be suitable for this purpose.

3.4 Simulation results

In this section, computer simulation will be used to show the working of the system. The intensity distribution, or its Fourier transform when appropriate, at each

step of the imaging forming process will be shown. The parameters used for the simulation are:

square grating, period = 3μm, 80% transparent and 20% opaque

wavelength λ = 532nm

material between grating and sample : air

separation between grating and sample: 1 Z_T = 32 μm

numerical aperture of the imaging system: NA = 0.2

For simplicity, the object is assumed to be a point scatterer having the same excitation and emission wavelengths. In the description below, all distances are expressed in normalized unit, NW = λ/NA. Therefore 1NW = 2.66μm. In spatial frequency domain the normalised unit is INW = $(NW)^{-1}$ = NA/λ = 0.38μm^{-1}.

The grating period is chosen so that the first grating harmonic is at ±2NA/λ which is equivalent to the highest grating order that a conventional SIM can accept. In the simulation, we have used up to ±2 grating orders although higher orders are available for use if desired.
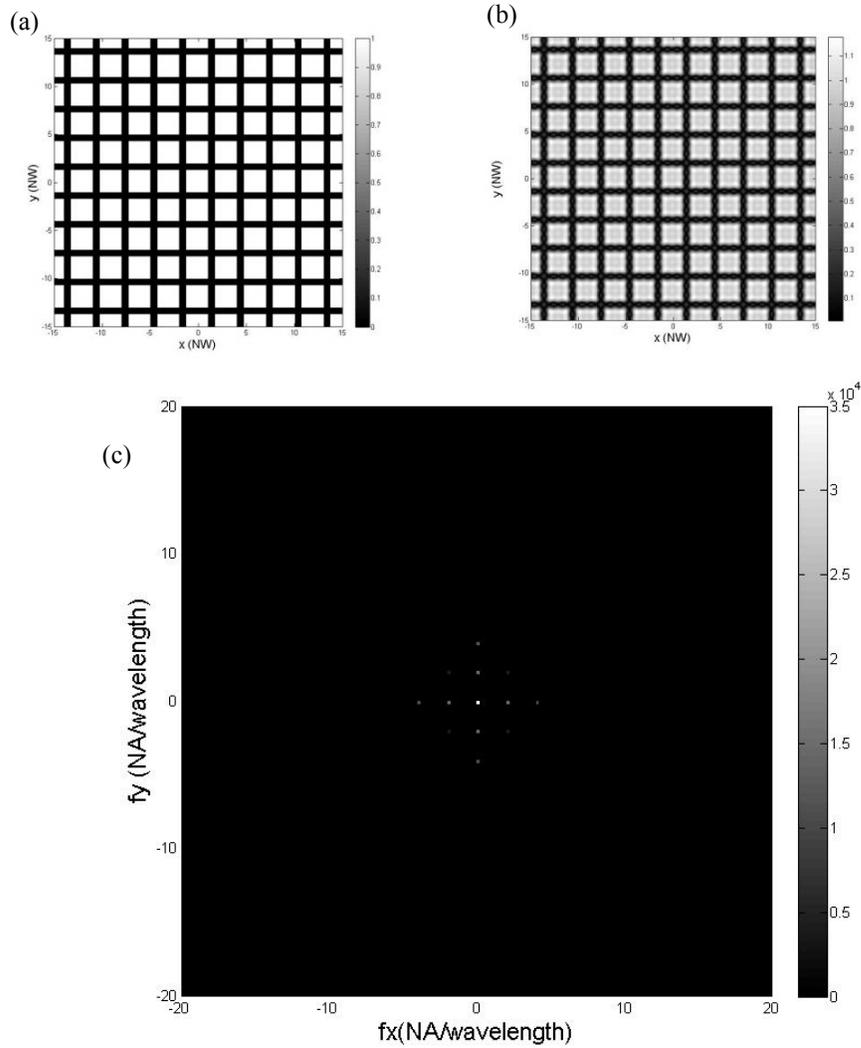
Figure 3.17 (a) Original grating, (b) Simulated projected illumination pattern at one Talbot distance from the grating, (c) Spatial frequency components of the projected illumination pattern.

Figure 3.17 shows the intensity distributions immediately after the grating (a) and at a distance Z_T from the grating (b). Because of the Talbot effect, the distribution is similar to the original grating. Figure 3.17(c) shows that the Fourier transform of the project intensity distribution (b). The figure contains 13 frequency

components (as in figure 3.14) but those at $\pm 45^0$ are very weak. The amplitudes of these components are directly related to the modulation depth of the various orders, and are strongest along the x- and y- directions.

The object is illuminated with this intensity pattern, and multiple images are required for the reconstruction algorithm. With 13 illumination orders, a minimum of 13 phase-shifted images are needed. As mentioned before, changing the incident angle can cause a lateral shift of the illumination, and for a 2D operation, the shifting must be performed in two directions. The final image is obtained by multiplying the object and the illuminations.
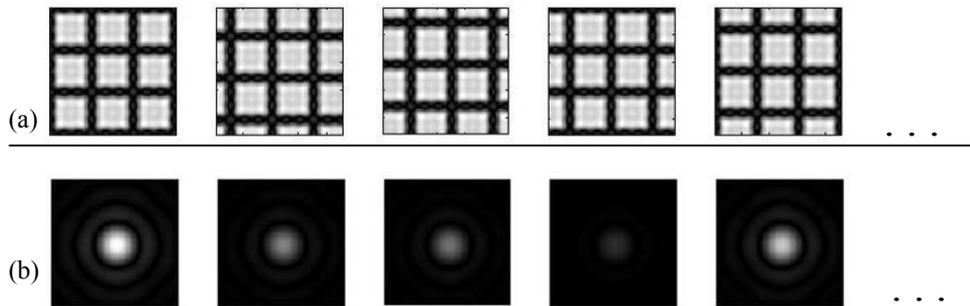
Figure 3.18 (a) illumination patterns at different incident angles. And (b) are the image of point source in the associated illumination patterns. Object position located at the centre of the frame.

Figure 3.18 (a) shows five of the thirteen phase shifted illumination patterns, and the resulting images (b). The variation in intensity of the illumination enables this technique to encode normally inaccessible high spatial frequency information into the images. Even though the size of the particle in each picture remains the same,

the intensity changes due to the different illumination over the sample. This information is used to extend the bandwidth by the reconstruction algorithm.
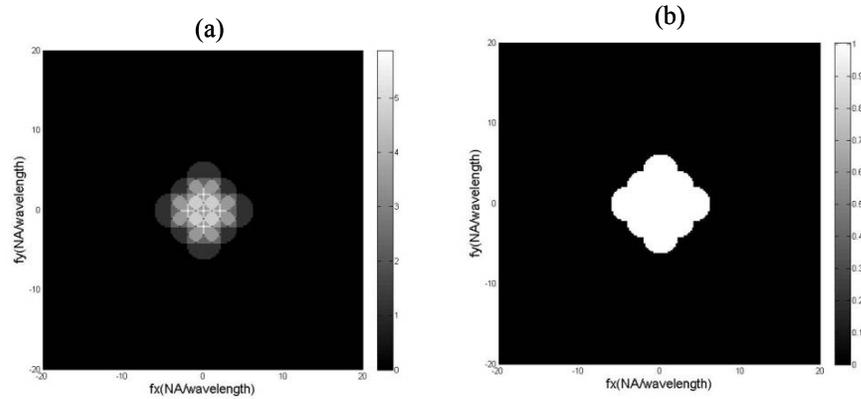

Figure 3.19 (a) sum of all 13 extracted components from reconstruction algorithm. (b) transfer function after weight-average.

After the application of the reconstruction algorithm, as described in section 3.2.1, the thirteen spectra are placed at the correct positions as shown in figure 3.19 (a). Figure 3.19 (b) shows the normalised spectrum before the multiplication of the Chinese hat function. By multiplying figure 3.19 (b) with the Chinese hat, the extended spectrum of the original point object is resulted. Figure 3.20 (a) shows the intensity distribution of the corresponding point image, which is of course the intensity psf of the high resolution system. Figure 3.20 (b) shows the profile of 3.20 (a). Also shown is the profile of the psf obtained using the original system.
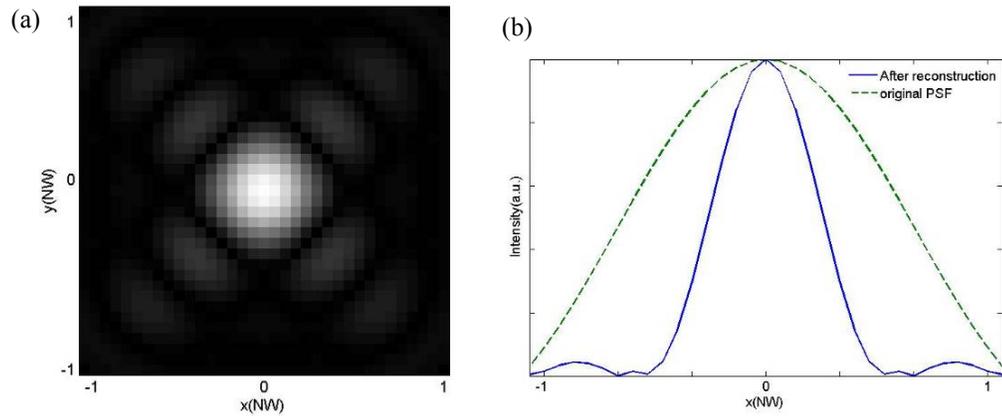
Figure 3.20 (a) Final image. (b)PSF comparison between original optical system and PGSIM.

In this simulation, the highest spatial frequency of illumination used is the 2nd harmonic ($f_x = 2*2NA/\lambda$), and the cut-off is the 2nd harmonics plus original system bandwidth, which equals to $3*2NA/\lambda$ for this example. In other words, the bandwidth is three times of that of the original system, and the PSF is three times smaller (figure 3.20(b)).

Up until now, the concept of projected grating SIM is illustrated by simulation on a point object using a square grating. We now use a more complicated grating structure, namely, a triangular grid, to replace the square grating. The main advantage of the triangular grid is that it provides stronger illumination orders away from the two orthogonal directions, thus offering a more uniform resolution improvement. Figure 3.21 is the work flow of the whole simulation process with a microtubule structure as sample. Red arrows show the PGSIM work flow and the yellow arrow is for the conventional microscopy.
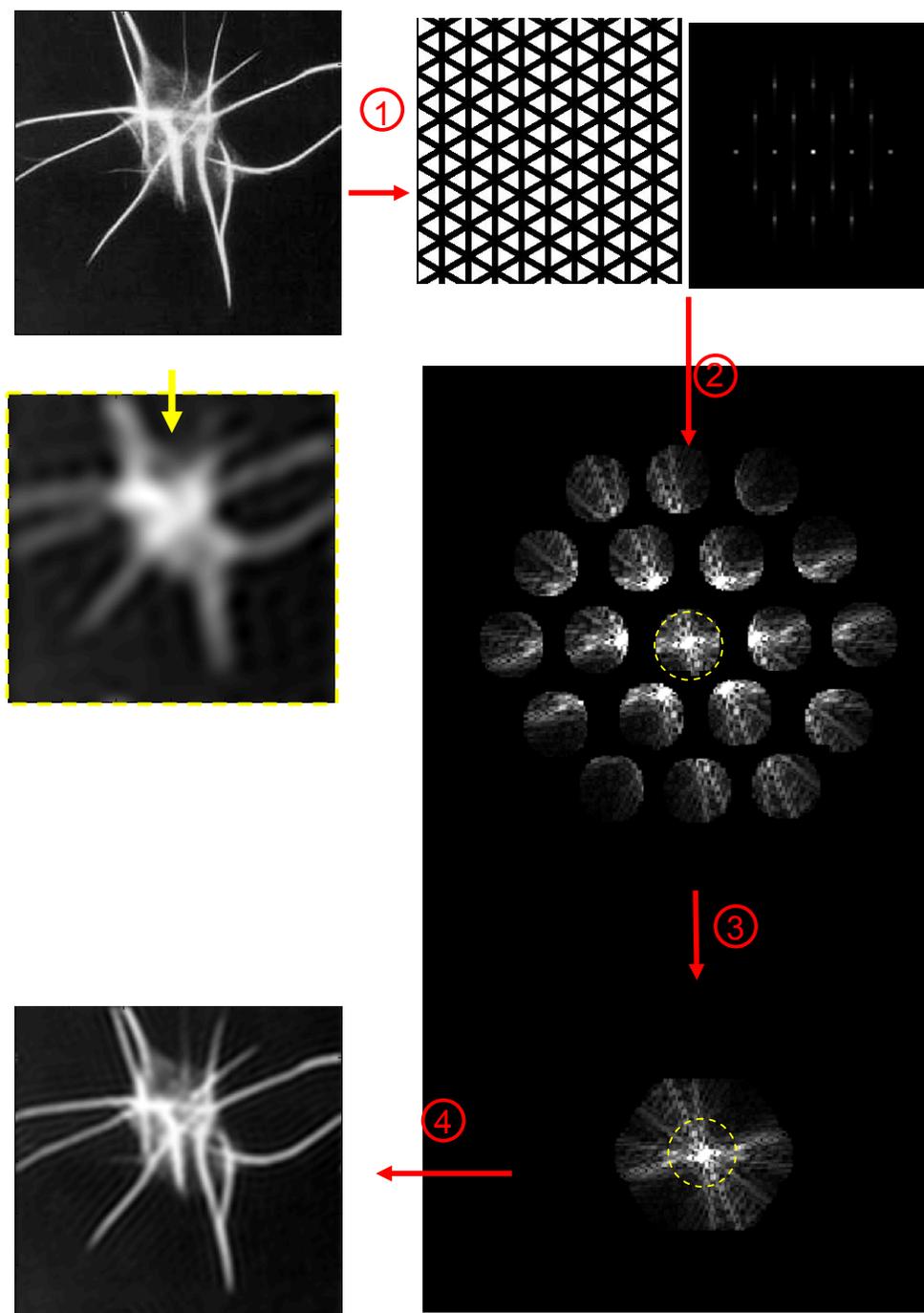
Figure 3.21 work flow of the reconstruction algorithm. Step 1: multiply he object (microtubule) and illumination (triangle). The triangle structure has harmonics along 3 directions in Fourier domain. Phase stepping is needed and images with different illumination lateral shift are recorded. Step 2: Separating the frequency components in the Fourier domain by using the reconstruction algorithm. Step 3: shift frequency components to proper position. The weight-average function is applied to get the

final extended bandwidth. Step 4: inverse Fourier transform back to space domain.

3.5 Discussion and Summary
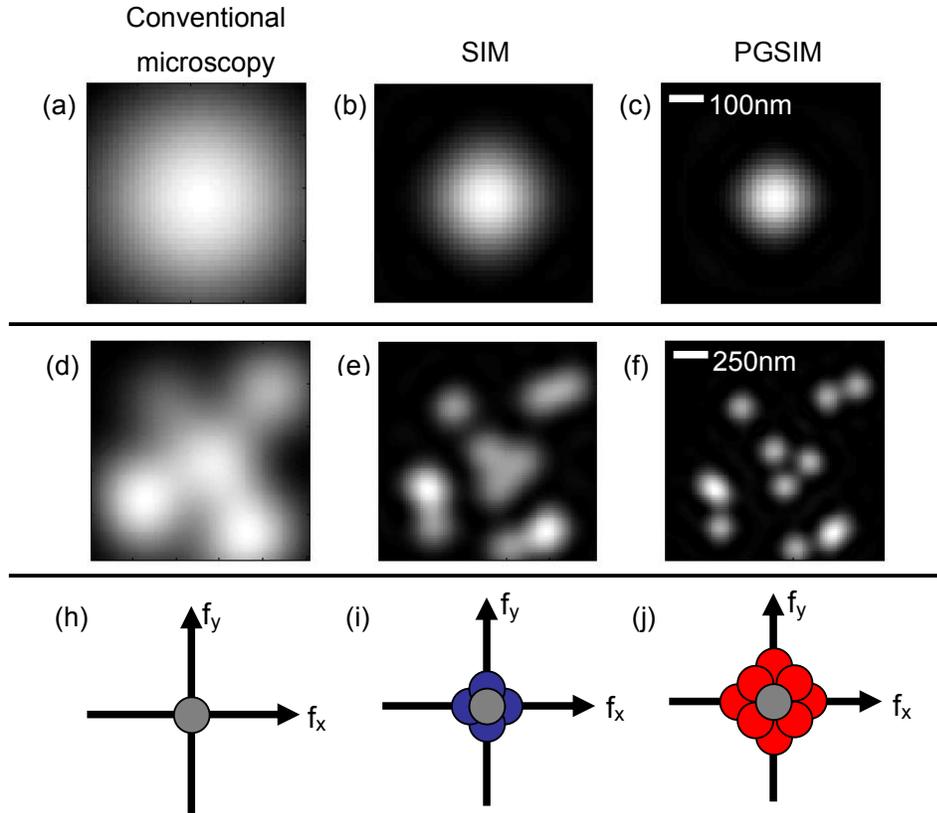
Figure 3.22 point spread function and image performance in different system. (a)conventional microscopy with objective NA=1. (b) Structured llumination microscopy with the same objective. (c) Projected illumination SIM with the same objective. (d~f) imaging performance demonstration for the case (a~c). (h~j) corresponding frequency domain, and the grey circle represents the low-spatial frequency information that can be acquired through conventional microscopy. The blue circles represent the high spatial frequency information coupled into the system through structured illumination. Projected illumination SIM has no barrier and can down convert even higher spatial frequency (red circles).

A novel structured illumination microscopy and the reconstruction processing have been discussed in this chapter. Figure 3.22 shows the relative resolution

performance of a conventional microscope, a SIM microscope and the PGSIM microscope using up to ±2 orders. All three are assumed to have the same initial system NA, and the SIM is assumed to be operating at its limit regarding resolution improvement. As shown, SIM can double the bandwidth compared to the conventional microscope, whereas the PGSIM can have much greater improvement depending on the *k-vector* of the illumination used.

The major advantage associated with PGSIM is that illumination bandwidth is limited by the refractive index of the thin film only. The thin film works as a solid immersion medium, and allows high spatial frequency waves to propagate. It provides conditions to create a very fine illumination pattern.

However, there is still a limit to this technique. The NA of the original imaging system and the maximum grating vector k_g decide the resolution limit. The latter is directly proportional to the refractive index n of the thin film in the sample unit, and is given by

$$k_g = n\frac{2\pi}{\lambda_o} \tag{3.12}$$

where λ_o is the optical wavelength in vacuum. To generate such a grating vector, a grating period of T_g is needed. The minimum grating period is given by

$$T_g = \frac{\lambda_o}{n} \tag{3.13}$$

A short period grating pattern can be projected onto the sample if high index

material is used for the thin film. For an intensity imaging system, the maximum

frequency cut-off is therefore given by

$$
\begin{aligned}
f_{pg} &= 2f_g + 2f_0 \\
&= 2\frac{n}{\lambda_0} + 2\frac{NA}{\lambda_0} \\
&= \frac{2}{\lambda_0}(n + NA) \\
&= \frac{2}{\lambda_0}NA_{eff}
\end{aligned}
\tag{3.14}
$$

where f_g is the spatial frequency corresponding to the grating vector, f_0 is the

coherent frequency cut-off of the system, and NA is the numerical aperture of the

imaging optics. The 2 in the equation accounts for intensity imaging rather than

amplitude. Using immersion oil as the thin film and a dry objective lens, the effective

NA_{eff} is therefore ~ 2.5 instead of 1. In addition, depositing thin solid film, such as

TiO_2, onto the grating with oil immersion imaging optics, an effective NA of 4 is a

distinct possibility. A table of possible NA_{eff} is listed below.

$\mathbf{NA_{eff}}$				
Thin film material Objective lens	Air n=1	Oil n=1.5	Zirconium Oxide ZrO2, n=1.96	Titanium Oxide TiO_2, n=2.4
NA=0.7 (dry)	1.7	2.2	2.66	3.1
NA=1.25 (water immersion)	2.25	2.75	3.21	3.65
NA=1.5 (oil immersion)	2.5	3	3.46	3.9

Table 3.2 PGSIM system effective NA

To sum up, a novel microscope based on the original SIM has been established and is called proximity projection grating structured light microscope. Theoretical analysis of the technique and computer simulations have been presented in this chapter. The resolution improvement comes from the high spatial frequency illumination which is achieved by a proximity grating unit.

In section 3.1, principles of the proximity grating unit have been explained. Using high refractive index thin film, PGSIM system allows illumination with k-vector greater than unity to propagate. The analysis of illumination pattern associated to the thin film thickness has been shown. We have also demonstrated the phase stepping process by changing the angle of the incident beam. The edge effect has been shown to determine the effective illumination area on the sample surface.

A general reconstruction algorithm has been established for the PGSIM in section 3.2. After weighted-averaging of the reconstructed frequency spectrum, an extended bandwidth can be obtained. In section 3.4, by using simulation results we demonstrated the system capability in breaking the resolution limit barrier and achieving an improvement greater than 2. Finally, the limit of this technique has also been discussed, showing that the PGSIM can potentially provide an optical system effective NA equal to 4.

Chapter 4 System implementation

This chapter deals with the hardware development of the projection illumination SIM. The chapter is divided into four parts: illumination method, optics for imaging, sample holder, and layout of the microscope. Comparing with a conventional microscope, the PGSIM differs mainly in the illumination of the sample and the sample holder itself. When combined they provide sample illumination with the appropriate Talbot pattern, and the phase stepping capability which is required for the image reconstruction. The illumination and imaging optics will be discussed first, followed by the grating unit and then the overall system.

4.1 System overview

Generally, a microscopy system can be separated into two parts, illumination and imaging. Both the illumination and the imaging channels need to be designed with care. Figure 4.1 shows the system configuration of the PGSIM microscope. As can be seen the system is divided into three parts: the illumination arm, the sample holder and the imaging arm. It should be made clear that the illumination arm is referred to the illumination of the sample holder, when combined, they form the sample illumination. These three parts will be discussed in Sections 4.1.1, 4.1.2 &

4.1.3.
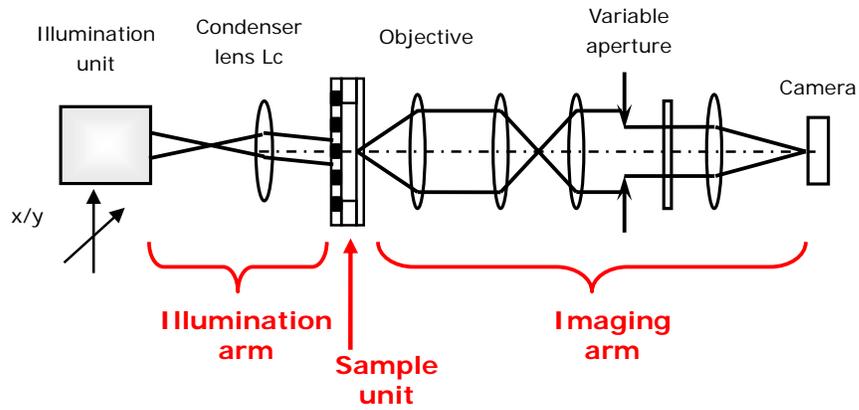
**Figure 4.1** System configuration

4.1.1 Illumination method
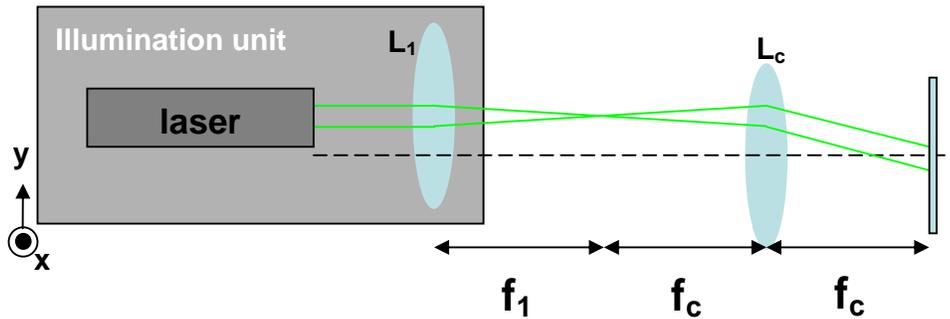
Figure 4.2 illumination arm

Figure 4.2 shows the illumination method. The illumination unit is made up of a laser (frequency doubled Nd:YAG, λ = 532nm, beam dia = 1mm, P = 50mW) and a doublet L_1 (ϕ = 25mm, f = 100mm). Outside of the laser unit is a

108

condenser lens L_C (doublet, $\phi = 25$mm, $f = 30$mm). The main requirement of the illumination arm is to provide off-axis incident beam at the sample holder. As shown, the output beam from the laser unit is focused onto the back focal plane of L_C. Depending on the position of the laser unit relative to the axis of L_C, the arrangement will produce a collimated laser beam incident at the sample holder obliquely.

The laser unit is mounted on a two dimensional motorized positioning stage (PI M-112.1DG, range = 25mm, repeatability = 0.1μm), allowing it to be translated in the x-y plane with high degree of accuracy. In effect a movable point source at the back focal plane of L_C is created. After the condenser lens, a parallel beam is formed with controllable angle, both in azimuth and elevation.

The sample surface should be put at the focal plane of the condenser lens, in order for the illumination to maintain uniformity when the light beam changes in angle, although in practice this does not make a great deal of difference as the sample unit is very thin.

In addition, the lenses L_1 and L_c also form a beam expender. The expanded laser beam should be large enough to match the full field of view, but not too large to reduce significantly the optical intensity. The magnification provided by the two lenses is:

$$M = \frac{f_c}{f_1} \tag{4.1}$$

In the system, $f_1 = 100$mm and $f_c = 30$mm are chosen, giving a magnification M = 0.3. The beam size after the condenser lens is therefore 300μm. This value is sufficient for the system, as the field of view used is usually around 100μm.

The diameter of the condenser lens L_c is 25mm. The absolute maximum in terms of scan angle it can provide is therefore $\pm 24^o$, if the effects of aberrations are ignored. The scan angle required for the phase stepping is around $\pm 3^o$ and is well within the capability of the arrangement.

To set up the illumination part practically, a reverse procedure is used. Once the sample location is fixed in the system, it is used as the reference and the condenser lens is set next. A parallel beam with large beam size is used to focus on the sample surface via the condenser. The position of the condenser lens is adjusted and considered corrected when the reflected beam is collimated through the condenser a second time when observed using a shear plate collimation tester (Melles-Griot, 09SPM001).

The next step is to set the laser unit. The key point is to set the separation of lenses L_1 and L_c, so that a parallel beam into L_1 will come out of L_c parallel. The shear plate is used normally for this purpose. However, as the beam size is reduced to 0.3mm, it is too small for the shearing plate to function. So we simply observe the beam at a far distance to judge its collimation.
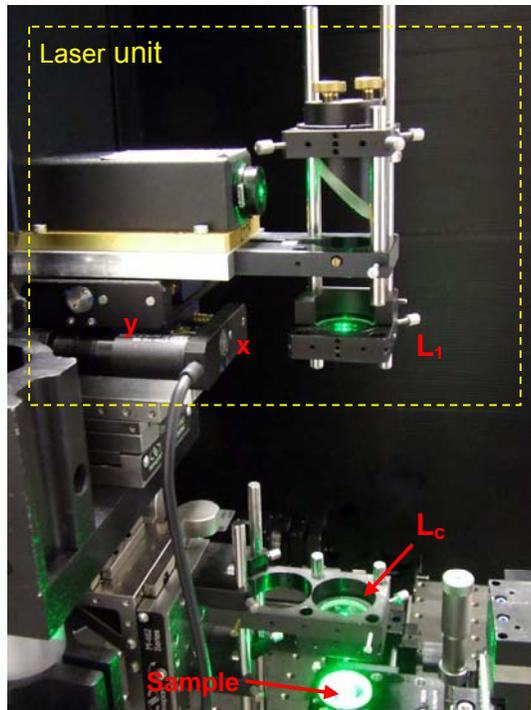
Figure 4.3 photograph showing the illumination arm comprising of the laser unit (yellow box), the condenser lens (L_c), and the sample. Also shown are the stages labelled x and y, providing movement for the laser unit in the x-y plane.

Fine tuning can be carried out on the illumination part. Our usual approach was to set up the illumination arm first and then the imaging arm. Using the high magnification image on the CCD camera this give a more accurate method of to judging the position of the optical elements.

Once the illumination part is set, a simple experiment is carried out to test the scanning of the illumination arm, and the movement of the Talbot pattern. A 2μm strip grating is used to provide the Talbot distribution. The grating is initially positioned so that it surface is imaged onto the CCD camera. It is then shifted by one half of the Talbot distance. At this position, the angle of the illumination is scanned from -3° to +3° in steps of 0.6^o, and at each step the intensity distribution is captured using the camera. This process is repeated two more times, at distances of 1 and 1.5

of the Talbot distance. Figure 4.4 shows the images for the three distances and seven

incident angles. It should be noted that, for ease of alignment, the edge of the grating

was used for the experiment. This gave rise to the edge effect and can be seen clearly

at the tops of the pictures.

$0.5*Z_T$
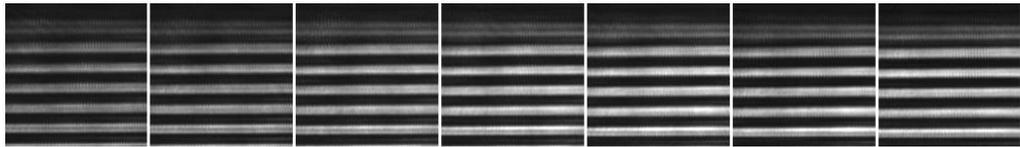
Z_T
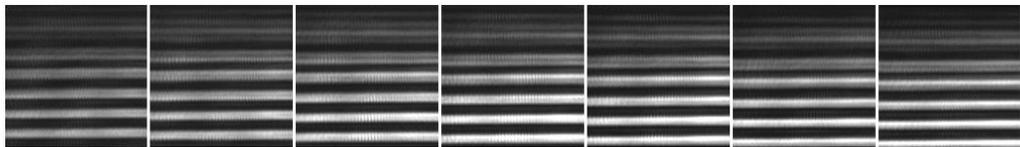
$1.5*Z_T$
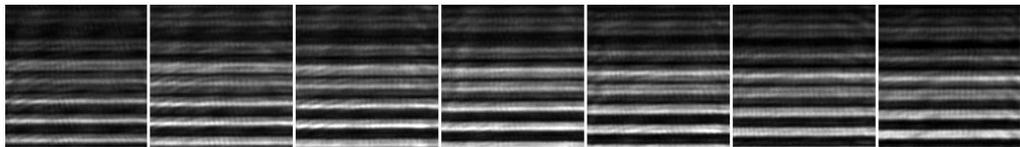
Step (0.6° difference per step)

Figure 4.4 angle scan (0.6 degree each step)

As discussed previously, the shift of the Talbot pattern is proportional to the

distance between the grating and the pattern itself. For quantitative analysis, a

Fourier transform is taken of the images, making sure that the same areas are used

and with the top parts of the pictures excluded. The movement of the pattern is

obtained as the phase of the first harmonics in the Fourier spectrum.
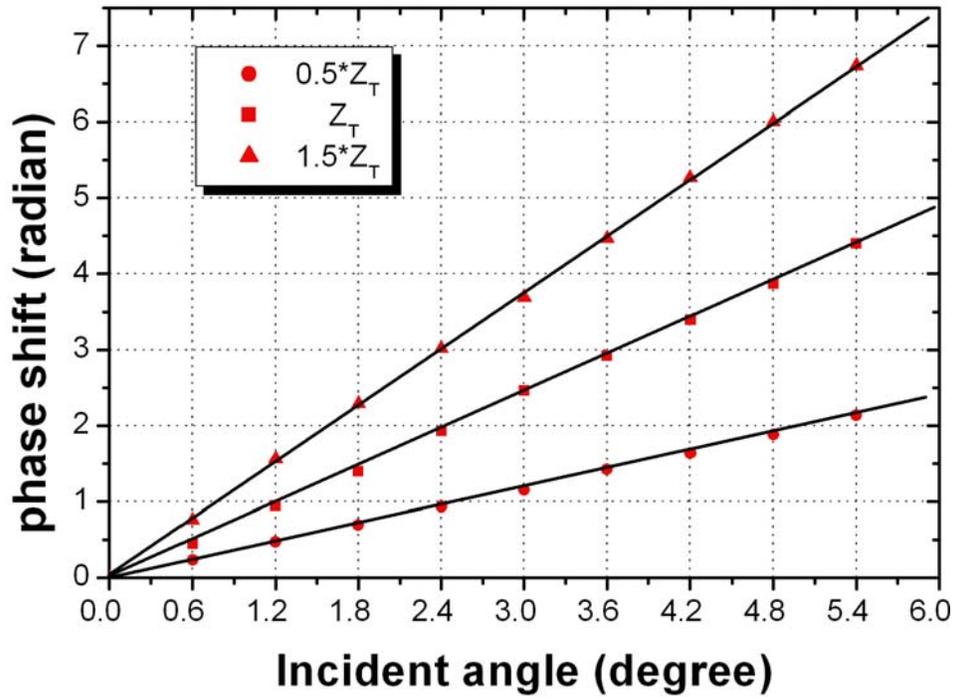
Figure 4.5 The relationship between incident angle and lateral shift

Figure 4.5 shows the plots of the phases of the first harmonics as a function of the incident angle of the incident beam. Three important points to observe:

- All three relationships are linear.

- The shift is proportional to the separation so that the pattern at $1.5Z_T$ moves three times as much as the $0.5Z_T$ one.

- Over an angle scan of $\pm3°$, the phase of the $1.5Z_T$ pattern changes by roughly 6.7radians. Therefore in order to phase step over one grating period, a distance of $1.5Z_T$ would be a suitable choice. If the other two are chosen, a greater scan range will be needed.

113

Choosing the edge of the grating in figure 4.4 is for the sake of showing the edge effect. In any structured illumination experiment we will use the centre area of the grating to avoid the edge effect. The above experimental results demonstrate that a 2μm period with green light (532nm) can produce a diffraction pattern which is movable by changing the incident angle. The angle scan causes a pure lateral shift and can act as phase stepping in the reconstruction algorithm. It is a powerful result to confirm the assumption that Talbot effect works well in this condition (2μm period and <6° incident angle). The grating designs used in this thesis are 3μm and 5μm, and the maximum scan angle is less than ±2.5^o. We can be sure that the diffraction pattern can work as predicted.

4.1.2 Imaging method

In this section, the imaging method is described. As in a conventional microscope, we use an objective lens to collect the light scattered from the object and a tube lens to form an intermediate image. The two lenses are arranged in a telecentric format so that they share a common focal plane. They are followed by another two lenses, again in a telecentric format, so that the final image is formed at the CCD camera. The main reason of adopting this set up is that a variable aperture

can be inserted at the conjugate plan of the back focal plane of the objective. By changing the size of aperture, we can control the spatial bandwidth of the optical system. It means that the effective NA is controlled. The reasons why a controllable NA system is used is that experiments can be performed under different conditions. For example, the image obtained with the full NA can serve as a reference. Furthermore, images obtained with the PGSIM can be compared with those obtained using the conventional wide-field microscope but with increased NA. So a system with a controllable aperture would provide better evidence for comparison.

In addition to the imaging arm, another optical path is inserted in the system. It contains a single lens L_B which images the back focal plane of the objective lens onto a second CCD camera. The purpose of this path is to aid the setting up of the variable aperture, as its image should coincide with that of the back focal plane of the objective lens. The two imaging paths are shown in detail in figure 4.6.
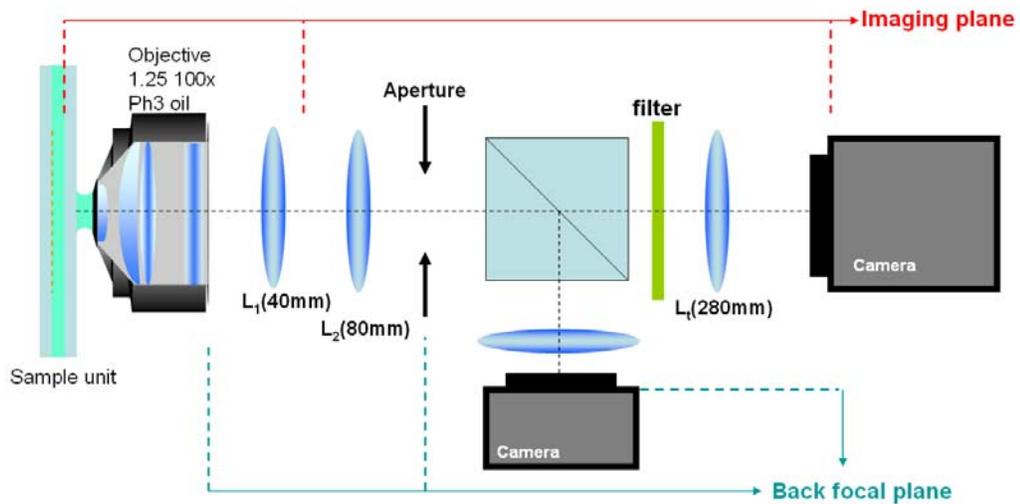
Figure 4.6 set up of imaging arm and back focal plan channel

In order to be able to adjust the variable aperture easily, a magnification of x2 is chosen for the L_1/L_2 lens combination. The focal lengths of the two are therefore $L_1 = 40mm$ and $L_2 = 80mm$. In this conjugate plane, there is an image of the objective back focal plane. An aperture is then put on this location to control the size of the system aperture and hence its NA.

The objective lens used is a Zeiss CP Achromat x100 1.25 oil Phase 3. Note that it is a phase contrast objective with a phase ring at the aperture plane. The use of such an objective is that the phase ring serves as a good reference for the location of the back focal plane, as well as to determine the relationship between the aperture size and the system NA. The CCD camera is an Andor iXON EMCCD, 1004 x 1002 pixels with pixel size 8 x 8 μm^2. The overall magnification of the imaging system is

x80, with the first section providing x23 and the second section x3.5. The effective pixel size at the sample surface is therefore 100 x 100 nm^2. Also included is a band-stop optical filter (Chroma Technology Corp. Z488/532m) that allows for fluorescent operation.

The fluorescent sample used for the experiments has a peak emission wavelength of 550nm, and the system has an NA of 1.25 when the aperture is fully opened. The resolution of the microscope defined by Abbe limit is 220nm. So a x80 magnification, with a 100 x 100 nm^2 digital resolution, would satisfy the sampling condition. The field of view is 100 x 100 μm^2.

The order of alignment is to set the distance between the objective lens and the sample first. Once this is done, the rest of the system is relatively straightforward as they are all afocal arrangement. A Shear-plate is used to test the collimation of the light beam when appropriate. After the lens L_t, the CCD camera is placed at one focal distance away. The sample unit is supported by a piezo-controlled stage for fine focusing of the sample. This is particularly important for high NA operation as the depth of focus of the objective lens is very small. Once the first imaging arm is set, the second arm, and especially the position of the aperture can be aligned with the method described above. Figure 4.7 shows the two arms after alignment.
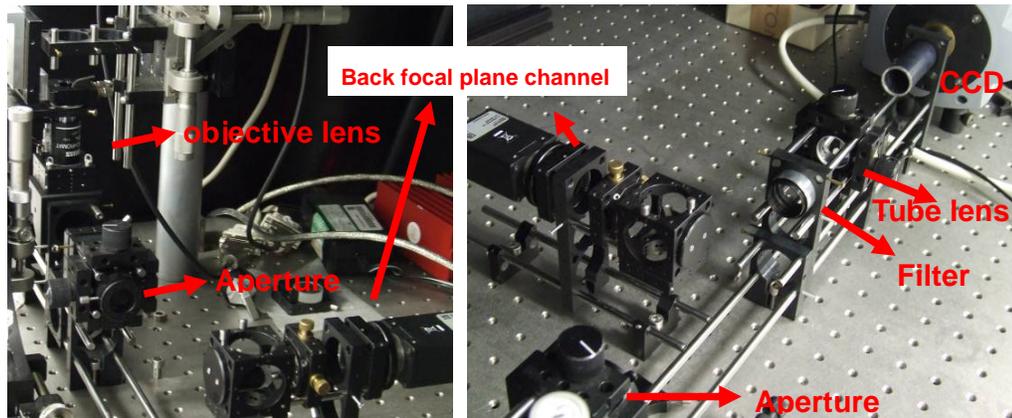
**Figure 4.7** photograph of the imaging arm
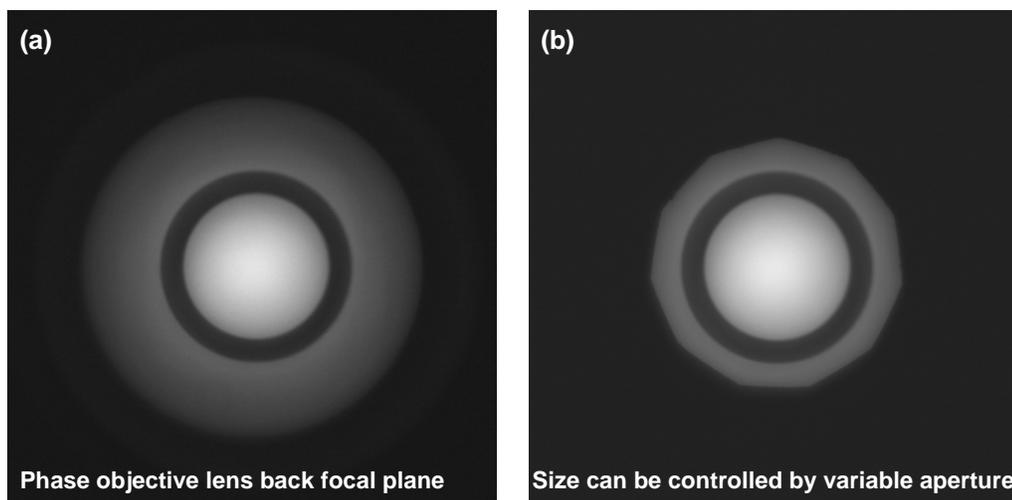
Figure 4.8 back focal plane images (a) full aperture, (b) close the aperture to reduce the size

Figure 4.8 shows the images obtained with the second camera, with the aperture fully (4.8 (a)), and partially opened (4.8 (b)). A green LED is used as the source for this experiment. From the two pictures, it is clear that the phase ring and the aperture are located at two conjugate planes. This phase objective is used in all the PGSIM

experiments. The presence of the phase ring, however, does not affect the system operation as for all the experiments, the system NA is restricted to below 0.4, whereas the inner diameter of the phase ring corresponds to a NA of 0.4.

To sum up, the aim of the imaging arm is set for a fluorescence microscope. A high NA objective lens is used but the system effective NA is controlled using a variable aperture. A simple experiment has been performed to test these two aspects of the microscope. 170nm radius fluorescent beads (excitation/emission: 532/550nm) were used as the sample. Images were captured with the aperture size set at different diameters. In so doing, we could compare the relationship between the system NA and the image size.

Back focal plane

(a) NA$_{eff}$=0.19

(b) NA$_{eff}$=0.29

(c) NA$_{eff}$=0.35

(d) NA$_{eff}$=0.66

(e) NA$_{eff}$=0.93

1μm
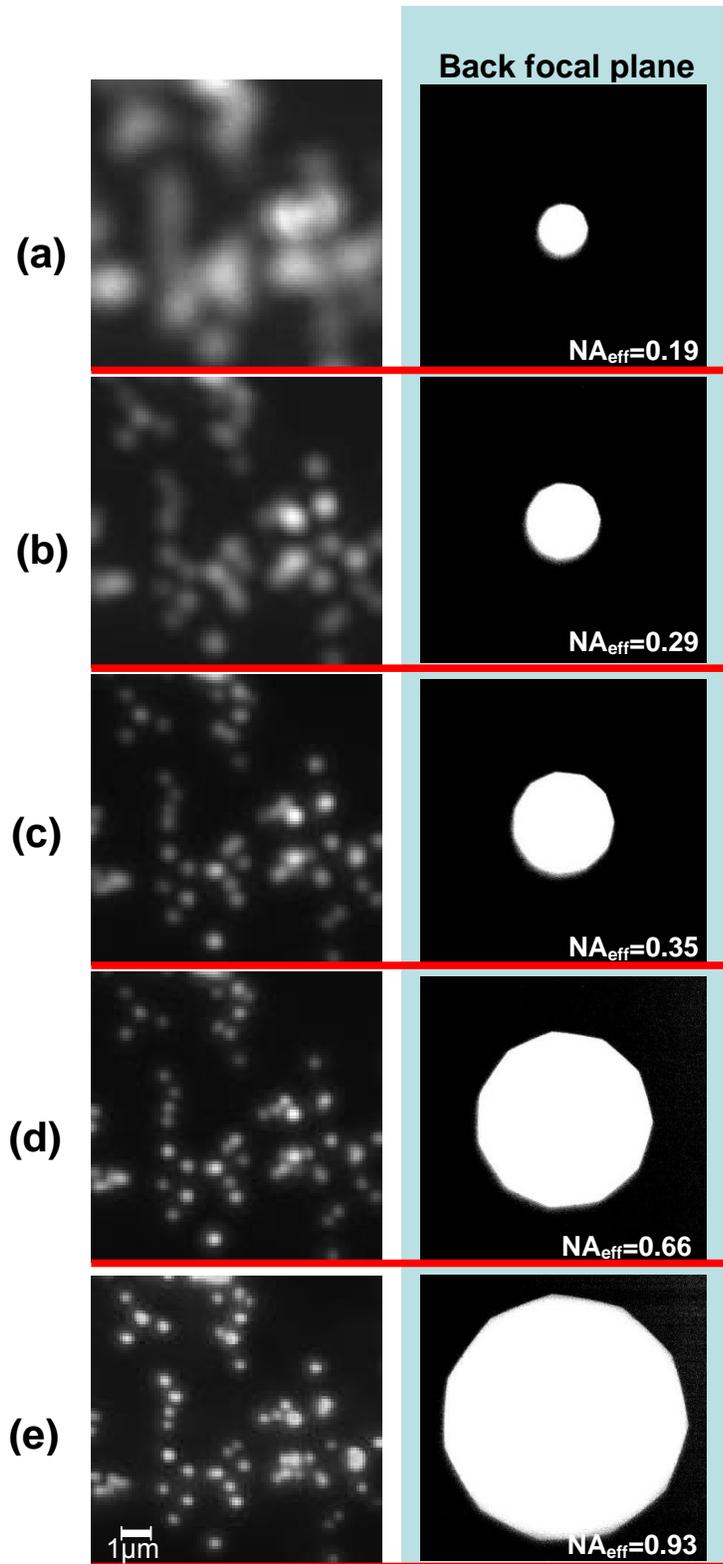
Figure 4.9 fluorescent beads images in different system bandwidth.

Figure 4.9 shows the images obtained at five different aperture settings, and the corresponding system NAs. Figure 4.10 compares the FWHM of the images as a function of the system NA. The solid curve is generated from experimental data (in practice, more than five aperture settings were used). The dashed line is obtained from computer simulation, which is based on a scalar diffraction model with the diameter of the fluorescent bead taken into account. These results demonstrate the validity of the system set up.
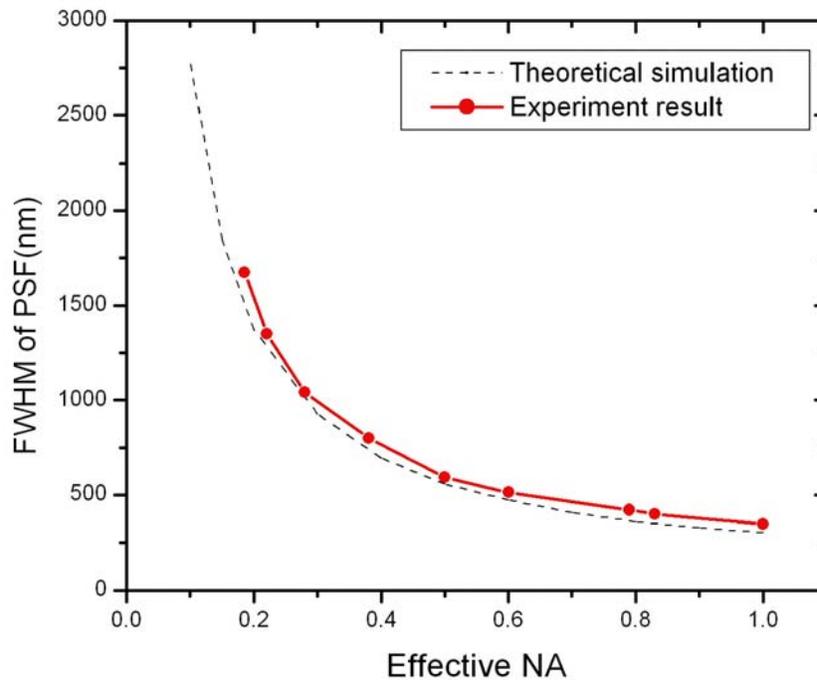
Figure 4.10 Relationship between system NA and the FWHM of PSF.

4.2 Sandwich structure

Sample unit plays a critical role in the system and underpins the principle of the technique. In this section the sample unit will be discussed in detail. The unit can be separated into two parts, namely the optical grating and the thin optical film. The latter is sandwiched between the grating and the sample under test. Once the sample unit is illuminated with a parallel beam, an intensity, or Talbot, pattern will be projected onto the sample surface through the grating. When combined with the illumination arm (Section 4.1.1) and the imaging arm (Section 4.1.2) a complete PGSIM system is established.

In the sections below, the design of the grating pattern will first be discussed. The aim of the grating pattern design is to optimise the spatial frequency components produced by the grating, so as to maximise the extension of the effective bandwidth. Secondly, the fabrication of the thin film between the grating and sample will be discussed. Two methods, one mechanical and the other chemical have been employed and will be described. A comparison between their characteristics will be given. Finally, a 2 D grating is used in the sample unit, and the experimental results obtained will serve to demonstrate the capability of project grating illumination.

4.2.1 Grating design

The key item in the project grating SIM is the sample unit. There are two aims of the grating design:

- The period of the grating and the refractive index of the thin film determine the k-vectors of the illumination pattern, which is the key point behind this technique. Besides this factor, the shape of the grating is also important. For grating with the same period, different on-off ratios change the illumination distributions and the harmonic content. The design of the grating should ensure that the magnitudes of the illumination orders used are as high as possible. Otherwise the signal noise ratio of the reconstructed image will be affected.

- The grating must be a 2 D pattern with frequency components in multiple directions. Since the grating is very close to the sample, it would be difficult to rotate it relative to the sample and a 2D pattern is needed to ensure that any resolution improvement is along both the x and y directions. A square grid grating has frequency components along two directions and a honeycomb-like grating has components along three directions. Both types have been used in the system and results obtained will be presented in the next Chapter.

With reference to the first point, a simulation has been carried out to investigate the effect of the aspect ratio of the grating. Figure 4.12 shows the gratings and their spectra. The five gratings have the same period but different aspect ratios. The spectra are obtained by taking the Fourier transforms of the grating functions. The spectrum amplitude is normalized by the maximum value of (e). As the on-off ratio increases, more light passes through the grating. This causes the DC value of the spectrum to increase. The magnitudes of higher harmonics are also enhanced with increasing on-off ratio. In the extreme case (e), the spectrum is like a comb function and all the harmonics have the same magnitude. For our system we have selected a ratio of 80%-20% (d), which is a good compromise between the uniformity of the grating components, the relatively high absolute values of the magnitudes of the different orders, and the ease of manufacturing.
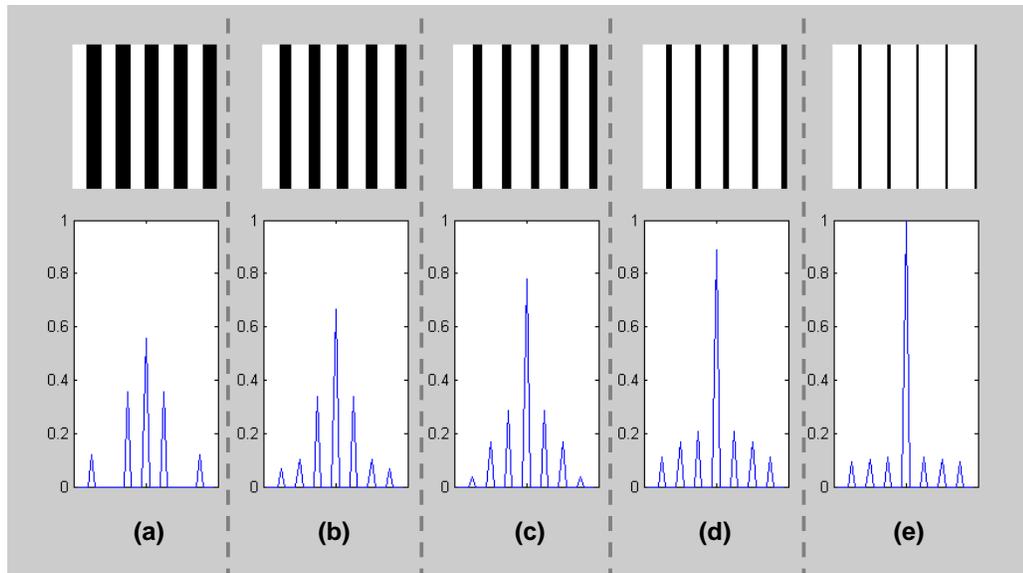
Figure 4.12 Gratings of the same period but different aspect ratios. (a)50%-50% (b)60%-40% (c)70%-30% (d)80%-20% (e)90%-10%

As have been mentioned above, we have designed gratings with square and triangular shapes. Figure 4.13 shows the two patterns and the respective frequency components. As can been seen, the latter are uniformly distributed as expected.

Rectangle grating

Triangle grating

Frequency domain

Frequency domain
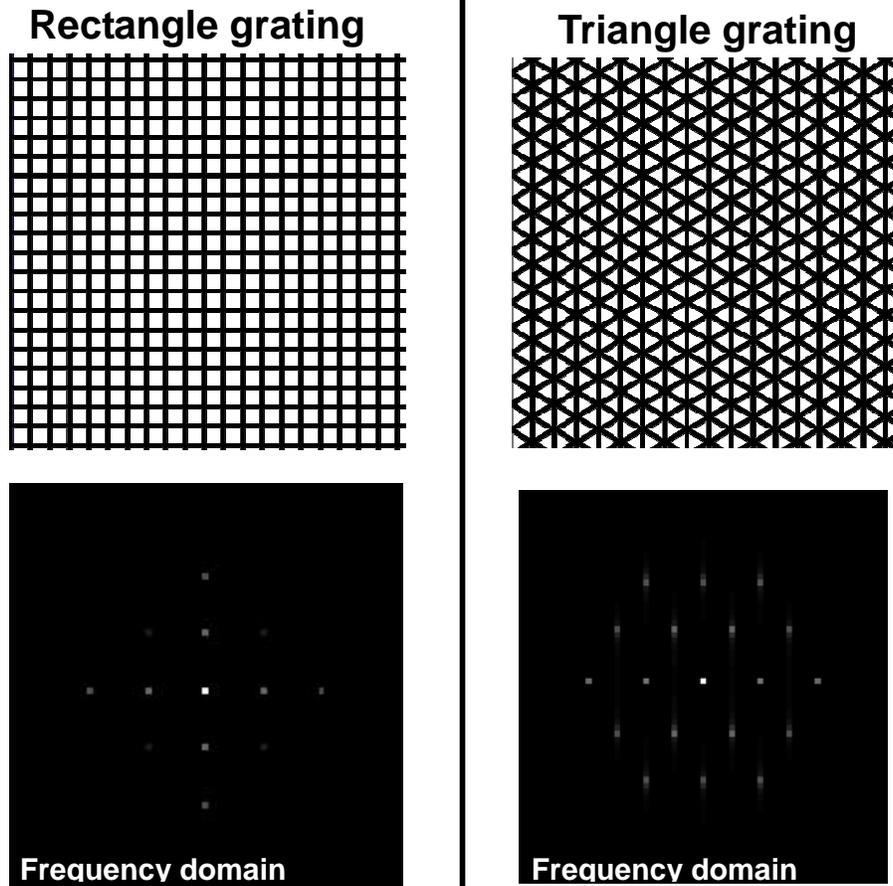
Figure 4.13 two kinds of grating design

After the pattern design, the gratings were fabricated by a Swiss company, EULITHA using e-beam lithography. The specifications of the gratings are as follows:

Substrate:	0.22mm BK7 coverglass, 22mm diameter
Metal layer:	60nm Chromium
Period of gratings:	for square grating, 3μm edge to edge
	for triangular grating, heights of triangles = 3μm
Aspect ratio:	80% - 20%, i.e. 2.4μm gap and 0.6μm chromium
Total pattern area:	400μm x 400μm

A square grating of 5μm period and 80% - 20% aspect ratio has also been made

for test purposes. A schematic of the grating is shown in figure 4.14.
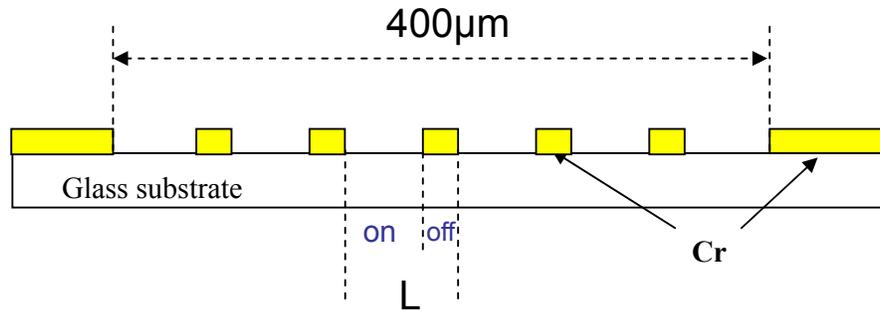
Figure 4.14 schematic of Grating

4.2.2 Controlling the gap between the sample and grating

The PGSIM takes advantage of the fine grating to create a high spatial frequency illumination at the sample. As discussed in Section 3.1.1, appropriate gap thickness between the grating and the sample is important, and will ensure sufficiently high magnitudes of the illumination orders for proper reconstruction of the image. In this section, details of the sample unit, and in particular, the appropriate gap value will be discussed. Diffraction patterns obtained experimentally will be compared to those obtained from simulation, showing excellent matching of the two.

There are several ways to construct the sample unit, each with their relative merits. The first method makes use of thin plastic shims as spacers between the grating and the sample substrate. The space created inside is then filled with

microscope immersion oil. This method is relatively easy but the end result lacks robustness and precision. Although plastic shims came with a wide range of thicknesses (from 12.5μm to 1mm thick in steps of 12.5μm), the gap is hard to control and it is also difficult to prevent bubbles forming in the oil. In practice, it was found that error of up to 20μm in the separation was common.

A different mechanical set up was then tried to overcome this problem. This method involves using a piezo nanocube (see Appendix B) to control the position of the grating relative to the sample. The cube has a movement of 100 μm in all three directions, and a nanometer resolution. It is fully computer controlled and is used to adjust the separation between the two substrates.
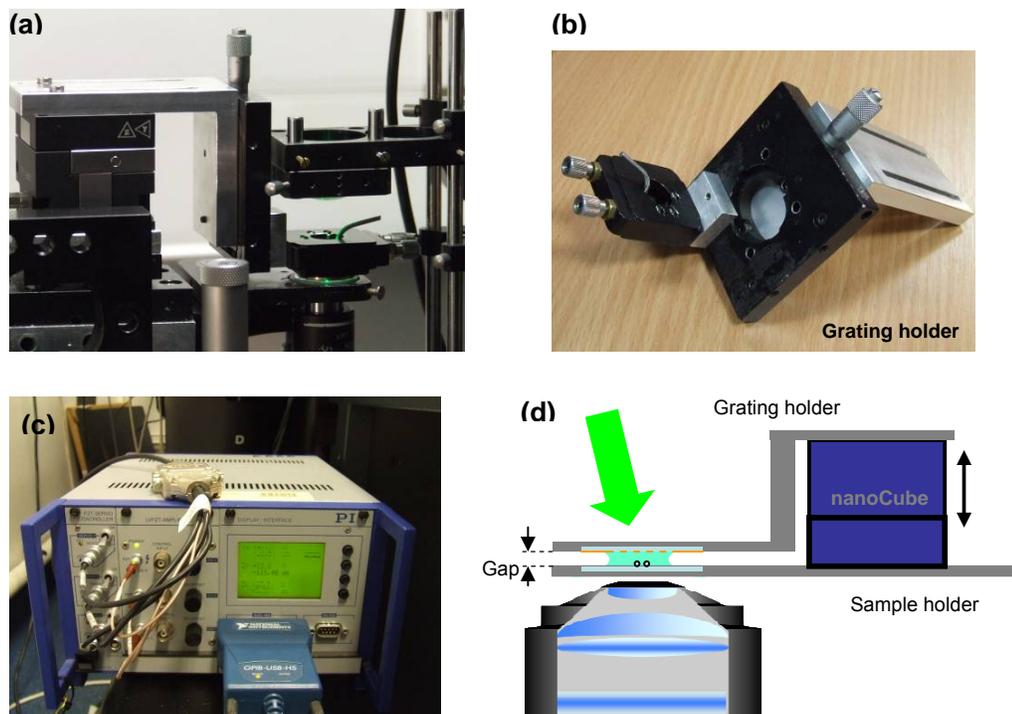
Figure 4.15 Sample holder using a piezo nanocube. (a) the whole sample unit. (b)

grating holder consisting of a coarse z positioner and a tip-tilt stage for the grating. This unit is mounted on the nanocube. (c) stage controller. (d) sample unit configuration.

Figure 4.15 shows the set up of the sample holder and the nanocube. The grating holder (Figure 4.15 (b)) comprises of a grating mount which has a x-y tip-tilt adjustment, and a coarse micrometer controlled translation stage. This grating holder is mounted on the nanocube as shown in figure 4.15 (a). This setup provides a coarse vertical adjustment, a fine x-y-z adjustment, and a fine x-y tip-tilt adjustment, and is sufficient to set the sample holder to the required specifications.

Assuming that the two substrates are parallel (the procedure will be described later this section), the setting of their separation will first be discussed. In reality, the separation is not set to any particular value. Instead the grating substrate (upper part in figure 4.15 (d)) is lowered towards the sample, with the objective lens focused at the sample surface. The intensity pattern projected onto the sample is monitored with the imaging arm of the system. The position of the grating is fixed once the observed pattern is considered appropriate. The actual separation of the two surfaces can be measured experimentally and the procedure will be described later.

We will now describe the method used to set the grating parallel to the sample surface. Both surfaces are 22mm in diameter (size of cover glass), and a small angular misalignment can result in a gap error in the range of hundreds of

micrometers. For example, a 1° error in the parallelism of the two surfaces will produce a difference in the gap value of 192μm between the centre and the edge of the substrates. Fine tuning of the parallelism of the two surfaces is therefore necessary.

Grating surface
Sample surface
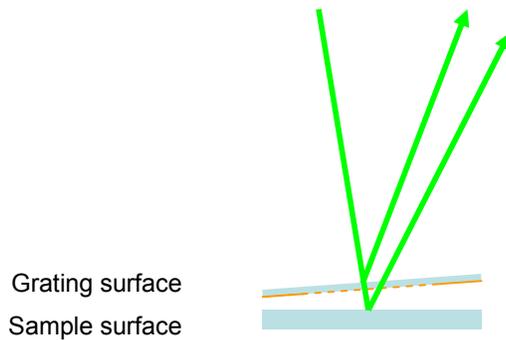
Figure 4.16 Instruction sketch

Figure 4.16 shows the method used to make two surface parallel, which consists of the following steps:

1. Assuming that the sample surface has already been set perpendicular to the optical axis, it would be used as the reference for setting the grating surface.

2. A laser beam is used to illuminate the sample surface at near normal incident. The surface reflection is projected at a far distance and its location is marked.

3. The grating holder is then attached to the nanocube and is then lowered towards the sample.

130

4. Fine tune the tilt stage until the second reflection coincides with the first marker. Provided the distance in 2) is sufficiently large, the two surfaces are considered to be parallel.

The distance from the sample surface to the marker is around 5 meters, and assuming the position of the reflected beam could be judged to within 1mm, the parallelism of the two surfaces can be adjusted to better than 0.01°. This value is sufficiently accurate for our application.

This method is controllable because of the use of the nanocube. As described above the gap was chosen based on the intensity pattern projected on the sample. To measure the value of this gap retrospectively, we scanned the illumination beam over a small angle and monitor the lateral shift of the pattern. Using the relationship described in Section 4.1.1, the separation between the two surfaces can be calculated. In practice, we have found that such a procedure could be used to set the separation down to about 50μm. Beyond this, more precise mechanical adjustment, especially the tip-tilt stage, would be needed.

Figures 4.17 and 4.18 show the intensity patterns obtained at the sample surface, as the gap between the two surfaces is changed. Figure 4.17 is for a 5μm square grating whereas 4.18 a 3μm triangular grating. Also shown are patterns obtained from computer simulations.

| Rectangle grating(period 5μm)		
Z	simulation	measurement
$n*Z_T$		
$n*Z_T+0.12\ Z_T$		
$n*Z_T+0.25\ Z_T$		
$n*Z_T+0.43\ Z_T$		
$n*Z_T+0.5\ Z_T$		
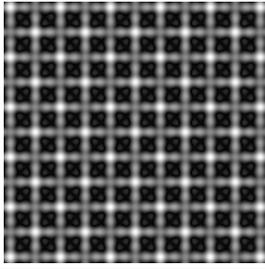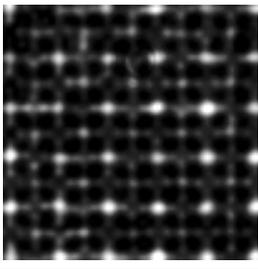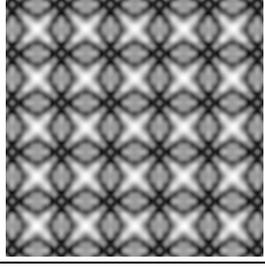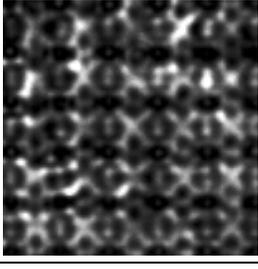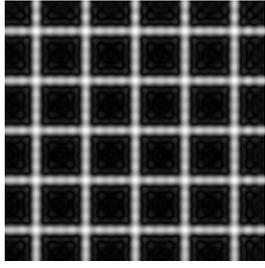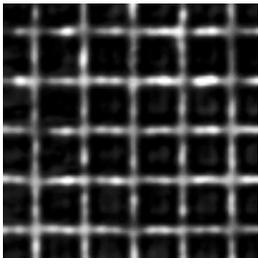
Figure 4.17 Square grid grating: simulations and experimental results

| Triangle grating(period 3μm)		
Z	simulation	measurement
$n*Z_T$		
$n*Z_T+0.1\ Z_T$		
$n*Z_T+0.35\ Z_T$		
$n*Z_T+0.47\ Z_T$		
$n*Z_T+0.59\ Z_T$		
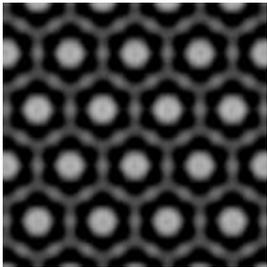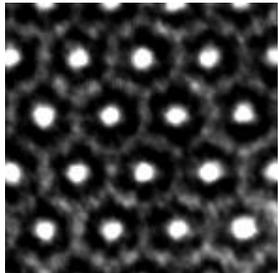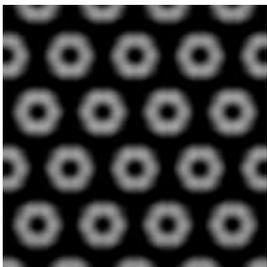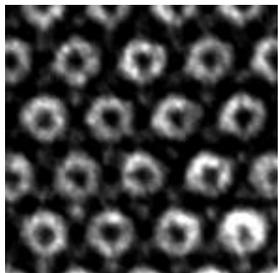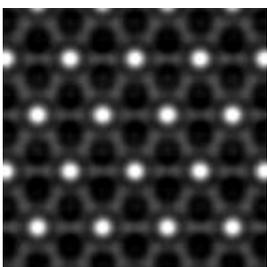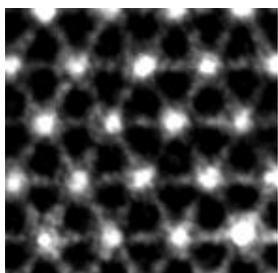
Figure 4.18 triangle grating diffraction pattern comparisons

4.2.3 General discussion of sample holder requirements

The above results show the diffraction patterns at different separations from the grating. The patterns match the simulated results remarkably well, demonstrating the careful construction of the sample unit and the control of the gap separation.

As discussed in section 3.1.1, the intensity pattern repeats itself at regular intervals. For general application, the Talbot image is the choice of illumination as it provides high illumination orders. Combining the sample unit, the illumination arm, and the imaging arm, a complete proximity projection grating illumination microscope system is established.

With the sample unit described, microscope immersion oil was used to fill the gap between the two substrates. Using oil is relatively simple and serves to demonstrate the principle of the technique. As discussed in section 3.2, the system bandwidth can be extended further if a higher refraction index material is used. For example the use of solid thin film will provide a more robust and more precise structure. A suitable construction of the sample unit would be to deposit TiO_2 onto the grating. TiO_2 has a refractive index of around 2.5 in the visible spectrum and can therefore extend the bandwidth of the system much further. The table below summarise the advantages and disadvantages of the different approaches.

	Infrastructure requirement	Physical range	error	Flexibility to change the gap	capability
Plastic shim as spacer	easy	>50μm	≈20μm	Low(change different thickness)	Oil immersion
Mechanical grating holder	common	>50μm	≈1nm	high	Oil immersion
Solid thin film coating	hard	<5μm	≈1nm	No(fixed after coating)	Solid immersion

Table 4.1 Sample unit of different approach

4.3 Layout of microscope and specifications

Up to now, the illumination arm, imaging method and sample unit have been explained. These three parts constitute the proximity projection grating SIM. Figure 4.19 is the photograph of the system set up, with the key components marked by numbers. The corresponding schematic of the system was shown in Figure 4.1.
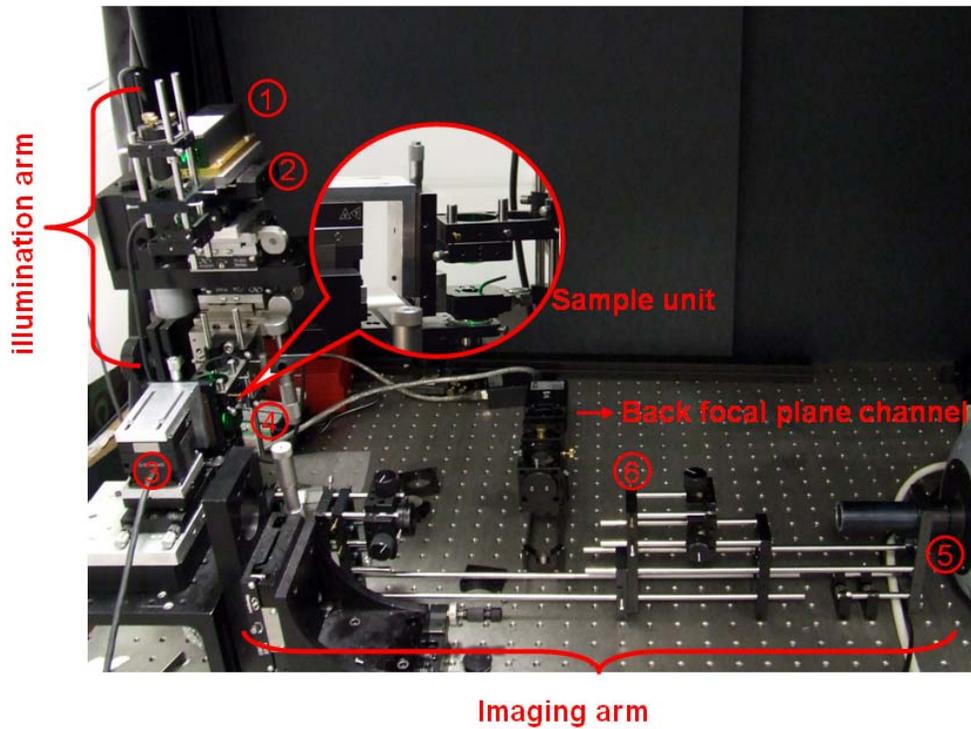
Figure 4.19 photography of the proximity projection grating SIM.

1. Nd-YAG laser(λ=532nm, P=50mW).

2. XY stage(travel range: 25mm,resolution: 0.1 μm).

3. nanocube(travel range: 100μm/axis, resolution: 0.2nm).

4. objective lens(NA=1.25).

5 CCD camera(1004×1002 pixels).

6 emission filter(block the laser 532nm and is transmitted in 550nm).

The second imaging arm is used to monitor the system back focal plan and it can move in and out for different purpose.

More details of the components are listed in Appendix B.

4.4 Summary

The optical system implementation has been shown in this chapter. All the key design considerations including components used, optical alignment and positioning have been discussed at length. The system consists of three parts: illumination arm, sample holder, and imaging arm.

The illumination arm produces a parallel beam with a controllable incident angle. A 2µm grating is used to show the lateral shift of the projected pattern at the sample surface. The relationships between the shift, the value of the gap and angle of the incident laser beam have been demonstrated experimentally (figure 4.5). In doing so, we have also shown that the set up provides sufficient lateral shift of the pattern for phase stepping purpose.

In the section of imaging arm, a controllable aperture is put in the back focal plan of the system to create a microscope with variable effective NA. A set of experiments is taken to compare the imaging size of fluorescent beads and the system effective NA (figure 4.9). In addition, another imaging arm is built to monitor the system back focal plane.

The sample holder includes two parts: grating design and the gap control. The aim of the grating design is to obtain an illumination pattern with high k-vector and

fully fill the frequency domain in different directions. Then the sample holder is

formed by the nanocube which can control the gap accurately. A comparison of

experimental and simulated diffraction patterns ts is shown (figure 4.17 and 4.18),

and demonstrates how the illumination pattern can be controlled by changing the

gap.

Chapter 5 Experimental results

In the preceding chapter, the optical system and its calibration have been explained. A series of experiments have been carried out to illustrate various aspects of the system. In this chapter, a low NA system will be used to demonstrate the principle of the technique.

The sample preparation and the collection of the phase shifted images will be explained first. Then the experimental results obtained using the 3μm square grating will be shown, demonstrating a resolution improvement by more than a factor of 2 in two dimensions. This will be followed by results obtained with the 3μm triangle grating, showing resolution improvement in three directions. In addition, we will compare the experimental results with those obtained from simulation, showing a high degree of agreement between the two. Comparison between the square and triangle gratings will be given.

5.1 Sample preparation and image acquisition

In all of the experiments, 170nm fluorescent beads (FluoSphere carboxylate-modified microsphere, Crimson fluorescent (530/550) Invitrogen) are

used as test sample. These beads are diluted with deionised water and the

concentration is set so as to avoid particle aggregation. From experience 1% particle

concentration is found to be the most appropriate choice. With this concentration, the

fluorescent beads would tend to spread out, with occasional small groupings, thus

providing a good target for the examination of the performance of the system. The

diluted bead solution is pipetted onto a cover-glass which is then placed on a 50°C

hot plate for 30 minutes to dry.
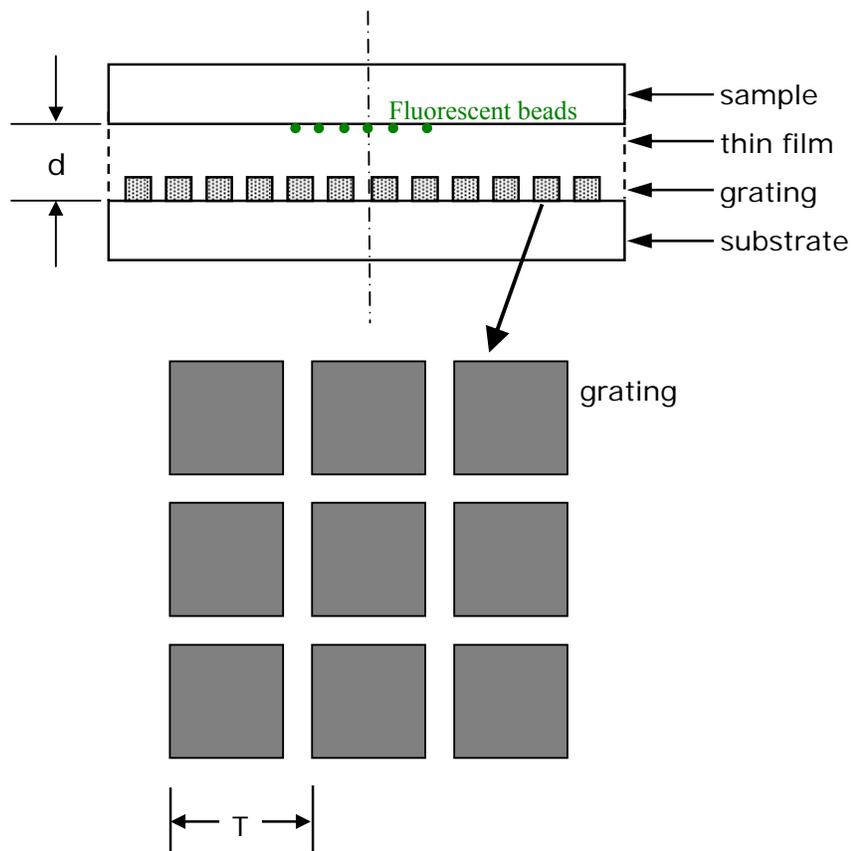
Figure 5.1   Sample holder showing the fluorescent beads and the grating.

Figure 5.1 shows the sandwich structure including the fluorescent bead sample, the optical thin film, and the grating. Together they form the sample unit. In the first experiment shown below, the 3μm square grating is used. Microscope immersion oil (Zeiss n = 1.518) is used as the thin film and plastic shim is employed as spacer to control the oil thickness. Once the sample holder is fixed, the thickness of the film is measured by scanning the input beam angularly and monitoring the shifted of the diffracted intensity pattern, as described in section 4.4.1. For the present case, the film thickness is measured to be 70μm.

In our experiments, we would generate N x N phase shifted images, as shown in figure 5.2. Normally they are spaced equally so that along each row and column, the images will undergo a total phase shift of 2π. In theory, only N images along the x-direction, and another N along y are required. The additional images serve to improve the SNR of the reconstruction as well as reducing the effects of speckle noise. Another step before the reconstruction is to remove background noise. This is accomplished by creating a background image, obtained with the laser source switched off. Each of the phase shifted image is then subtracted by the background.
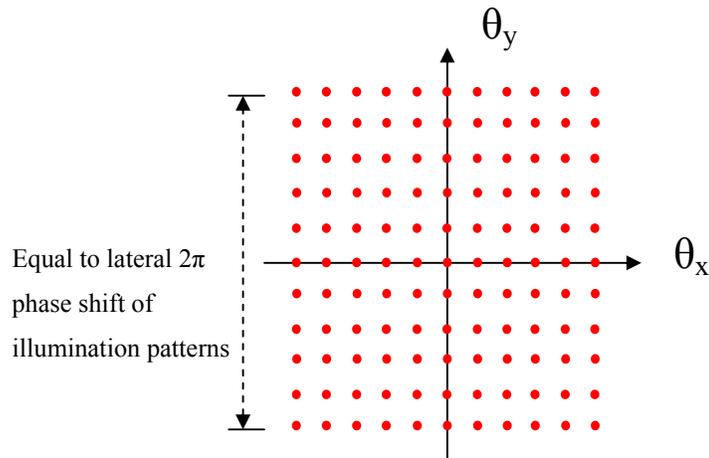
Figure 5.2 Scan angles of all steps. Each point indicates the scan angle of x and y direction. The separation is the same in both directions, and each row or column can be sum and obtain a pure 1 dimension structured grating with low noise. Total scan angle in each direction is 2π to avoid ill condition in the reconstruction process (See section 3.1.4).

For all the experiments shown in this chapter, three sets of results are shown. They are the fluorescent bead images obtained using a low NA setup, the reconstructed images, based on the same low NA setup, but with the application of the PGSIM technique, and images obtained with a high NA setup. These three sets of results provide a consistent and reliable comparison of the proposed technique. To quantify the resolution improvement, we measure the FWHM of the bead images for all three settings. Furthermore, the resolution improvement in different directions will also be considered.

5.2 Experimental results

In this section, the results obtained with the 3μm square grating will be shown first, demonstrating the resolution improvement in the horizontal and vertical directions. Results obtained from the 3μm triangle grating results will then be presented, showing clearly the resolution improved in three directions.

5.2.1 3μm square grating

Figure 5.3(a) shows the image of the grating at the sample surface (top surface of the thin oil film), taken with the band-stop optical filter removed. Figure 5.3(b) shows the intensity distribution at the back focal plane of the objective lens, taken with the second CCD camera as shown in section 4.1.2. The dc and the eight Fourier components (components up to the second order along the x and y directions) are clear in the figure. In the reconstruction performed, we used only the dc, ±1 and ±2 of the Fourier components.

(a) illumination　　　　**(b) Back focal plane**
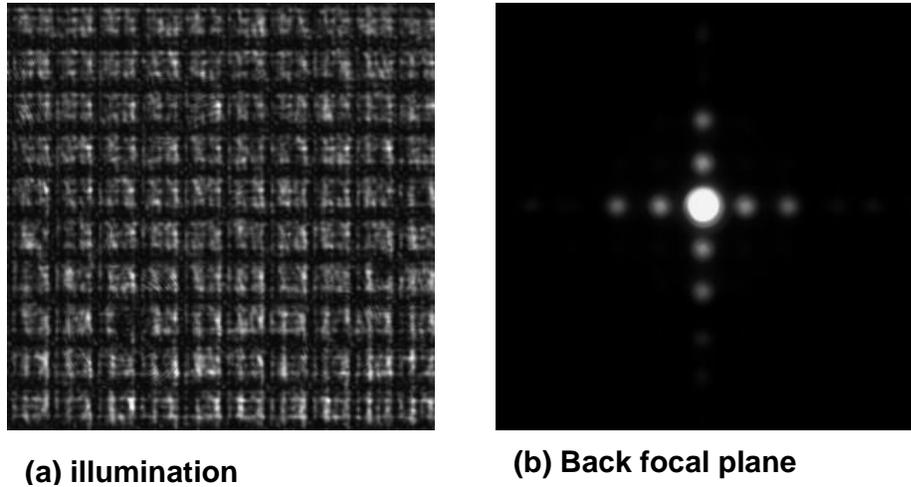
Figure 5.3 (a) Intensity pattern of the grating projected onto the sample plane, and (b) the back focal plane channel

(a)

(b)
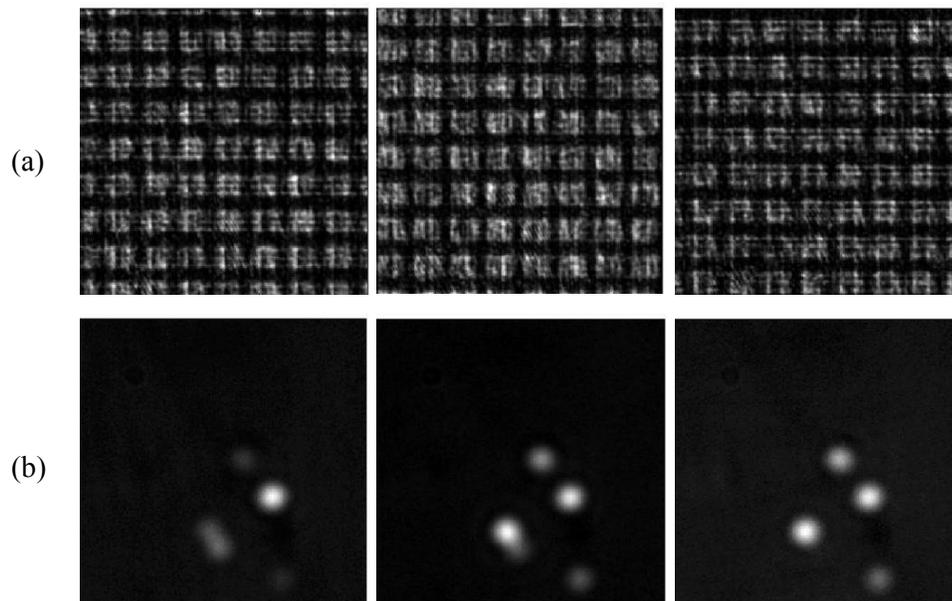
Figure 5.4 (a) Illumination patterns for different phase step, and (b) the raw images.

Figure 5.4(a) shows the grating images acquired in three phase steps. 5.4(b) shows the resulting images of the samples, and the effects of the changes in the

illumination patterns can be clearly seen.

The number of phase shifted images required is determined by the number of Fourier components used in the reconstruction. If M is the number of the Fourier components used in each direction (with the positive and negative orders counting as one), excluding the dc term, then the minimum number of phase shifted images needed is

$$N = 2M + 1 \qquad\qquad (5.1)$$

As we use M = 2 in the reconstruction, the minimum number of phase shifted images required is therefore 5. In practice, we usually use N = 10.
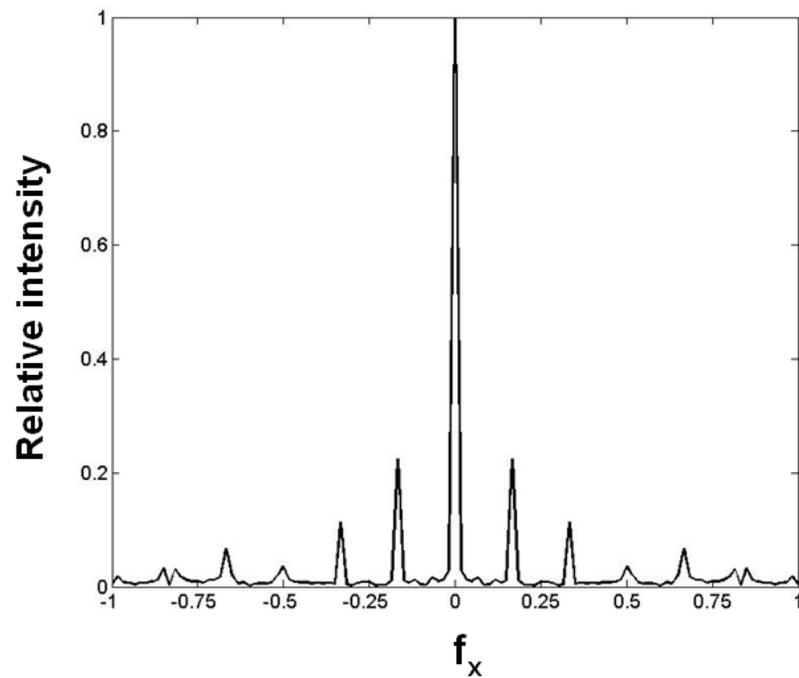
Figure 5.5 Fourier components of the intensity pattern

Figure 5.5 shows the magnitude of the Fourier transform of figure 5.3(a), along the x-direction. The relative magnitudes of the Fourier components are determined by the aspect ratio of the grating, and the optical thickness of the thin film used, as discussed in the last chapter.

The locations of the harmonics are related to the optical wavelength and grating period, and are given by the grating equation:

$$L\sin(\theta_m) = m\frac{\lambda}{n} \qquad (5.2)$$

where L is the grating period, m is the order, and n is the refractive index of the thin film. We define an effective NA to represent the locations of the harmonics as:

$$NA_m = n\sin(\theta_m) = m\frac{\lambda}{L} \qquad (5.3)$$

For the 3µm period grating and wavelength of 532nm, the fundamental is therefore equivalent to an illumination NA_m of 0.177, and the second harmonic an NA_m of 0.354, both can be seen in figure 5.5. In order to illustrate the resolution improvement, we choose the NA of the original system to be 0.17, and the diameter of the variable aperture is set to give an imaging NA equal to 0.17. Based on this

146

setting, the effective NAs for using the zero order, zero & ±1 orders, and zero & ±1 & ±2 orders are respectively 0.17, 0.26 and 0.35.

Figure 5.6 shows the results obtained with the square grating. 5.6(a) is the image obtained using the zero illumination order only, and is thus equivalent to that from a 0.17 NA conventional microscope. 5.6(b) is the reconstructed image using the zero, ±1 and ±2 orders. 5.6(c) is similar to 5.6(a) but with the variable aperture fully opened, giving an imaging NA of 1.25. The last image serves as a reference. The improvement in the lateral resolution provided by the technique is clear. It is also worth noting the successful recovery of the two features at the lower left side of the picture, where one is much more intense than the other, indicating the robustness of the reconstruction process.
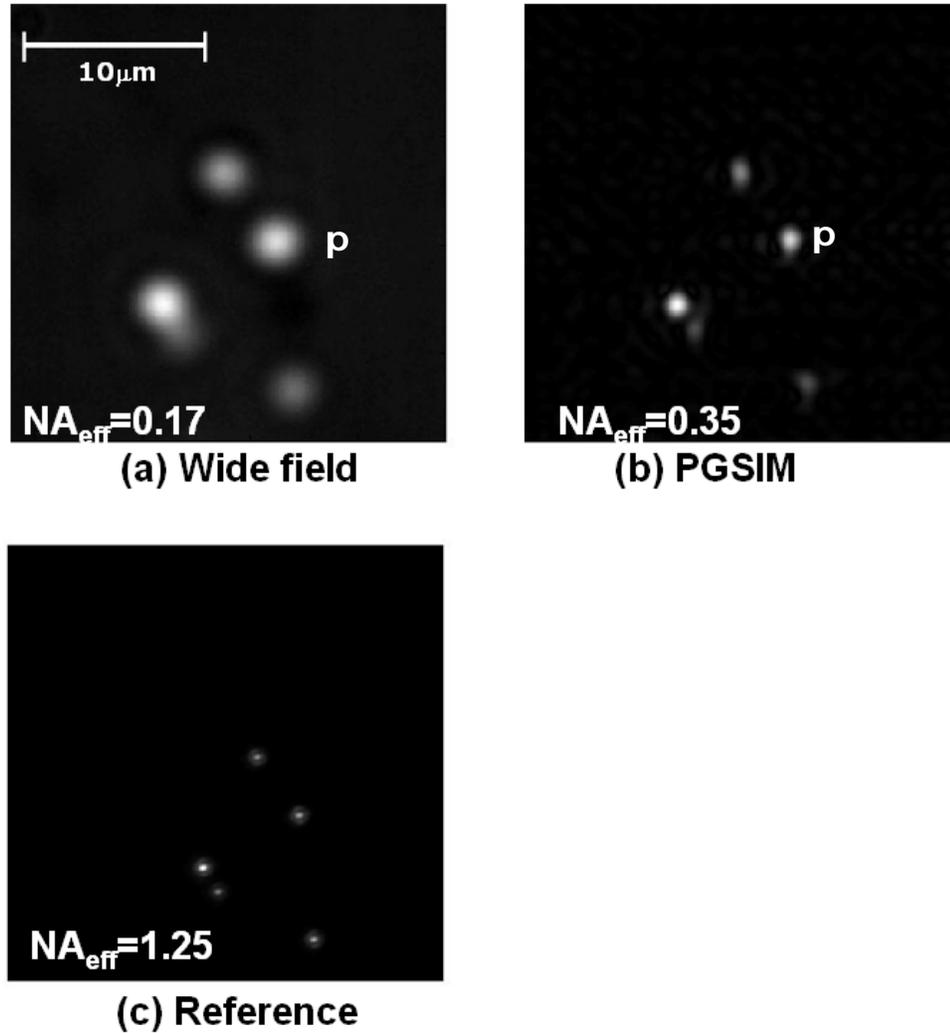
Figure 5.6 (a) Image of fluorescent beads using reduced aperture (NA = 0.17), (b) reconstructed image using the zero, ±1 & ±2 orders, Fourier components of the intensity pattern

Figure 5.7 shows the intensity profiles across the particle labelled 'p' in figure

5.6, with the curve labelled 1 extract from 5.6(a), and the one labelled 3 from 5.6(b).

Curve 2 is similar to 3 except that it is reconstructed using the zero and the ±1 orders

only. It therefore has a smaller effective NA than curve 3. The FWHMs of the three

are measured to be 1.7 μm, 1.1 μm and 0.85 μm respectively.
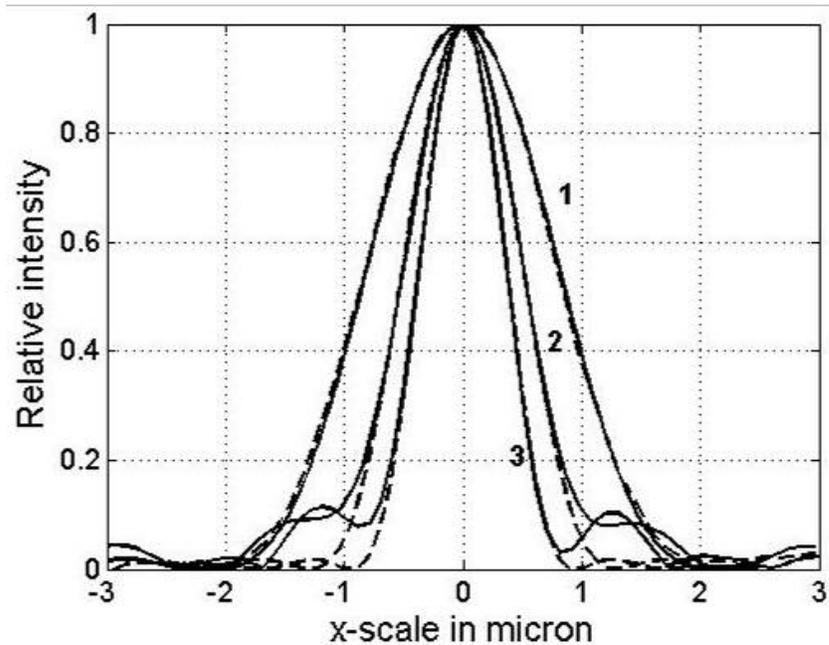
Figure 5.7 Intensity profiles of the fluorescent bead labelled P in figure 5.4(b). Profile 1: obtained using the reduced NA of 0.17; Profile 2: reconstructed using the zero and ±1 orders; and Profile 3: reconstructed using the zero, ±1 & ±2 orders. Dashed lines are simulated profiles using NA of 0.17, 0.26 and 0.35 respectively for the three profiles.

Three simulated profiles (in dashed lines) are also shown in the figure. These simulated profiles are obtained using a scalar diffraction model, assuming that the system has a Chinese hat transfer function. To produce the fits, system NAs of 0.17, 0.26 and 0.35 have been used.

The ratios of the three NAs are 1 : 1.53 : 2.06. Therefore, using the present set up and diffracted orders up to the second grating order, it can be concluded that a resolution improvement of 2.06 times has been achieved. Two points are worth

noting here: 1) curves 2 & 3 have distinctly larger sidelobes compared to curve 1, which are mainly due to the shapes of the equivalent transfer functions for the two. They can be suppressed relatively easily and will be discussed in the next section; 2) we have only used up to the second diffraction order in the reconstruction algorithm. In comparison the magnitude of the third order is small relative to the first and second. Its inclusion will inevitably lead to noisy reconstruction. However, as discussed in section 4.2.1, the relative magnitudes of the illumination orders could be modified by changing the aspect ratio of the grating structure, this makes the use of the higher orders feasible.

A second set of result is shown in figure 5.8, with the same system parameters as in figure 5.6. There are two particles (in region labelled 'P') that are close to each other, and provide a good demonstration of the resolution improvement. The intensity profiles across the two particles are shown in 5.8(d).
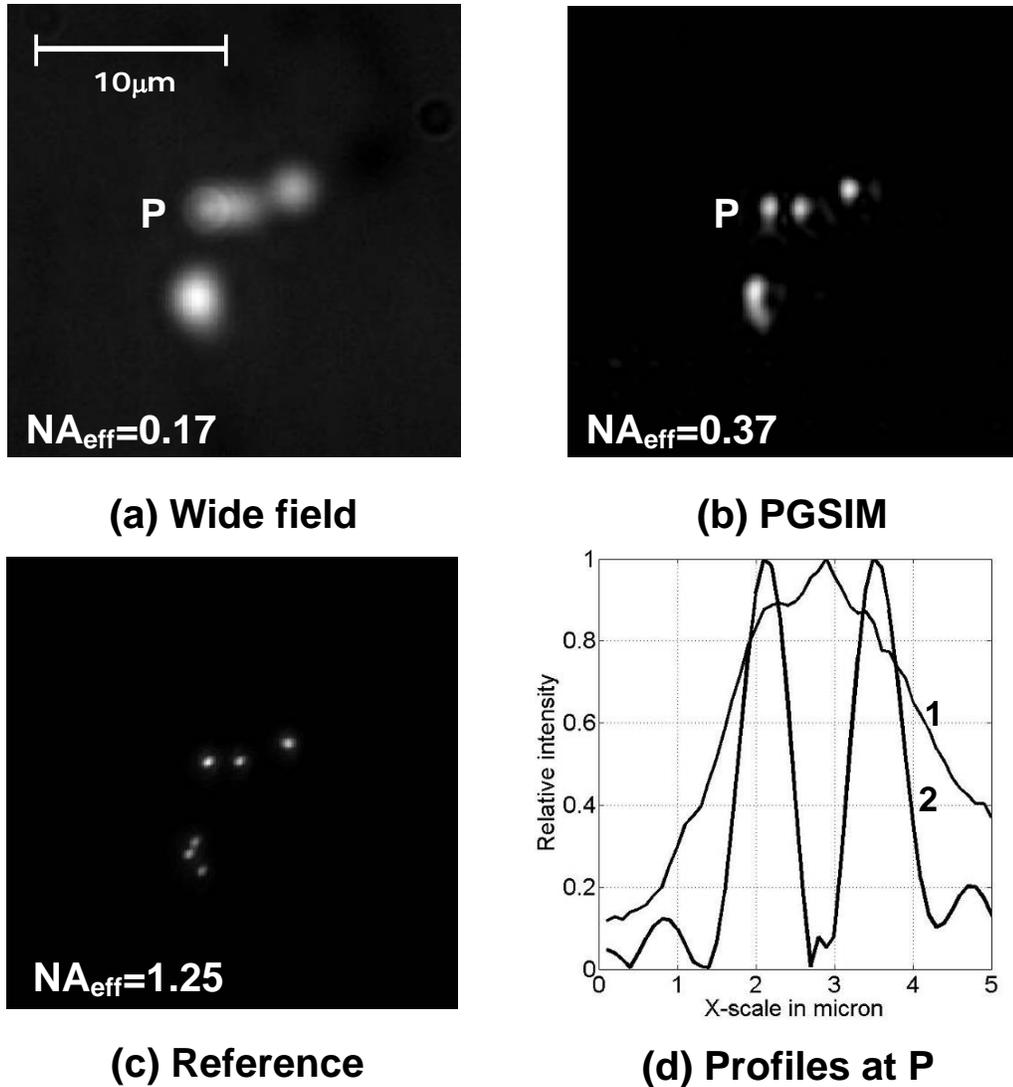
Figure 5.8 (a) Image of fluorescent beads using reduced aperture (NA = 0.17), (b) reconstructed image using the zero, ±1 & ±2 orders, Fourier components of the intensity pattern, (c) image with full open aperture as reference(NA=1.25), (d) horizontal intensity profiles of the fluorescent beads labelled P in figure 5.6(a) and 5.6(b). Profile 1: unresolved particles extracted from (a); Profile 2: resolved particles extracted from (b).

Table 5.1 summarises the 3μm results. The effective NAs are obtained from the system settings, depending on the grating period and the diameter of the variable

aperture. The experimental FWHMs are obtained taking the average of the isolated particles in figures 5.6 and 5.8. The values for both the vertical and horizontal directions have been used. The final column is obtained using the scalar diffraction model, applied to fluorescent beads of 170nm in diameter, for the stated effective NAs.   The measured FWHMs are slightly larger than those from simulation, but are well within the experimental tolerance.

		PGSIM experiment FWHM	Simulation (Chinese hat MTF) FWHM
DC	NAeff = 0.17	1700±50nm	1700nm
DC, ±1	NAeff = 0.26	1100±50nm	1056nm
DC, ±1, ±2	NAeff = 0.35	850±50nm	800nm

Table 5.1 FWHM of PSF

Using the above settings, a resolution improvement of 2.06 times has been achieved. However, the 11% sidelobes make the PSF appear artificial. The reason behind the large sidelobe is that the effective transfer function is not circularly symmetrical. The frequency components provided by the square grating are concentrated around the vertical and horizontal axes as illustrated in figure 5.9, and the resolution improvement is primarily along these two directions. The lack of signals beyond the circles in the frequency domain contributes to the 11% sidelobes.
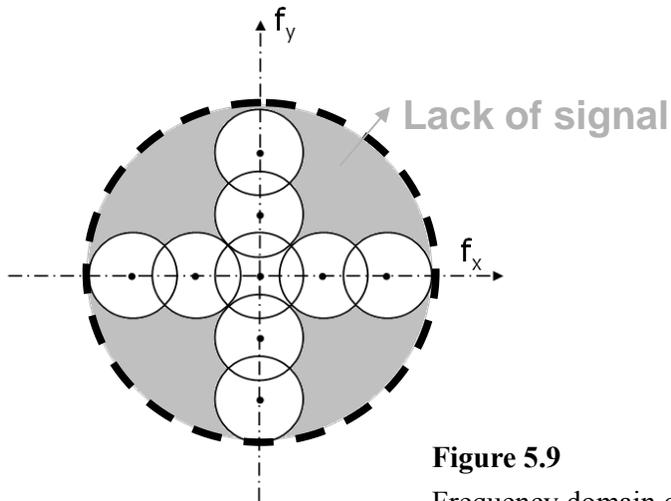
Figure 5.9
Frequency domain distribution after reconstruction.

In order to reduce the sidelobes and improve the image quality, a triangle grating is used instead of the square grating.

5.2.2 3μm triangle grating

With the triangle grating, the period is kept at 3μm. In addition, the gap between the gating and sample surface is controlled using the piezo nanocube, in order to achieve a more precise and flexible control.

(a) illumination   **(b) Back focal plane**
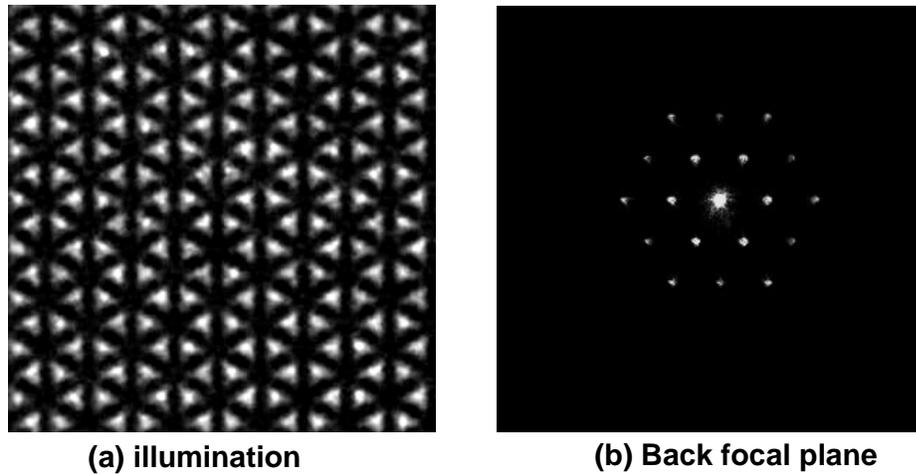
Figure 5.10 (a) Intensity pattern of the grating projected onto the sample plane, and (b) the back focal plane channel

Figure 5.10 shows the illumination pattern and its spectrum at the aperture plane. It is apparent that the illumination pattern is the self image of the grating with a good contrast. The most important aspect is that this triangle grating has frequency components every 60 degrees instead of only vertical and horizontal ones. The frequency domain is better filled by these harmonics. Comparing figure 5.10(b) with figure 5.3(b), the advantage of triangle grating is clear that the harmonics work as carrier and extend the bandwidth in a more isotropic manner.

The other system parameters are the same as with the square grating experiment, with the system bandwidth set to $NA_{eff} = 0.17$. Figure 5.11 shows the image obtained using the zero order and the PGSIM enhance image. Also shown are the counts of particles with respect to the FWHMs.
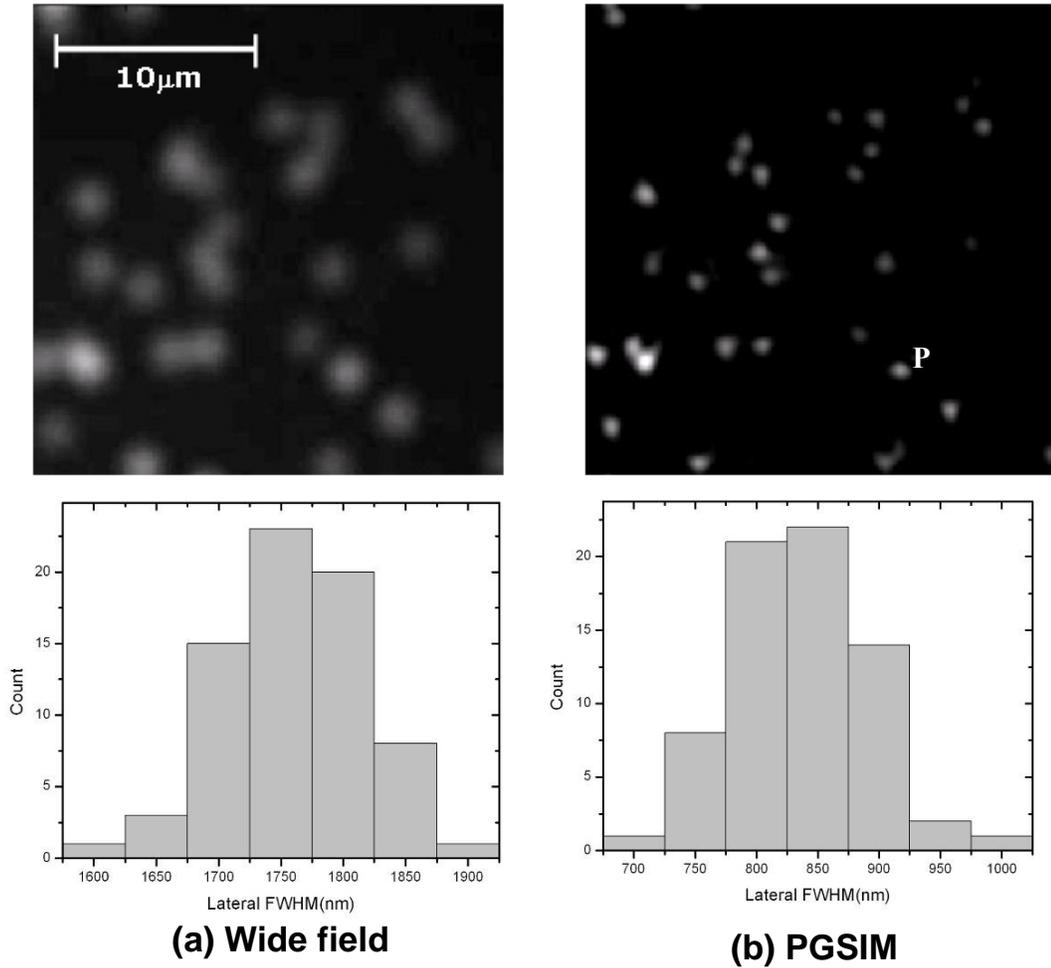
Figure 5.11 (a) Image of fluorescent beads using reduced aperture (NA = 0.17), (b) reconstructed image using the zero, ±1 & ±2 orders, Fourier components of the intensity pattern

Figure 5.12 shows the horizontal intensity profiles across the particle labelled 'p' in figure 5.11(b). The two curves, labelled 1& 2, are for the wide field and the PGSIM. The sidelobes associated with curve 2 is now about 6% of the peak value, as compared to 11% for the square grating, indicating that the triangle structure illumination extends the bandwidth in more directions.
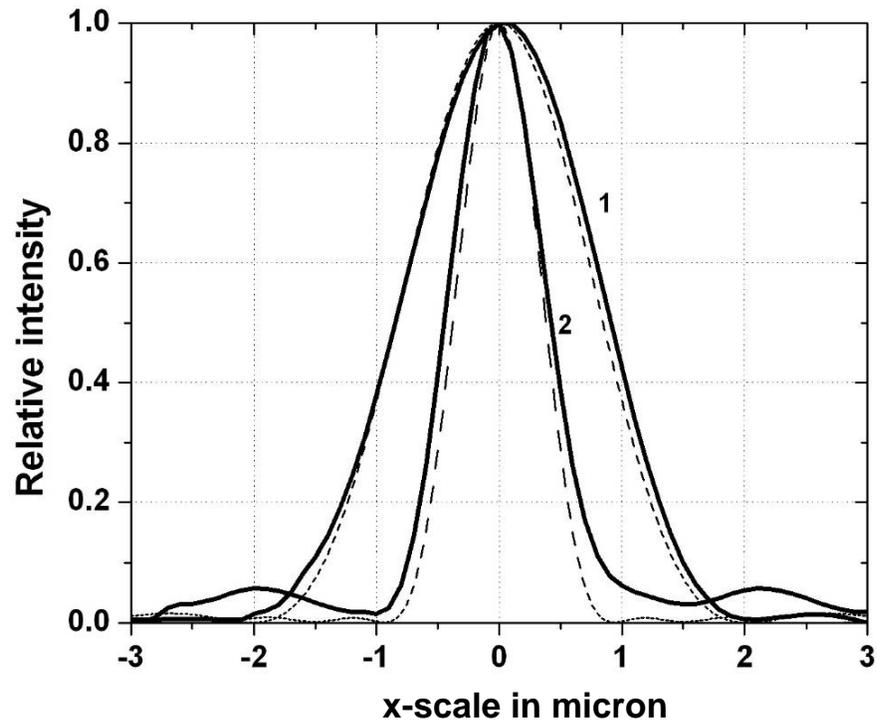
Figure 5.12 Intensity profiles of the fluorescent bead labelled P in figure 5.9(b). Profile 1: obtained using the reduced NA of 0.17; Profile 2: reconstructed using the zero, ±1 & ±2 orders. Dashed lines are simulated profiles using NA of 0.17 and 0.35 respectively.
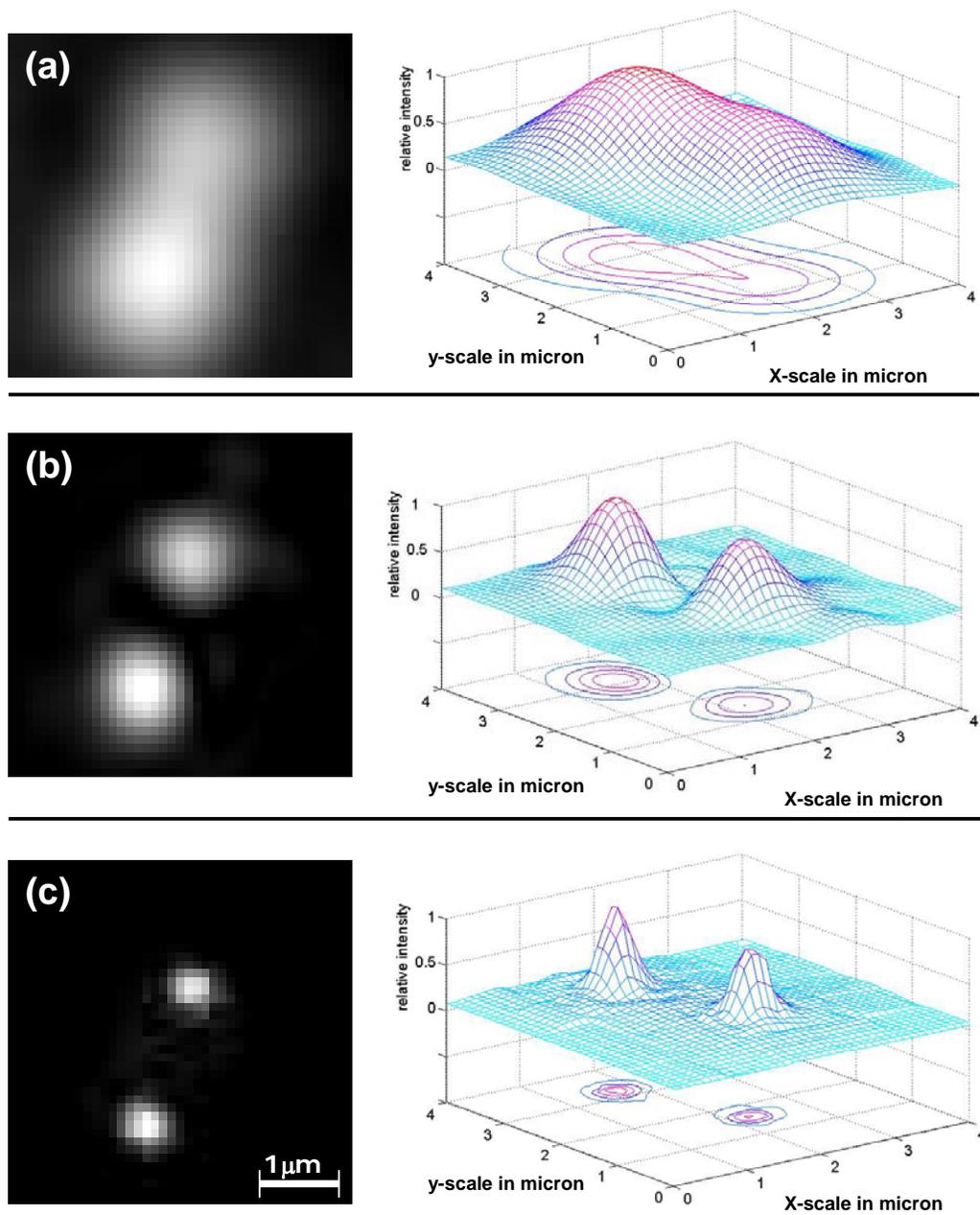
Figure 5.13 (a) Image of fluorescent beads using reduced aperture (NA = 0.17), (b) reconstructed image using the zero, ±1 & ±2 orders (NA = 0.35), (c) image with full open aperture as reference (NA=1.25).

Another interesting result is shown in figure 5.13. Two neighbouring particles

are imaged by PGSIM. The distance between them is about 1.4μm, which is beyond

the microscope resolution (Figure 5.13(a)). After reconstruction, the PGSIM resolves the two particles (Figure 5.13(b)). It is a similar example as the result shown in Figure 5.11, but this time the mesh chart is used to present the 3D profile. The sidelobes still exist but their magnitude is smaller. The mesh chart shows a more isotropic high resolution result.

If using the FWHM of the PSF to calculate the system effective NA, we demonstrate that PGSIM enhance the resolution from NA=0.17 to NA=0.35. The conclusion can be drawn that the lateral resolution has been improved by a factor of 2.06.

5.3 Discussion

In this chapter we have demonstrated experimentally the improvement, using PGSIM, in imaging NA by a factor of greater than 2 compared to conventional optical microscope. As discussed, the key component of the system is the sample unit, and in particular, the proximity grating. When choosing the grating the important parameters to consider are the grating period, its aspect ratio and the grating shape. The objectives are to maximise the coverage in the frequency domain by the virtual apertures with illumination orders of sufficiently high SNR. The suitable grating period T_0 is given in Eq. 3.13, or, if overlap of the neighbouring apertures is desired,

$$T_0 = m\frac{\lambda_0}{n}$$

where *m* is the grating order. Overlapping of the different apertures is important as it will increase the system signal to noise ratio and also reduce the sidelobes of the reconstructed image.

Figure 5.14 shows results obtained from computer modelling of the intensity point spread functions generated using two different grating patterns: square and triangular. The computer program which simulates the PGSIM system has been described in chapter three. Along each grating direction, two grating orders are used (therefore four virtual apertures along each direction, ignoring the zero order), and a Chinese hat transfer function is assumed for the virtual aperture. After summing the contributions from all the apertures, the resultant transfer function is normalised to have a Chinese hat envelope. The procedure is illustrated clearly in 1D in Figure 3.13.
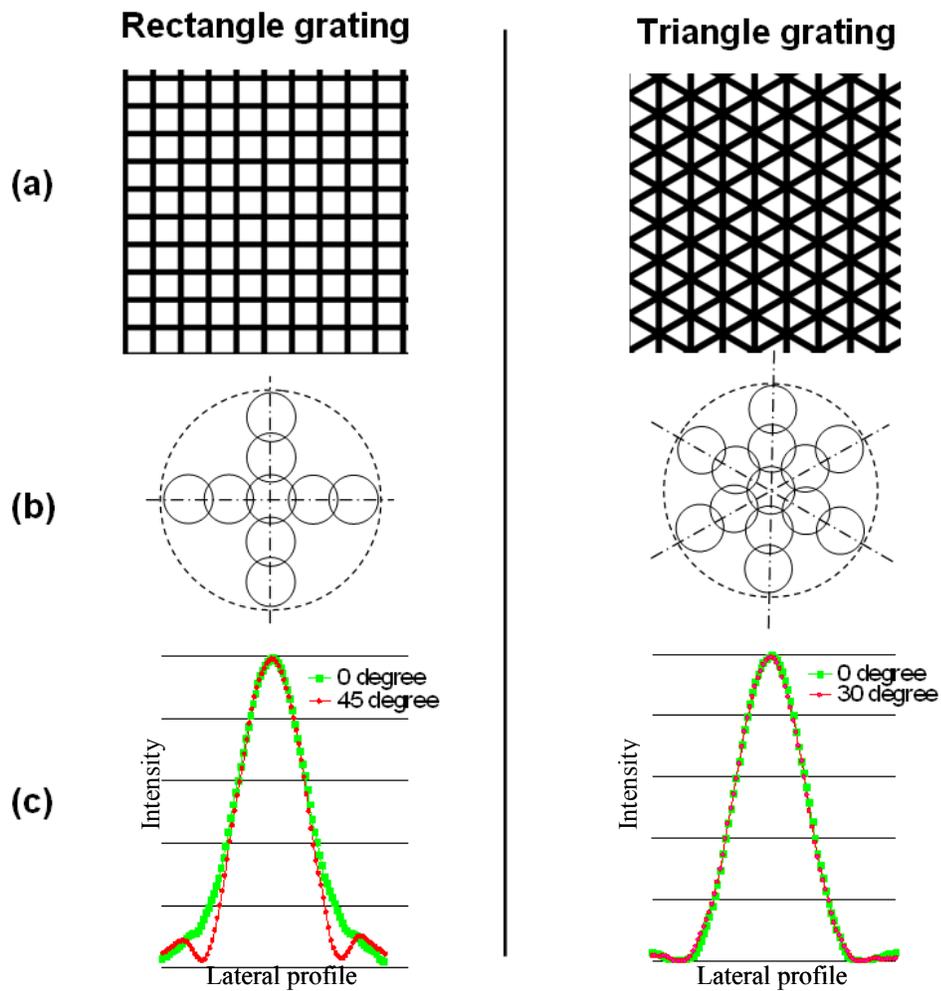
Figure 5.14   Computer simulations of point spread functions using a square grating pattern and a triangular. Column (b) shows locations of the virtual apertures, and column (c) the intensity point spread functions along grating directions and direction between them.

Figures 5.14 row (a) shows the square and triangular grating patterns. The

transfer functions supported by these patterns are shown in row (b). The small circles

represent the system (or virtual) apertures. The amount of overlap used is equal to

25% of the radius of the system aperture. The intensity point spread functions for the

two cases are shown as row (c). For the square grating pattern, the PSF is slightly

wider and has larger sidelobes which is about 11% of the peak value. Furthermore,

the PSF is not so isotropic (the vertical and horizontal profile is a little wider than 45

degree). For the triangular case, however, the differences are so small they are

negligible.

Towards the end of 5.2.1, we mentioned the lack of signal after reconstruction

in the frequency domain. This drawback is reduced effectively with the triangle

pattern. If we compare the images of an isolated particle obtained using the two

arrangements, the isotropic improvement is ever clearer.
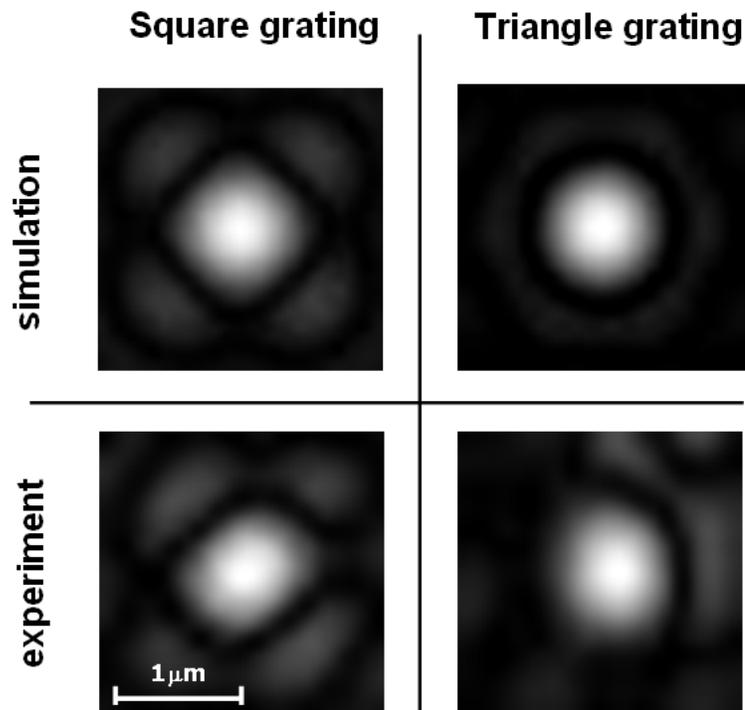
Figure 5.15 Numerical and experimental point spread function in PGSIM with
square and triangle grating. Because of the lack of signal along 45 and -45 degree in

square case, there are sidelobes along these directions. In the triangle case, the PSF is more isotropic.

5.4 Conclusion

A custom 2D grating is used to produce an illumination pattern practically. This high spatial frequency illumination can extend the system bandwidth by mixing and shifting the high spatial frequency information which is originally out of the bandwidth. By means of the projection grating, PGSIM breaks the barrier of conventional SIM. In this chapter, we have demonstrated experimentally the improvement in imaging NA by a factor of 2.06.

The optical power efficiency is important and it is associated with two factors: pattern on-off ratio and the propagation distance. We designed the grating with 80%-20% ratio to ensure more energy is coupled to the first and second harmonics. Higher intensity harmonics make good SNR to work as carriers. In addition, by controlling the gap between the grating and sample surface, we can ensure all frequency components are constructive. In practice, a piezo stage is employed to control precisely the propagation distance. The illumination patterns used all exhibit high intensity contrast.

The grating pattern is also discussed and examined experimentally. Triangle

grating has harmonics which cover most of the frequency domain. It is demonstrated that triangle grating design has better image quality (PSF with lower sidelobes).

The practical approach to the implementation of PGSIM has been successfully developed. It is fast and has large field of view. After reconstruction, the lateral resolution improvement is clear. The suggestion for future work and the system instrument improvement will be discussed in next chapter.

Chapter 6 Discussion, Conclusion and Suggestion for Future Work

In this thesis, we have demonstrated the principle behind the proximity grating projection illumination microscope. We have also shown experimentally that the technique can provide an imaging NA more than twice of the original imaging system. In this section, we will discuss this technique in several practical points of microscopy concern. The strengths and shortcomings of PGSIM will be discussed and comparing with other state-of-the-art super-resolution fluorescence microscopy. In the end, the conclusion and future work will be given.

6.1 Discussion

6.1.1 Imaging performance

The imaging performance will be discussed first. The resolution improvement behind the SIM is based on the illumination pattern, and is increased as the illumination pattern becomes finer. The pattern generating method is therefore crucial if the resolution of the conventional SIM is to improve further still. PGSIM provides a novel method to create such a fine illumination pattern.

Due to the limitation of the illumination NA, conventional SIM can extend

the system bandwidth by up to a factor of two (section 2.3). In PGSIM, because the grating is held close to the sample, with the medium in between filled with high refractive index material, a much finer illumination pattern can be created, thus improving the system resolution compared to SIM. This is demonstrated by experiments shown in chapter 5, where the improvement obtained was 2.1. The effective NA of PGSIM has been discussed in the section 3.5, and is shown to be given by $NA_{eff} = n + NA$, where n is the refractive index of the optical thin film and NA the numerical aperture of the imaging system (Eq. 3.19). The influence of the pattern shape has been discussed in both chapter 3 and 5. A comparison of the PSFs obtained using a square grating and triangular grating has been presented in figure 5.14. The choice of the grating pattern is governed by two considerations: the coverage in the frequency domain by the virtual apertures and the extent of the sidelobes associated with the PSF. From figure 5.14, we can conclude that the triangular grating is more desirable compared to the square one, on account of the smaller sidelobes it can provide. In this section, we will explore further, using computer simulation, the effects of the coverage in the frequency domain by the virtual apertures.

The simulation parameters are:

- Dry objective lens, NA=0.7.
- Optical wavelength = 550nm.

- Three triangle gratings with periods = 0.22µm, 0.44 µm, and 0.66µm,
- Grating on-off ratio 80%-20% for each.
- Refractive index of thin film n=2.5.
- Thickness of thin film is set at one Talbot distance, 176nm, 704nm, and 1584nm respectively for the three different grating periods.
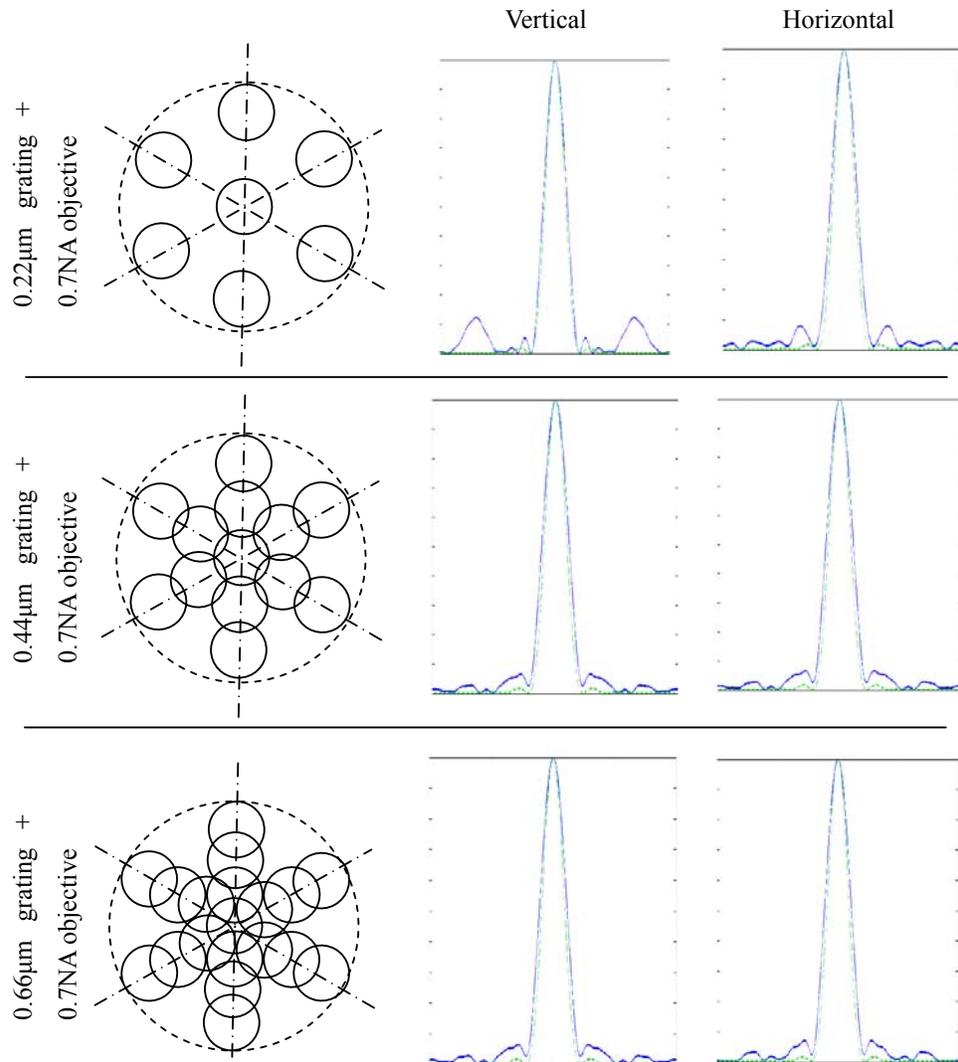
Figure 6.1 Computer simulations of PSFs using three triangular grating patterns . Column 1 shows locations of the virtual apertures; column 2 and 3 provide the intensity PSFs along vertical (along frequency components direction) and horizontal (between frequency components directions). Also shown in column 3 is the PSF (dashed curve) obtained using the ideal large aperture (large dashed circle in column 1) which the effective NA is equal to 3.2.

The purpose of selecting these three grating periods and the 0.7 imaging NA

is that they provide different amount of coverage in the frequency domain, and still

retain the same maximum frequency extent, as shown by the dashed circles in the

first column of the figure, with the equivalent NA of the dashed circle being 3.2. For

the 0.22μm grating, only one illumination order exists along each grating direction.

For the 0.44μm and 0.66μm grating, additional virtual apertures appear, with the

amount of overlap equaling 10% and 40% respectively.

Columns 2 and 3 in figure 6.1 show the PSF along the vertical and the

horizontal directions. Also shown is the PSF obtained if the system transfer function

is given by the outer dashed circle (i.e., an imaging system with spatial frequency

cutoff equivalent to the outer circle). From the figure, it is obvious that the amount of

coverage has little effect on the width of the PSF, but the sidelobes are affected. It is

important to point out that, overlap beyond 10% does not really have much

significant effect on the sidelobes, as are shown by the 0.44μm and 0.66μm gratings.

The FWHM of the PSF and the sidelobes, for the plots in figure 6.1, column 2 and 3,

are tabulated in Table 6.1 for comparison.

	vertical		horizontal	
	Normalised FWHM	Magnitude of sidelobe	Normalised FWHM	Magnitude of sidelobe
Ideal (NA$_{eff}$=3.2)	1	1.7%	1	1.7%
0.22 μm grating + objective (gap between virtual apertures)	1.11	20%	1.13	12%
0.44 μm grating + objective (10% overlap between virtual apertures)	1.18	8%	1.18	8%
0.66 μm grating + objective (40% overlap between virtual apertures)	1.18	7%	1.18	8%

Table 6.1 Simulation intensity PSF. FWHM is normalized with respect to the width of the ideal one. Magnitude of sidelobes is expressed as a percentage of the peak of the mainlobes.

6.1.2 Other considerations

Apart from the lateral resolution, there are other issues that are of concern when considering the performance of a microscope [87]. Some of these are issues related to biological imaging, such as the ability to image time series of living samples and multidimensional imaging. Others are more general, including the ease of operation and the reliability of the results. Figure 6.2 lists the challenges and trade-offs in super-resolution microscope, and the following discussion will divide into several points for microscope application.
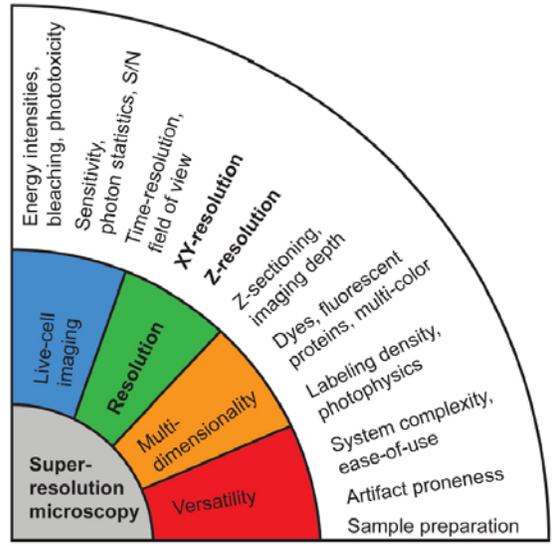
Figure 6.2 Challenges and trade-offs in super-resolution fluorescence microscopy. Although the nominal lateral (xy) and axial (z) resolution of a microscope is the most prominent system parameter, the usefulness for broader or routine application depends on other additional criteria. Notably, none of the currently available super-resolution technologies fulfill all criteria. [87]

Z resolution and Imaging depth

The PGSIM provides lateral illumination pattern to improve the XY-resolution, but the there is no improvement along axis direction shown in this thesis. However, as shown in figure 3.6, the illumination also varies along the axial direction, and this characteristic can be used potentially to improve the Z resolution of the system. The details will be discussed in the section of future work (6.3.2).

In our PGSIM system, high spatial frequency can propagate in high refractive index thin film. However, internal totally reflection may happen at the thin film-sample surface if the propagating angle is larger the critical angle. It means the PGSIM can deal with surface structures and dynamics with high resolution, but

provide the interior study with lower resolution. Generally, the refractive index of biology environment is about 1.3 (depends on organelle), and it will become the limit of PGSIM instead of thin film refractive index if we apply PGSIM in cell interior.

Field of view

With many microscopy techniques, such as solid immersion lens, high image resolution is usually achieved at the cost of limited field of view. For PGSIM, however, the final image is reconstructed using several low NA images. As long as the original images are sampled satisfying the Nyquist condition, the reconstructed image will have both high resolution and retain the original field of view. The limiting factors are as described in section 3.1.5, which are the size of the grating and also the edge effect. Both are engineering problems that can be solved.

Temporal resolution

The majority of the published work in the area of super resolution microscope concerns cellular structures in fixed cells. However, the biological processes are dynamic, and quick temporal resolution is required to study structural changes in a

cell and cell interactions with the environment. Among these super resolution techniques, SIM is promising to do real time imaging. Although a number of raw images need to be recorded, they can be completed in seconds. The data processing time is relatively short and can also be processed off line. For PGSIM, depending on the number of reconstruction orders used (see figure 6.1), the situation would either be the same as SIM, or possibly requiring two times more images for reconstruction. In any case, imaging of live samples is a real possibility.

Dyes

An attractive feature of structured illumination for cell biological applications is that standard dyes and staining protocols can be used. Since no special photo physics is needed for PGSIM, virtually all modern fluorescent labels can be used. It provides sufficient photostable to accommodate the additional exposure cycles. From the point of dyes, PGSIM is the most flexible approach and allows more application. However, dyes for other super resolution techniques, such as SSIM, STED, and STORM, all need special characteristics.

System complexity, and sample preparation

A novel technique will certainly be used if it is simple to set up. One significant

advantage of PGSIM is its simplicity. Since many commercial microscopes have already the facility of laser scanning, PGSIM can be implemented on them directly. The grating unit can be used to replace the sample substrate, and the rest facilities can keep the same without much modification. As mentioned before, it is compatible with a simple and straightforward strategy for sample labeling with fluorescent probes or other labels, and there are no special demands for sample preparation. PGSIM shows a relatively user-friendly strength comparing with other super resolution techniques.

From the above discussion, we can have a simple conclusion for PGSIM. This technique is based on the conventional structured light microscope. It keeps the strength of light microscope, such as large field of view and high temporal resolution. Compard with other super-resolution techniques, the sample preparation is relatively easy and there is no special demand for dyes. Although the extreme lateral resolution limit is not as high as 20nm which other super resolution techniques may achieve, it provides a sample-friendly condition with capability of living cell imaging. A user-friendly characteristic is also an advantage.

6.2 Summary

For centuries, biological research has been based on light microscopy and been limited by its resolution at the same time. Obtaining images at sufficiently high resolution for biological and other applications is one of the primary tasks of research in optical microscopy.

This project studied one of the most promising high resolution techniques, structured illumination microscopy (SIM). Discussions in the spatial frequency domain, presented in Chapter 2, have provided a clear picture of the principles of SIM. The high spatial frequency information of the sample is down-converted into the optical system aperture, even though they are outside of the system bandwidth originally. The k-vectors of the illumination pattern play an important role in the process, and an appropriate reconstruction algorithm is needed to synthesis the final extended bandwidth, thus achieving image resolution beyond that can be afforded by the conventional optical microscope.

However, there is a physical limit regarding the resolution an SIM can achieve. This is due to the approach of illumination adopted by SIM. In the original set up, two parallel light beams are used to interfere at the sample, thus creating a sinusoidal illumination pattern. The finest pattern that can be achieved is governed

by the NA of the illumination optics, or in a reflected light microscope by the NA of the objective lens. This is why the resolution improvement of SIM is limited to a factor of 2 of the original value.

A high spatial frequency illumination pattern, which is higher than the illumination optics can afford, can provide further resolution improvement. To achieve this goal, we have designed a proximity projection grating unit, which takes advantages of a very fine grating structure, and a high refractive index material sandwiched between the grating and the sample. The latter is therefore illuminated by an intensity pattern consisting of very high k-vectors. At the sample surface, the values of the k-vectors are no longer restricted by the illumination optics, but by the refractive index of the thin film material. Indeed we have shown in Chapter 3 that the resolution for such a system increases with increasing refractive index. To complete the imaging process, phase stepping is required. This is accomplished by changing the incident angle of the light beam illuminating the grating unit. Chapter 4 contains experimental results showing the phase shift of the light pattern at the sample surface as the incident light beam is scanned over an angular range of ±3 degree. The linear phase relationship is what is expected from design.

The design of such a sandwiched structure sample holder has two chief considerations: the shape of the grating pattern and the thickness of the high

refractive index material. The grating pattern determines the coverage in the

frequency domain by the virtual apertures and the eventual extension of the system

bandwidth. From simulations, a triangle pattern can provide harmonics in three

directions and cover enough regions in the frequency domain for the final image to

have minimum artifact. The thickness of the high refractive layer determines the

magnitudes of the different illumination orders. The intensity pattern at the sample

surface can be explained using the Talbot effect, where the diffraction pattern will

repeat itself at regular distances from the grating and is known as the Talbot distance.

Chapter 4 shows comparisons of the intensity patterns obtained from simulations and

experiment, at five different thin film thicknesses, for both square and triangular

gratings. The similarities between the theoretical and experimental results are

striking.

Proper grating pattern design and thickness control can provide a unique high

spatial frequency illumination with optimum signal to noise ratio for all the

illumination orders used. Theoretically, an oil immersion objective lens combining a

high refractive index material (n=2.5) can produce a PGSIM system with effective

NA =4.

In chapter 5, we have demonstrated the PGSIM capability experimentally. A

number of samples consisting of well characterized fluorescent beads have been used

for this purpose. Images were obtained using a conventional set up, the PGSIM set

up with one illumination order, and PGSIM with two illumination orders. The ratio

of the effective bandwidths of the three is 1 : 1.65 : 2.18, thus showing a resolution

improvement of greater than 2. PGSIM can distinguish two close fluorescent beads,

which are unresolved in a conventional microscope. It shows the resolution

improvement clearly. In addition, we also use a triangle grating to obtain a more

isotropic image, and the results show lower sidelobes than results from square

grating. The practical approach to the implementation of PGSIM has been

successfully developed, and the goal of this project has been done and demonstrated.

6.3 Suggestion for Future Work

In this section, we will describe future work that will potentially improve the working of the system as well as providing further applications. The system is composed of three parts: illumination arm, sample holder (grating with thin film), and imaging arm. The imaging arm is the same as a conventional fluorescence microscope, so the following sections will concentrate on illumination arm and the sample holder.

6.3.1 Sample holder

The experimental results shown in this thesis are obtained using immersion oil as the thin film material to fill the gap between the grating and sample. It is a low NA set up as the refractive index of the oil is 1.512 only. It is adequate for demonstrating the capability of the relative resolution improvement of the technique. As mentioned in the section 4.2.3, this thin film is a vital element and affects the performance of the technique. The use of immersion oil also entails other problems. The difficulties in controlling its thickness and in setting the top and bottom surface parallel are but two examples. A more desirable method is to coat a thin layer of transparent material on the grating. Table 6.2 lists some promising materials that are suitable for this purpose. They are all of higher refractive index. Furthermore, a solid and robust thin film would allow different specimen to be examined and reduces the possibility of the

sample unit to be damaged, and is therefore important as far as its practical usage is

concerned. Further research is needed to investigate if it is possible to evaporate

micron thin layer of material onto the grating.

Material	Formula	Index of refraction @ 550nm	Transparency Rang (µm)
Gallium Phosphate	GaP	3.5	0.4-10.0
Titanium Oxide	TiO_2	2.4	0.45-11.0
Tantalum Oxide	Ta_2O_5	2.1	0.3-10.0
Antimony Oxide	Sb_2O_3	2.1	0.3-10.0
Zirconium Oxide	$Zr\,O_2$	1.96	0.3-11.0

Table 6.2 promising material for thin film.

6.3.2 Illumination arm

The aim of the illumination arm is to provide an oblique incident parallel light.

In this thesis, we used a laser unit mounted on a 2D translation stage to change the

incident angle.   Although the set up functions well for our requirement, it was quite

time consuming. To this end, a programmable array of light source may be used. This

can be a light source used in conjunction with a spatial light modulator, or a LED

array that can be controlled individually. By placing the modulator or the LED array

at the back focal plane of condenser L_c in figure 4.2, we can dispense with the need

of any mechanical scanning. With this scheme, we need to consider the light

through-put or the divergence and the spectral width of the LEDs, in order to ensure

the proper operation of the system.

6.3.3 Widefield imaging with optical sectioning

As demonstrated in Chapter 3, the light distribution behind the optical grating is

a function of the grating period, the refractive index of the thin film material, and

also the distance from the grating. Figure 3.5 shows a simulation of the intensity

pattern as a function of the distance from the grating, and as can be seen, it consists

of bright and dark regions. The illumination, therefore, can be considered as

comprising of volumes of light, confined in all three dimensions. This potentially

provides a basis for optical sectioning, leading to 3D imaging. In order to realise the

latter, we need to be able to scan the bright volumes of light in the x-y plane as well

as axially. Scanning in the x-y direction has already been demonstrated (figure 3.9).

The key to move the bright volume axially is to change the spatial frequency

components of the diffracted orders inside the thin film. A potentially promising way

of doing this is to impose certain structure onto the illumination beam. The mixing of

the illumination and the grating will produce spatial frequency components different

from those of the grating alone. A suitable set up for such a system will therefore

consist of a laser beam passing through a spatial light modulator before incident onto

the grating unit. Figure 6.3 shows the intensity profile as a function of z, the

distance form the grating, obtained at a particular point in the x-y plane. This

intensity oscillation demonstrates the light confinement in the axial direction. By

alternating the spatial frequency components of the illumination, it is expected that

the oscillation will change in phase, thus covering the entire sample. The

implementation of such a set up may prove to be the most powerful application of the

technique.
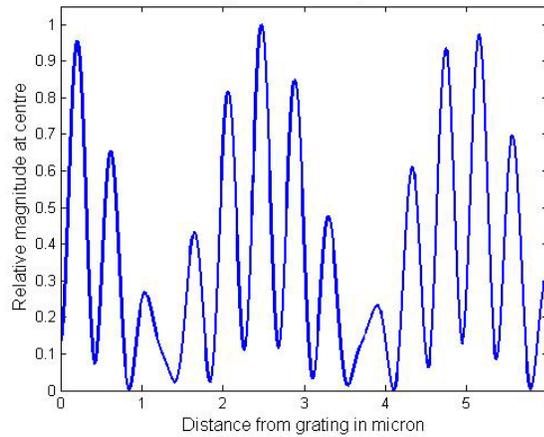
Figure 6.3 Intensity at centre of the light spot as the thickness of the thin film, d, changes from 0 to 6μm.

In conclusion, the usage of the grating unit described in this thesis is not

restricted to SIM, and the various diffraction patterns afforded by the unit provide

much potential for other applications, and as such, for future research areas.

Appendix A

Phase shift caused by angle scanning

SIM acquire images at various illumination phase to do reconstruction. For PGSIM, the illumination pattern is projected through thin film and can be shifted by changing the incident angle. As described in chapter 3, the shift is associated with the thickness of thin film and the incident angle. We simulate the 1D illumination pattern distribution on one Talbot distance Z_t, and scan the incident angle to obtain the relationship between lateral phase shift and incident angle.

Factors of simulation:

Wavelength λ: 550nm

Grating period L: 0.5μm, 1μm, 2μm, 4μm; 80% transparent and 20% opaque

Thin film: refractive index: 1.5, thickness: L^2/λ

Scan angle: 0^0 to 10^0
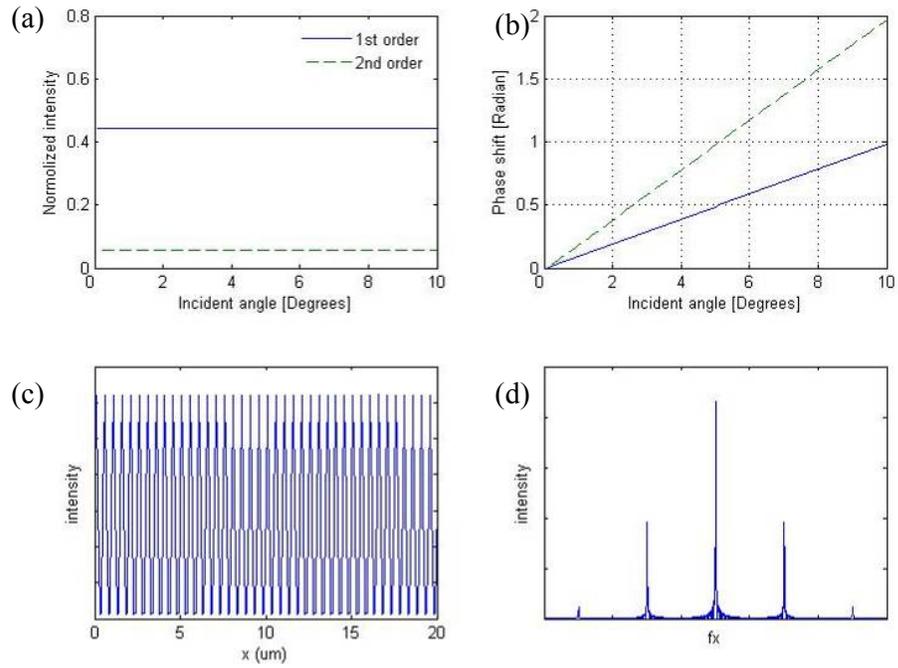
Figure A.1 0.5µm Grating diffraction pattern at Z_t with incident
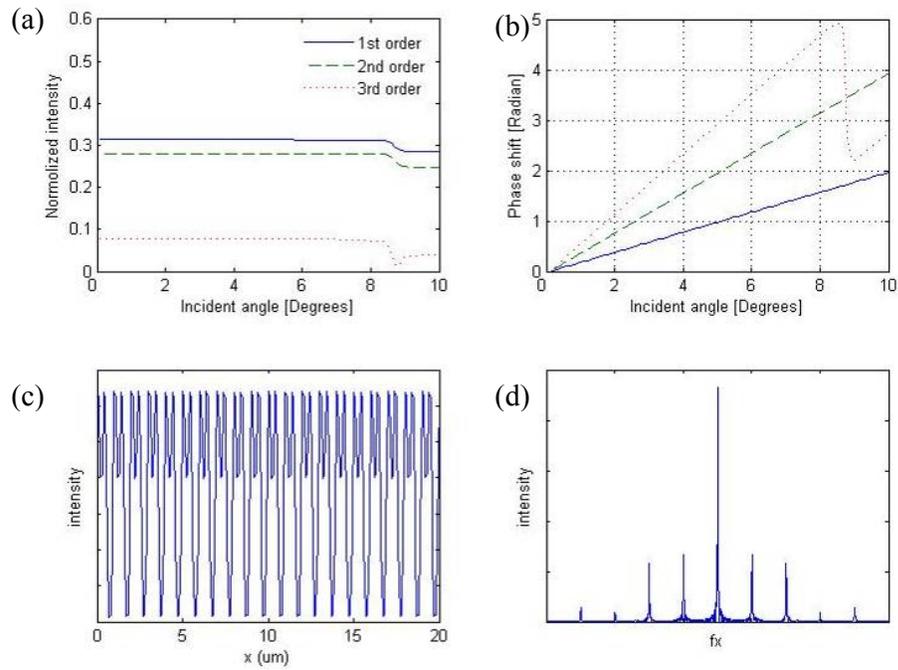
Figure A.2 1µm Grating diffraction pattern at Z_t with incident
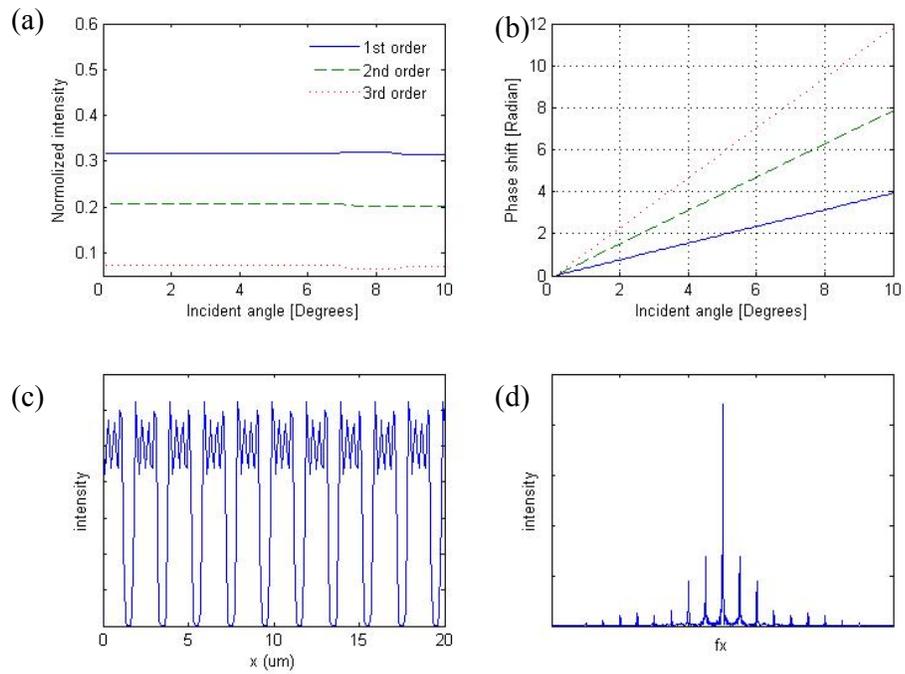
Figure A.3 2μm Grating diffraction pattern at Z_t with incident
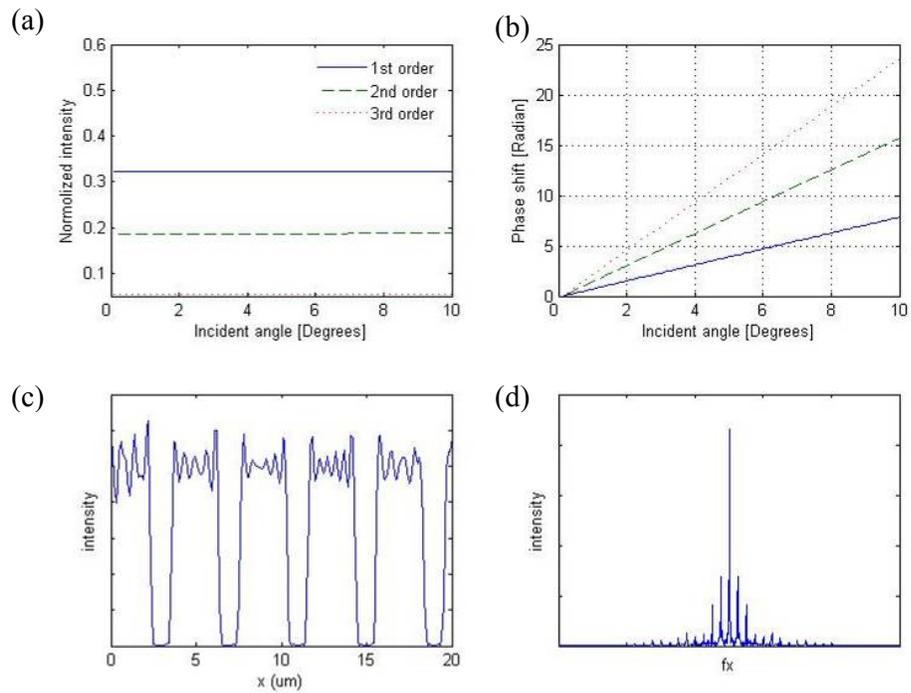
Figure A.4 4μm Grating diffraction pattern at Z_t with incident

The bottom of each figure shows the illumination intensity profile and its harmonics orders. In general, the lateral shift is proportional to the incident angle and the harmonics order. In the small angle ($<5^0$) the intensity distribution keeps constant; magnitude of each harmonics order stay the same when scanning the incident angle. It demonstrates that the incident angle causes pure lateral shift without altering the shape for the illumination.

Appendix B

PGSIM System Specifications

A laser beam (frequency doubled Nd:YAG, 532 nm) is focused onto the back focal plane of the condenser lens L_C (focal length = 30mm). After the sample unit, an objective lens (Zeiss CP Achromat x100 1.25 oil) is used to image the sample, via a set of imaging optics, to a CCD camera (Andor iXON EMCCD, 1002 x 1002 pixels, size 8 x 8 μm^2). The magnification of the imaging system is x80, making the effective pixel size at the sample surface 100 x 100 nm^2. A variable aperture is included in the imaging optics to control the numerical aperture of the system. Also included is a band-stop filter (Chroma Technology Corp. Z488/532m) that allows for fluorescent operation.

The illumination unit (IU) is mounted on a x-y scan stage. Moving IU laterally will allow the incident beam to change angle at the sample unit. The grating consists of a 40 nm thick Cr layer, in the form of a square grid and triangle, deposited on a 220 μm thick glass substrate. The period T_g of the square grid is 3 μm, and the width of the grid line is 0.6 μm. The sample unit is controlled by piezo nanoCube. The gap is modulated at 67.7μm which is twice the Talbot distance and the self image appear on the sample surface.

With the above parameters, an angular scan of the illuminating beam over 2.5 deg will shift the projected grating pattern by one period at the sample surface. This scan angle is sufficiently small for the projected pattern to retain its shape at the sample surface. The angular scan is achieved by moving the illumination unit by a distance of 1.32mm.

The key apparatus in this set up include:

(1) Laser

The light source is a diode pumped solid state laser from B&W TEK INC. The brief specifications are given below:

Specifications of B&W diode solid state	
Wavelength	532nm
Max power	50mW
Beam diameter	≈1mm
Beam divergence (Full angle)	<1mrad
RMS Noise stability	<0.5%

(2) xy stage

Two 1D motor stages from PI are used in the illumination unit(IU). The brief specifications are given below:

Specifications of m-112.1DG	
Travel range	25mm
Unidirectional repeatability	0.1 μm

Minmus incremental motion	0.05μm
Max normal load capacity	2kg

(3) piezo nanoCube

The piezo nanoCube is used to control the grating holder in the sample unit.

The brief specifications are given below:

Specifications of p-611.3	
Travel range	100μm/axis
resolution	0.2nm
Max load capacity	15N

(4) objective lens

The objective lens is a 1.25 NA 100x Achromatic oil immersion objective

from Zeiss. The brief specifications are given below:

Specifications of 1.25 100x oil immersion objective lens	
magnification	100x
Numerical Aperture	1.25
Working distance	0.23mm
Coverglass thickness	0.17
immersion	Oil

(5) CCD camera

The CCD camera is from andor. The brief specifications are given below:

Specifications of iXon X3 885 EMCCD camera	
Active pixels	1004×1002
Pixel size	8×8μm
Read noise	<1e with EM gain

(6) Emission filter

The emission filter z488/532m is used in the florescent microscope. It will

block the laser (532nm) and is transmitted in 550nm. The transmission curve

is shown below:
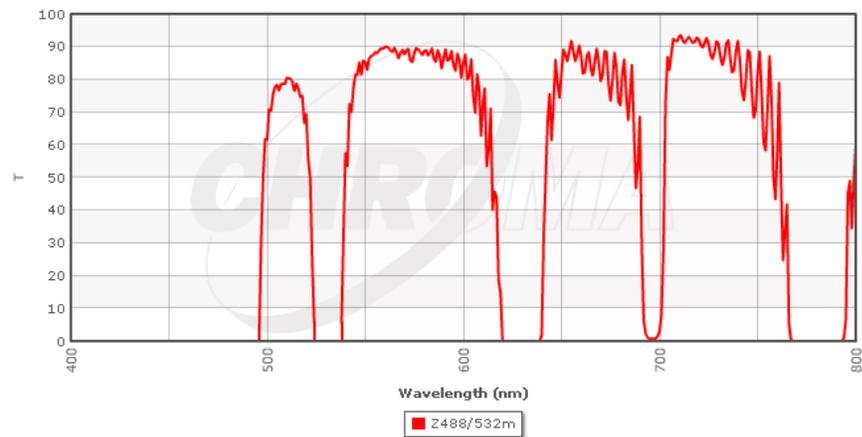
References

1. B. Harke, J. Keller, C. K. Ullal, V. Westphal, A. Schoenle, and S. W. Hell, "Resolution scaling in STED microscopy," Opt. Express **16**, 4154-4162 (2008).

2. M. J. Rust, M. Bates, and X. W. Zhuang, "Sub-diffraction-limit imaging by stochastic optical reconstruction microscopy (STORM)," Nat. Methods **3**, 793-795 (2006).

3. M. G. L. Gustafsson, "Surpassing the lateral resolution limit by a factor of two using structured illumination microscopy," J. Microsc.-Oxf. **198**, 82-87 (2000).

4. C. W. See, C. J. Chuang, S. G. Liu, and M. G. Somekh, "Proximity projection grating structured light illumination microscopy," Applied Optics **49**, 6570-6576 (2010).

5. S. Liu, C. J. Chuang, C. W. See, G. Zoriniants, W. L. Barnes, and M. G. Somekh, "Double-grating-structured light microscopy using plasmonic nanoparticle arrays," Opt. Lett. **34**, 1255-1257 (2009).

6. R. O. Frischknecht F, Shorte SL, "Imaging today's infectious animalcules.," Current Opinion in Microbiology **9**, 297-306 (2006).

7. E. Abbe, "Beiträge zur Theorie des Mikroskops und der mikroskopischen Wahrnehmung," Archiv für Mikroskopische Anatomie **9**, 5 (1873).

8. M. Abramowitz, *Microscope basics and beyond* (Olympus America Inc, 2003).

9. J. R. Lakowicz, *Principles of Fluorescence Spectroscopy* (Springer, 2006).

10. M. W. D. Kenneth R. Spring, "Introduction to Fluorescence Microscopy," (Nikon, 2011).

11. M. W. Davidson, "Resolution," (Nikon, 2011), http://www.microscopyu.com/articles/formulas/formulasresolution.html.

12. J. W. Goodman, *Introduction to Fourier Optics* (Roberts & Company Publishers, 2004).

13. G. Sluder, and J. J. Nordberg, "Microscope basics," Digital Microscopy, 3rd Edition **81**, 1-10 (2007).

14. H. H. Hopkins, "The airy disc formula for systems of high relative aperture," Proceedings of the Physical Society **55**, 0116-0128 (1943).

15. E. H. K. Stelzer, "Contrast, resolution, pixelation, dynamic range and signal-to-noise ratio: fundamental limits to resolution in fluorescence light microscopy," J. Microsc.-Oxf. **189**, 15-24 (1998).

16. H. E. Bennett, and J. M. Elson, "Rayleigh and other resolution criteria," Journal of the Optical Society of America a-Optics Image Science and Vision **2**, P32-P32 (1985).

17. C. M. Sparrow, "On spectroscopic resolving power," Astrophysical Journal **44**, 76-86 (1916).

18. T. Bernas, "Basics of digital microscopy," Curr Protoc Cytom **Chapter 12**, Unit 12.12 (2005).

19. Y. Kuznetsova, A. Neumann, and S. R. J. Brueck, "Imaging interferometric microscopy - approaching the linear systems limits of optical resolution," Opt. Express **15**, 6651-6663 (2007).

20. M. A. Hayat, *Principles and Techniques of Electron Microscopy: Biological Applications*

(Cambridge University Press, 2000).

21. R. M. Glaeser, and K. A. Taylor, "Radiation-damage relative to transmission electron-microscopy of biological specimens at low-temperature - review," J. Microsc.-Oxf. **112**, 127-138 (1978).

22. M. B. Wabuyele, M. Culha, G. D. Griffin, P. M. Viallet, and T. Vo-Dinh, "Near-field scanning optical microscopy for bioanalysis at nanometer resolution," Protein Nanotechnology: Protocols, Instrumentation, and Applications **300**, 437-452 (2005).

23. E. Betzig, J. K. Trautman, T. D. Harris, J. S. Weiner, and R. L. Kostelak, "Breaking the diffraction barrier - optical microscopy on a nanometric scale," Science **251**, 1468-1470 (1991).

24. V. Subramaniam, A. K. Kirsch, and T. M. Jovin, "Cell biological applications of scanning near-field optical microscopy (SNOM)," Cellular and Molecular Biology **44**, 689-700 (1998).

25. R. Eckert, H. Heinzelmann, L. Aeschimann, U. Staufer, N. F. de Rooij, and Is, *Super-resolution imaging by scanning near-field optical microscopy with microfabricated probes* (Society Imaging Science Technology, Springfield, 2005).

26. M. Koopman, A. Cambi, B. I. de Bakker, B. Joosten, C. G. Figdor, N. F. van Hulst, and M. F. Garcia-Parajo, "Near-field scanning optical microscopy in liquid for high resolution single molecule detection on dendritic cells," FEBS Lett. **573**, 6-10 (2004).

27. J. B. Pendry, "Negative refraction makes a perfect lens," Physical Review Letters **85**, 3966-3969 (2000).

28. J. Pawley, *Handbook of Biological Confocal Microscopy* (Springer, 2006).

29. D. M. Shotton, "Confocal scanning optical microscopy and its applications for biological specimens," Journal of Cell Science **94**, 175-206 (1989).

30. J. T. Fredrich, "3D imaging of porous media using laser scanning confocal microscopy with application to microscale transport processes," Physics and Chemistry of the Earth Part a-Solid Earth and Geodesy **24**, 551-561 (1999).

31. R. Henriques, C. Griffiths, E. H. Rego, and M. M. Mhlanga, "PALM and STORM: Unlocking Live-Cell Super-Resolution," Biopolymers **95**, 322-331 (2011).

32. S. W. Hell, and J. Wichmann, "Breaking the diffraction resolution limit by stimulated-emmission-depletion fluorescence microscopy," Opt. Lett. **19**, 780-782 (1994).

33. T. A. Klar, and S. W. Hell, "Subdiffraction resolution in far-field fluorescence microscopy," Opt. Lett. **24**, 954-956 (1999).

34. M. Dyba, and S. W. Hell, "Photostability of a fluorescent marker under pulsed excited-state depletion through stimulated emission," Applied Optics **42**, 5123-5129 (2003).

35. C. Eggeling, A. Volkmer, and C. A. M. Seidel, "Molecular photobleaching kinetics of rhodamine 6G by one- and two-photon induced confocal fluorescence microscopy," Chemphyschem **6**, 791-804 (2005).

36. S. W. Hell, "Far-field optical nanoscopy," Science **316**, 1153-1158 (2007).

37. S. W. Hell, "Toward fluorescence nanoscopy," Nature Biotechnology **21**, 1347-1355 (2003).

38.   J. Gelles, B. J. Schnapp, and M. P. Sheetz, "Tracking kinesin-driven movements with nanometre-scale precision," Nature **331**, 450-453 (1988).

39.   E. Betzig, G. H. Patterson, R. Sougrat, O. W. Lindwasser, S. Olenych, J. S. Bonifacino, M. W. Davidson, J. Lippincott-Schwartz, and H. F. Hess, "Imaging intracellular fluorescent proteins at nanometer resolution," Science **313**, 1642-1645 (2006).

40.   S. T. Hess, T. P. K. Girirajan, and M. D. Mason, "Ultra-high resolution imaging by fluorescence photoactivation localization microscopy," Biophysical Journal **91**, 4258-4272 (2006).

41.   R. E. Thompson, D. R. Larson, and W. W. Webb, "Precise nanometer localization analysis for individual fluorescent probes," Biophysical Journal **82**, 2775-2783 (2002).

42.   M. Bates, B. Huang, and X. W. Zhuang, "Super-resolution microscopy by nanoscale localization of photo-switchable fluorescent probes," Current Opinion in Chemical Biology **12**, 505-514 (2008).

43.   E. Rittweger, K. Y. Han, S. E. Irvine, C. Eggeling, and S. W. Hell, "STED microscopy reveals crystal colour centres with nanometric resolution," Nat Photonics **3**, 144-147 (2009).

44.   G. Donnert, J. Keller, R. Medda, M. A. Andrei, S. O. Rizzoli, R. Lurmann, R. Jahn, C. Eggeling, and S. W. Hell, "Macromolecular-scale resolution in biological fluorescence microscopy," Proc. Natl. Acad. Sci. U. S. A. **103**, 11440-11445 (2006).

45.   B. Huang, W. Q. Wang, M. Bates, and X. W. Zhuang, "Three-dimensional super-resolution imaging by stochastic optical reconstruction microscopy," Science **319**, 810-813 (2008).

46.   M. G. L. Gustafsson, D. A. Agard, and J. W. Sedat, "Doubling the lateral resolution of wide-field fluorescence microscopy using structured illumination," Three-Dimensional and Multidimensional Microscopy: Image Acquisition Processing Vii **1**, 141-150 (2000).

47.   M. G. L. Gustafsson, "Nonlinear structured-illumination microscopy: Wide-field fluorescence imaging with theoretically unlimited resolution," Proc. Natl. Acad. Sci. U. S. A. **102**, 13081-13086 (2005).

48.   M. G. L. Gustafsson, L. Shao, P. M. Carlton, C. J. R. Wang, I. N. Golubovskaya, W. Z. Cande, D. A. Agard, and J. W. Sedat, "Three-dimensional resolution doubling in wide-field fluorescence microscopy by structured illumination," Biophysical Journal **94**, 4957-4970 (2008).

49.   L. Schermelleh, P. M. Carlton, S. Haase, L. Shao, L. Winoto, P. Kner, B. Burke, M. C. Cardoso, D. A. Agard, M. G. L. Gustafsson, H. Leonhardt, and J. W. Sedat, "Subdiffraction multicolor imaging of the nuclear periphery with 3D structured illumination microscopy," Science **320**, 1332-1336 (2008).

50.   M. J. P.-H. a. M. W. Davidson, "Oblique Illumination Light Pathways," (2011), http://micro.magnet.fsu.edu/primer/java/oblique/lightpaths/index.html.

51.   J. Z. Mário Figueiredo, Anil K. Jain, *Energy minimization methods in computer vision and pattern recognition* (2001). ISBN 978-3-540-42523-6

52.   R. Heintzmann, and C. Cremer, "Laterally modulated excitation microscopy: Improvement of

resolution by using a diffraction grating," Optical Biopsies and Microscopic Techniques Iii, SPIE **3568**, 185-196 (1999).

53. C. L. Wei, M. Y. Chen, and Z. L. Wang, "General phase-stepping algorithm with automatic calibration of phase steps," Optical Engineering **38**, 1357-1360 (1999).

54. C. L. Wei, M. Y. Chen, W. D. Hou, and Z. J. Wang, "Phase measurement algorithm without phase-unwrapping problem for phase-stepping interferometry," Laser Interferometry Ix: Techniques and Analysis **3478**, 405-410 (1998).

55. A. Sentenac, K. Belkebir, H. Giovannini, and P. C. Chatumet, "Subdiffraction resolution in total internal reflection fluorescence microscopy with a grating substrate," Opt. Lett. **33**, 255-257 (2008).

56. N. B. E. Sawyer, S. P. Morgan, M. G. Somekh, C. W. See, X. F. Cao, B. Y. Shekunov, and E. Astrakharchik, "Wide field amplitude and phase confocal microscope with parallel phase stepping," Review of Scientific Instruments **72**, 3793-3801 (2001).

57. R. Heintzmann, "Saturated patterned excitation microscopy with two-dimensional excitation patterns," Micron **34**, 283-291 (2003).

58. M. G. L. Gustafsson, D. A. Agard, and J. W. Sedat, "(IM)-M-5: 3D widefield light microscopy with better than 100 nm axial resolution," J. Microsc.-Oxf. **195**, 10-16 (1999).

59. J. Bewersdorf, R. Schmidt, and S. W. Hell, "Comparison of (IM)-M-5 and 4Pi-microscopy," J. Microsc.-Oxf. **222**, 105-117 (2006).

60. L. Shao, B. Isaac, S. Uzawa, D. A. Agard, J. W. Sedat, and M. G. L. Gustafsson, "(IS)-S-5: Wide-field light microscopy with 100-nm-scale resolution in three dimensions," Biophysical Journal **94**, 4971-4983 (2008).

61. P. Kner, B. B. Chhun, E. R. Griffis, L. Winoto, and M. G. L. Gustafsson, "Super-resolution video microscopy of live cells by structured illumination," Nat. Methods **6**, 339-342 (2009).

62. J. T. Frohn, H. F. Knapp, and A. Stemmer, "True optical resolution beyond the Rayleigh limit achieved by standing wave illumination," Proc. Natl. Acad. Sci. U. S. A. **97**, 7232-7236 (2000).

63. R. Fedosseev, Y. Belyaev, J. Frohn, and A. Stemmer, "Structured light illumination for extended resolution in fluorescence microscopy," Opt. Lasers Eng. **43**, 403-414 (2005).

64. A. Stemmer, M. Beck, and R. Fiolka, "Widefield fluorescence microscopy with extended resolution," Histochemistry and Cell Biology **130**, 807-817 (2008).

65. G. E. Cragg, and P. T. C. So, "Lateral resolution enhancement with standing evanescent waves," Opt. Lett. **25**, 46-48 (2000).

66. P. T. C. So, H. S. Kwon, and C. Y. Dong, "Resolution enhancement in standing-wave total internal reflection microscopy: a point-spread-function engineering approach," Journal of the Optical Society of America a-Optics Image Science and Vision **18**, 2833-2845 (2001).

67. E. Chung, D. K. Kim, and P. T. C. So, "Extended resolution wide-field optical imaging: objective-launched standing-wave total internal reflection fluorescence microscopy," Opt. Lett. **31**, 945-947 (2006).

68. B. Bailey, D. L. Farkas, D. L. Taylor, and F. Lanni, "Enhancement of axial resolution in fluorescence microscopy by standing wave excitation," Nature **366**, 44-48 (1993).

69. F. Lanni, and B. Bailey, "Standing-wave excitation for fluorescence microscopy," Trends in Cell Biology **4**, 262-265 (1994).

70. B. Schneider, J. Bradl, I. Kirsten, M. Hausmann, and C. Cremer, "High precision localization of fluorescent targets in the nanometer range by spatially modulated excitation fluorescence microscopy," Fluorescence Microscopy and Fluorescent Probes, Vol 2, 63-68 (1998).

71. R. Heintzmann, T. M. Jovin, and C. Cremer, "Saturated patterned excitation microscopy - a concept for optical resolution improvement," Journal of the Optical Society of America a-Optics Image Science and Vision **19**, 1599-1609 (2002).

72. R. Heintzmann, and P. A. Benedetti, "High-resolution image reconstruction in fluorescence microscopy with patterned excitation," Applied Optics **45**, 5037-5045 (2006).

73. A. Sentenac, K. Belkebir, H. Giovannini, and P. C. Chaumet, "High-resolution total-internal-reflection fluorescence microscopy using periodically nanostructured glass slides," Journal of the Optical Society of America a-Optics Image Science and Vision **26**, 2550-2557 (2009).

74. C. S. Kealley, M. D. Arnold, A. Porkovich, and M. B. Cortie, "Sensors based on monochromatic interrogation of a localised surface plasmon resonance," Sensors and Actuators B-Chemical **148**, 34-40 (2010).

75. R. S. Moirangthem, Y. C. Chang, and P. K. Wei, "Investigation of surface plasmon biosensing using gold nanoparticles enhanced ellipsometry," Opt. Lett. **36**, 775-777 (2011).

76. J. P. O. Reilly, J. D. Fisk, M. Rooth, E. Perkins, and A. M. Shaw, "Non-linear plasmon response to protein binding at a nanostructured gold particle plasmon resonance surface," Physical Chemistry Chemical Physics **9**, 344-345 (2007).

77. J. P. O'Reilly, J. D. Fisk, M. Rooth, E. Perkins, and A. M. Shaw, "Non-linear plasmon response to protein binding at a nanostructured gold particle plasmon resonance surface," Phys Chem Chem Phys **9**, 344-345 (2007).

78. J. Ye, K. Bonroy, D. Nelis, F. Frederix, J. D'Haen, G. Maes, and G. Borghs, "Enhanced localized surface plasmon resonance sensing on three-dimensional gold nanoparticles assemblies," Colloids and Surfaces a-Physicochemical and Engineering Aspects **321**, 313-317 (2008).

79. R. de Waele, A. F. Koenderink, and A. Polman, "Tunable nanoscale localization of energy on plasmon particle arrays," Nano Lett. **7**, 2004-2008 (2007).

80. Talbot, "Facts relating to optical science," Philos. Mag. **9** (1836).

81. L. Rayleigh, "On copying diffraction gratings and on some phenomenon connected therewith," Philos. Mag. **11** (1881).

82. K. Patorski, "The Self-Imaging Phenomenon and its Applications " Proc. SPIE 5036, 129 (2003)

83. A. Wang, P. Gill, and A. Molnar, "Light field image sensors based on the Talbot effect," Applied

Optics **48**, 5897-5905 (2009).

84. G. S. Spagnolo, and D. Ambrosini, "Talbot effect application: measurement of distance with a Fourier-transform method," Measurement Science & Technology **11**, 77-82 (2000).

85. V. I. Kakichashvili, and O. G. Tkeshelashvili, "Theory of the Talbot effect in oblique-angled rasters," Zhurnal Tekhnicheskoi Fiziki **56**, 2221-2223 (1986).

86. M. Testorf, J. Jahns, N. A. Khilo, and A. M. Goncharenko, "Talbot effect for oblique angle of light propagation," Optics Communications **129**, 167-172 (1996).

87. L. Schermelleh, R. Heintzmann, and H. Leonhardt, "A guide to super-resolution fluorescence microscopy," Journal of Cell Biology **190**, 165-175 (2010).